REPORT NO. GDCA-DFM72 -009
CONTRACT NAS 8-26363

DRA

SPACE SHUTTLE ASCENT FLIGHT TURBULENCE RESPONSE

INTERIM REPORT

GENERAL DYNAMICS
Convair Aerospace Division

REPORT NO. GDCA-DFM72-009

SPACE SHUTTLE ASCENT FLIGHT TURBULENCE RESPONSE

INTERIM REPORT

15 September 1972

Prepared Under
Contract NAS8-26363

Submitted to
National Aeronautics and Space Administration
GEORGE C. MARSHALL SPACE FLIGHT CENTER
Huntsville, Alabama

Prepared by
CONVAIR AEROSPACE DIVISION OF GENERAL DYNAMICS
San Diego, California

FOREWORD

This report presents the second year results of an investigation being conducted under Contract NAS8-26363 for NASA George C. Marshall Space Flight Center under the technical direction of the Aero-Astrodynamics Laboratory, Dynamics and Control Division. Dr. S. Winder is the technical monitor. The study is being performed by Convair Aerospace Division of General Dynamics under the direction of Mr. R. Huntington, project leader.

The author is indebted to Mr. H. Riead for his assistance in performing the numerical analysis.

TABLE OF CONTENTS

LIST OF FIGURES

LIST OF FIGURES, Continued

LIST OF TABLES

SUMMARY

A totally reusable space shuttle configuration has been analyzed during ascent flight to determine its response to atmospheric turbulence. Responses in the form of booster and orbiter body accelerations and booster wing root shear, bending moment and torque were obtained due to random and quasi-square-wave discrete turbulence. The configuration was also analyzed with booster aerodynamic surfaces removed to simulate an expendable booster. Symmetric and antisymmetric analyses were performed. Propellant sloshing, gust penetration, and automatic control system effects were included.

The steady-state aerodynamic method of Woodward was used to derive the generalized aerodynamic forces using the standard quasi-steady assumption. Aerodynamic interference effects between adjacent wings and bodies were found to be significant. Total normal force and moment data computed by the Woodward method agreed well with wind tunnel values.

It was found that the symmetric responses were generally higher than the antisymmetric ones. The stability augmentation system tended to lower the booster accelerations in the symmetric case, while increasing the orbiter accelerations.

Loads due to the 9 m/s quasi-square-wave gust were higher than the 3σ random turbulence loads, indicating that the discrete gust design criterion may be conservative. The elastic portion of the response accounted for about 15% of the total wing load in the discrete gust analysis, while in the random case the elastic effect was small.

SECTION 1

INTRODUCTION

This report presents the results of the second year's work under Contract NAS8-26363, Aeroelastic Effects on Shuttle Vehicle Dynamics. The first year of the study is documented in References 1 and 2.

During the first year, a method was developed for determining the response of space shuttle to atmospheric turbulence. The objective of the second year's effort was to apply this technique to the shuttle configuration during ascent flight.

The analysis method accounts for propellant sloshing, gimbaled engine dynamics and stability augmentation system (SAS)/elastic vehicle coupling. The problem is formulated in the frequency domain to permit the use of existing unsteady or quasi-steady state aerodynamic theories based on harmonic motion for computing generalized aerodynamic forces. Either discrete or random turbulence can be treated. For the random case, statistical outputs are generated relating vehicle loads and accelerations to level of turbulence. A Fourier series is used to approximate the discrete gust shape. Discrete responses are in the form of time histories.

A finding of the first year's study was that properly predicting flow interference, thickness, angle-of-attack, and body aerodynamics is more important for space shuttle than including unsteady aerodynamic lag effects for the low to moderate reduced-frequency range of interest in the turbulence response problem. It was recommended that the Woodward steady-state aerodynamic method (Reference 3) be applied in future space shuttle turbulence response studies using the standard quasi-steady state assumption which includes aerodynamic damping due to plunging velocity.

In the study reported here, the space shuttle configuration shown in Figure 1-1 was analyzed at Mach numbers of 0.8 and 1.2, which are in the region of maximum dynamic pressure on the ascent trajectory (Figure 1-2). Symmetric and antisymmetric responses to random and discrete turbulence were obtained. The turbulence models were as specified in Reference 4. The Woodward aerodynamic method was used to compute the generalized forces. To simulate a non-flyback booster, calculations were also made for the configuration shown in Figure 1-1 with all booster aerodynamic surfaces removed. Propellant sloshing effects were included. The SAS was included in one symmetric condition. A summary of conditions analyzed is given in Table 1-1.

Section 2 contains detailed discussions of the modal and aerodynamic analyses, and results of the turbulence response calculations. Conclusions and recommendations for further work are presented in Section 3.

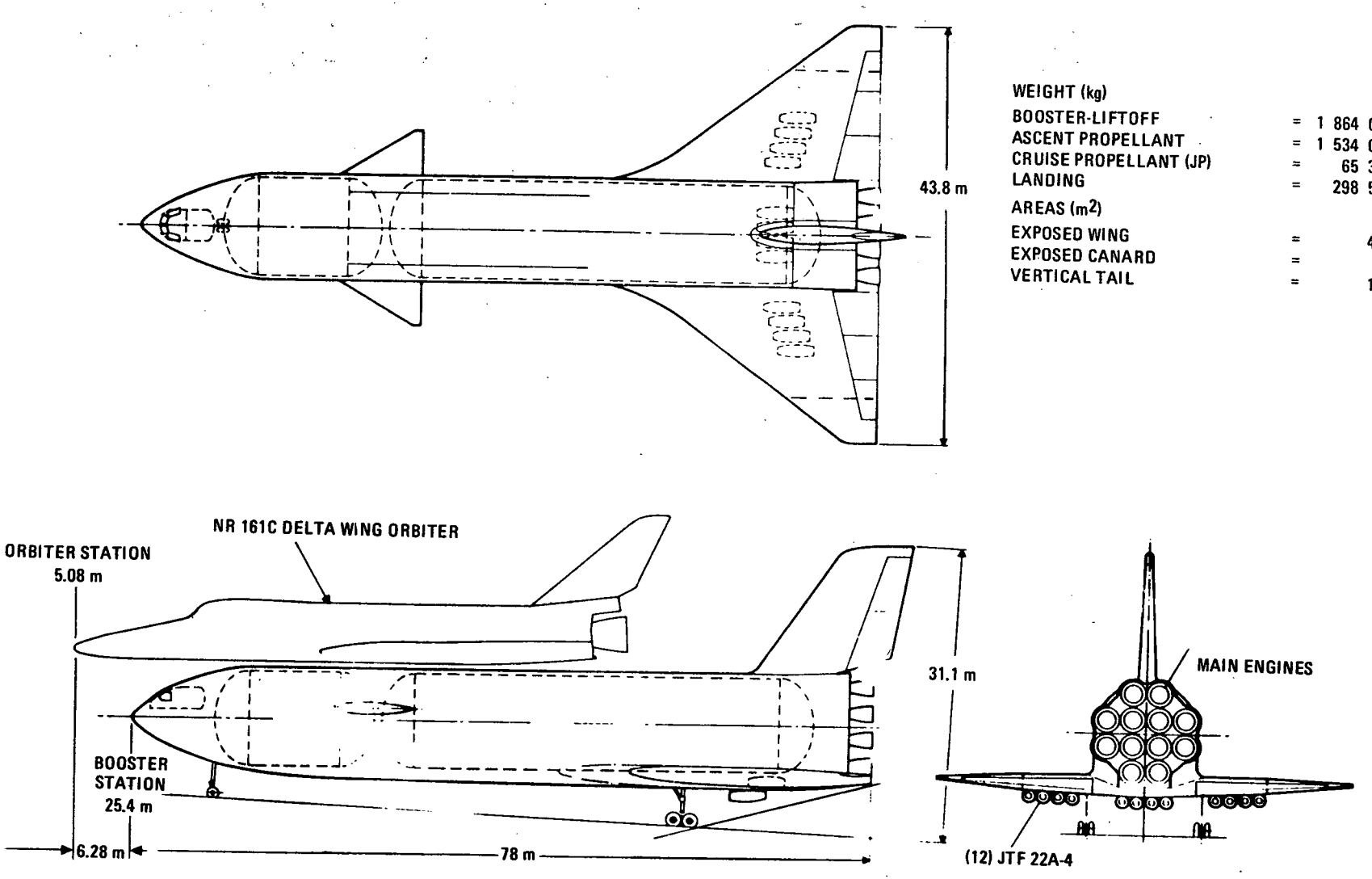

Figure 1-1. Study Vehicle

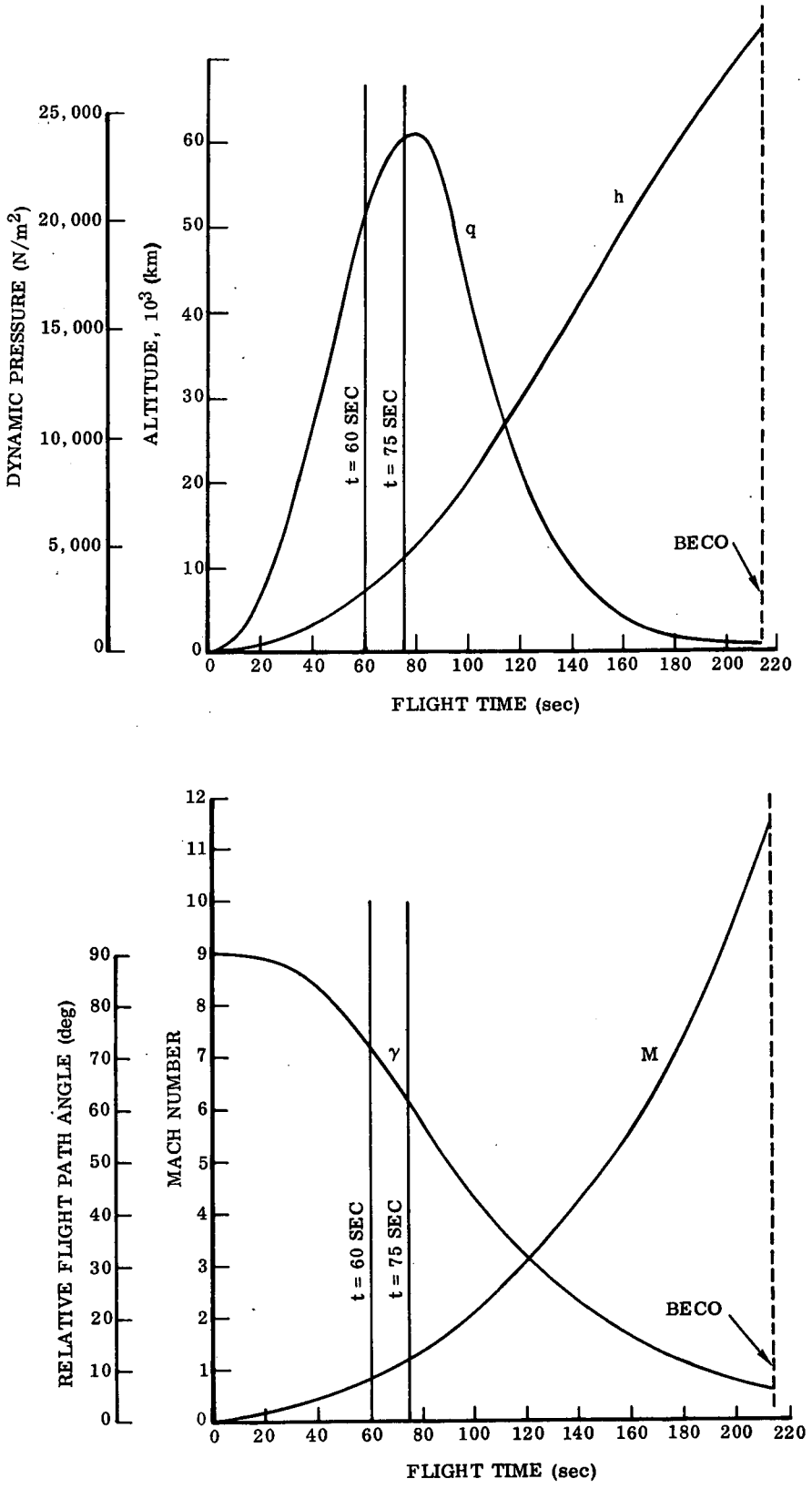

Figure 1-2. Ascent Trajectory

Table 1-1. Conditions Analyzed

Condition No.	Mach No.	Booster Aero Surfaces	Boundary Condition	SAS	Response Type
1	1.2	On	Sym.	Off	Discrete
2	1.2	On	Sym.	Off	Random
3	1.2	On	Sym.	On	Random
4	1.2	Off	Sym.	Off	Random
5	1.2	On	A/S	Off	Random
6	1.2	On	A/S	Off	Discrete
7	1.2	Off	A/S	Off	Random
8	0.8	On	Sym.	Off	Random
9	0.8	Off	Sym.	Off	Random
10	0.8	On	A/S	Off	Random
11	0.8	Off	A/S	Off	Random

SECTION 2

TECHNICAL DISCUSSION

Significant effort was put forth in deriving the input data for the turbulence response analysis. Therefore, Sections 2.1 and 2.2 present details concerning the modal and aerodynamic analyses, respectively. A detailed discussion of the turbulence response analysis, along with significant results, is presented in Section 2.3.

2.1 MODAL ANALYSIS

The NASTRAN computer program (Reference 5) was used to obtain the structural vibration modes for the mated space shuttle configuration. The over-all structural idealization is shown in Figure 2-1. The orbiter body is represented as a flexible beam, and the orbiter aerodynamic surfaces are rigid. The booster body and aerodynamic surfaces are elastic, represented in considerable structural detail. By use of the Guyan reduction (Reference 5), the dynamic degrees of freedom were reduced to 107 for the symmetric analysis and 106 for the antisymmetric case.

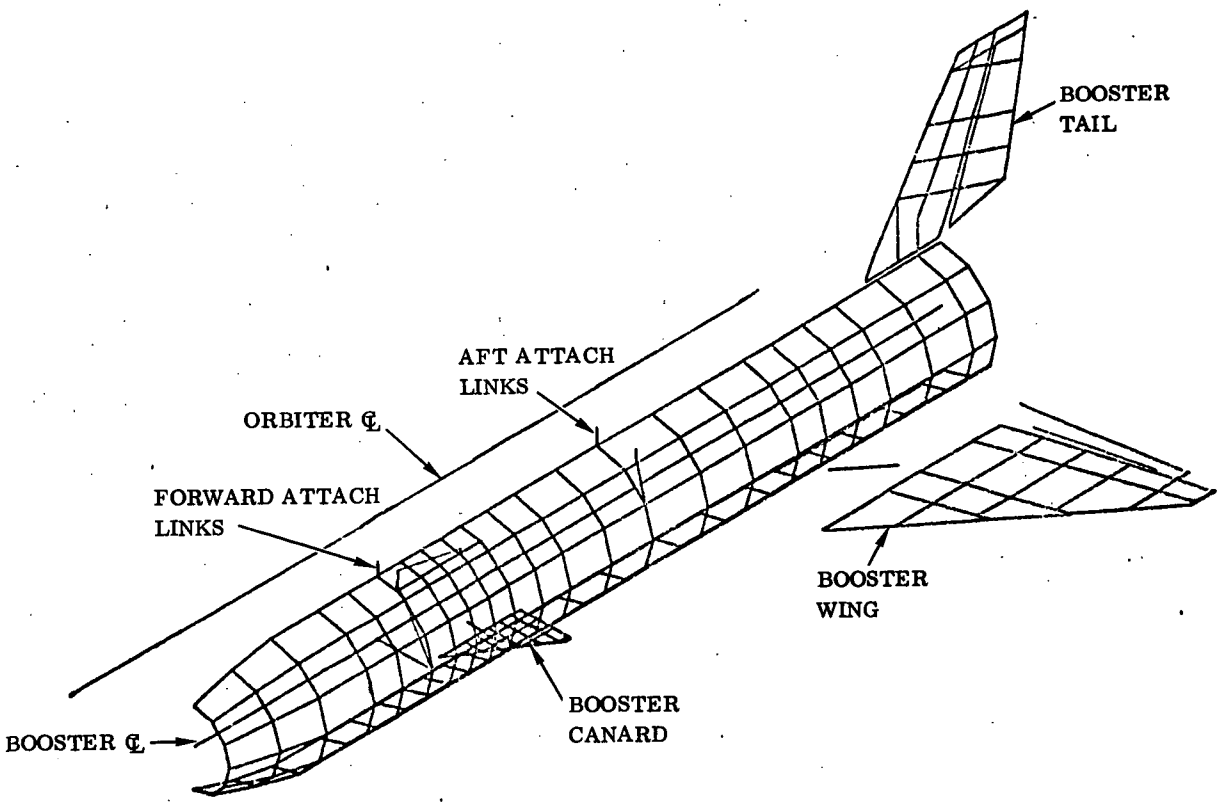

Figure 2-1. Over-all Structural Idealization

The modal frequencies are summarized in Table 2-1. The mode shapes for t = 75 seconds are shown in Figure 2-2 for the symmetric case. Figure 2-3 presents the corresponding antisymmetric modes.

Table 2-1. Summary of Modal Frequencies (Hz)

Type	t = 60 sec	t = 75 sec
Symmetric	1.07	1.09
	1.17	1.17
	1.48	1.48
	2.05	2.06
	2.18	2.19
	2.49	2.49
	2.80	2.89
	3.02	3.04
Antisymmetric	0.87	0.87
	1.26	1.28
	1.77	1.77
	2.37	2.52
	3.19	3.19
	3.45	3.82
	4.28	4.32

The mode shapes at t = 60 seconds were assumed to be identical to those at 75 seconds. The generalized masses were corrected for the heavier mass distribution by the equation

$$\mathfrak{m}_{60_j} = \mathfrak{m}_{75_j} + \sum_{i=1}^{n} \Delta m_i \, \phi_{i_j} \qquad (1)$$

where $\mathfrak{m}_{t_j}$ is the generalized mass of mode j at time t, Δm_i is the change in mass at the i^{th} structural grid point, ϕ_{i_j} is the deflection at grid point i due to mode j, and the summation is over all grid points, n.

The frequencies were corrected by the equation

$$\omega_{60_j} = \omega_{75_j} \sqrt{\frac{\mathfrak{m}_{75_j}}{\mathfrak{m}_{60_j}}} \qquad (2)$$

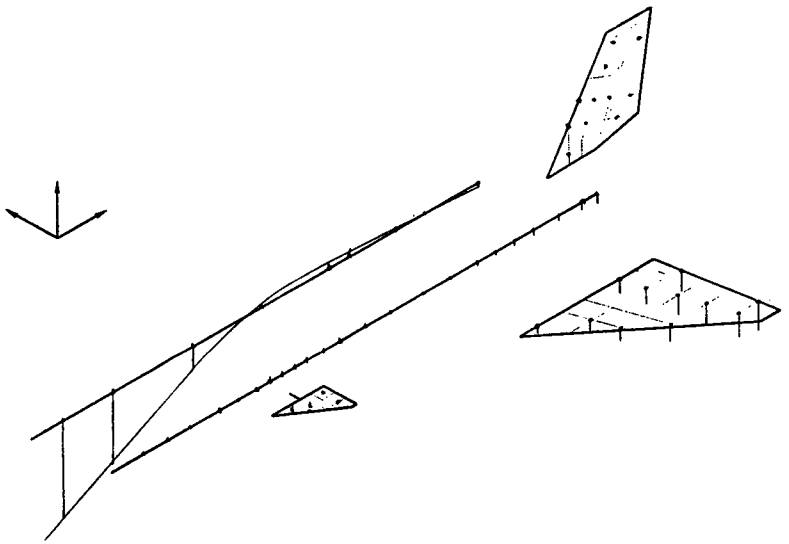

Mode 1, 1.09 Hz

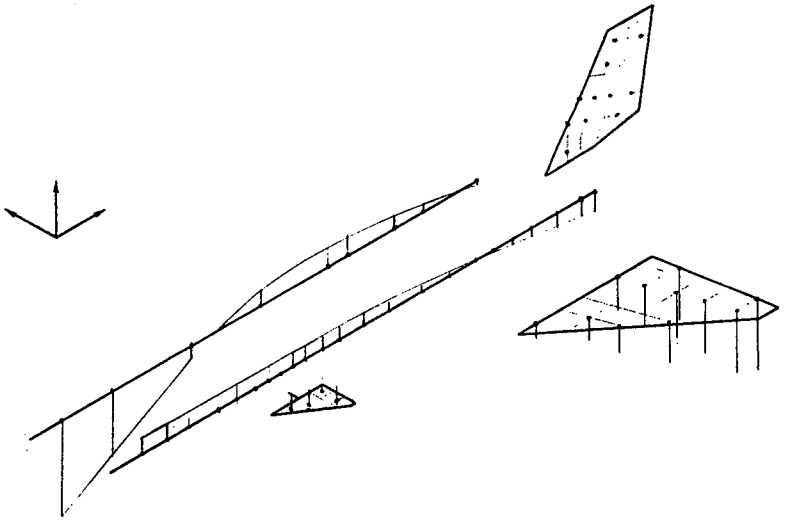

Mode 2, 1.17 Hz

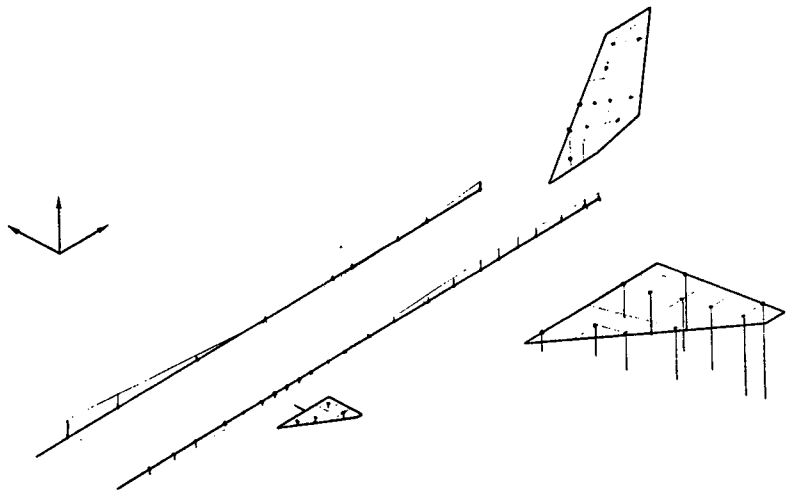

Mode 3, 1.48 Hz

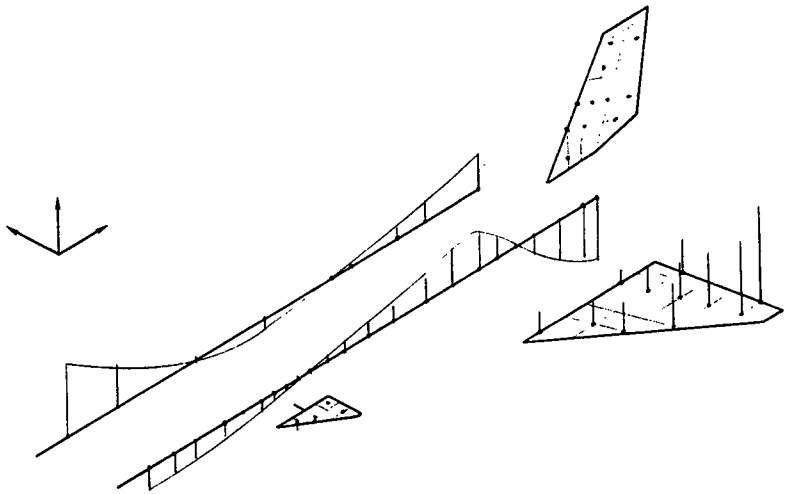

Mode 4, 2.05 Hz

Figure 2-2. Symmetric Mode Shapes (t = 75 sec) (Sheet 1 of 2)

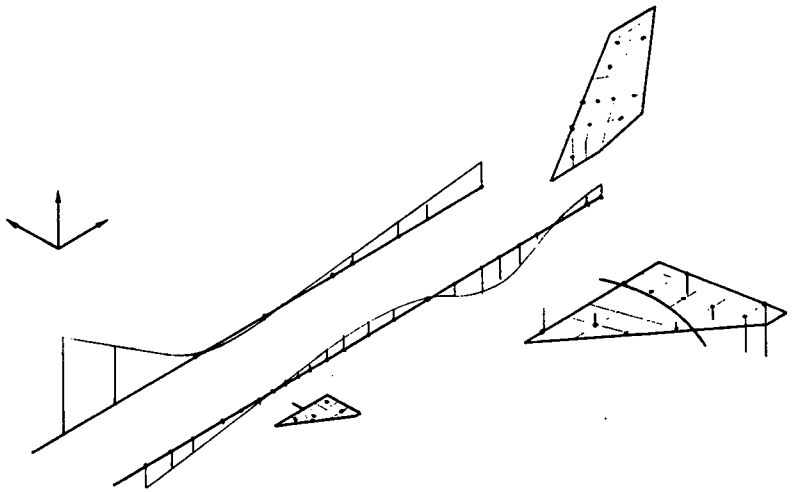

Mode 5, 2.19 Hz

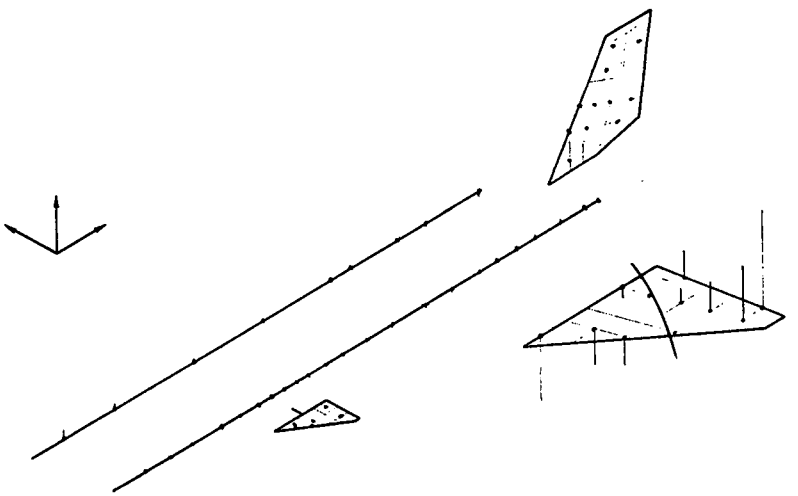

Mode 6, 2.49 Hz

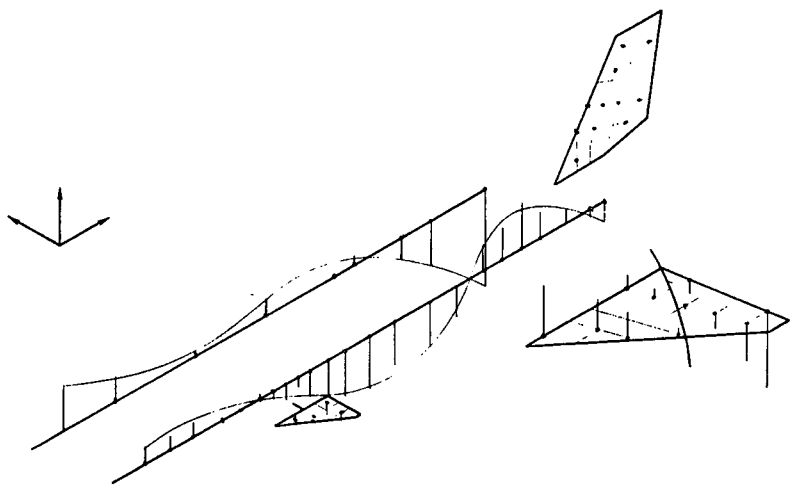

Mode 7, 2.89 Hz

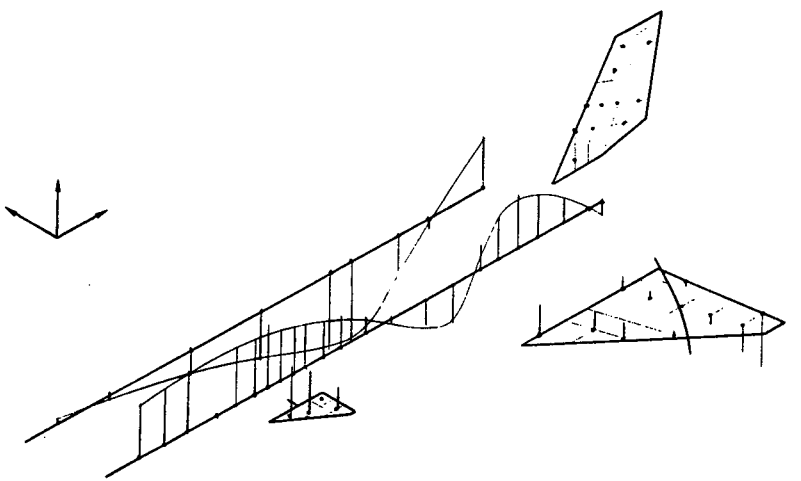

Mode 8, 3.04 Hz

Figure 2-2. Symmetric Mode Shapes (t = 75 sec) (Sheet 2 of 2)

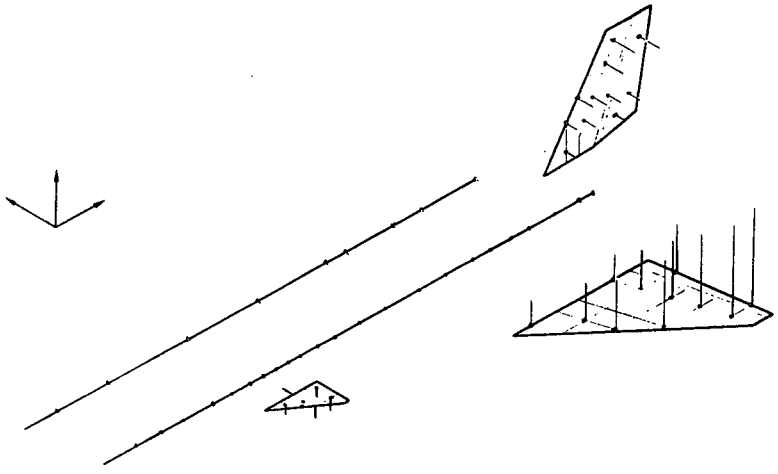

Mode 1, 0.87 Hz

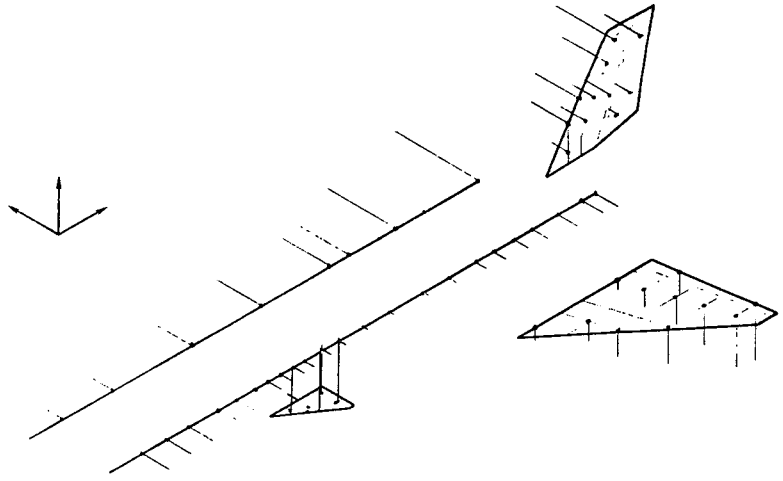

Mode 2, 1.28 Hz

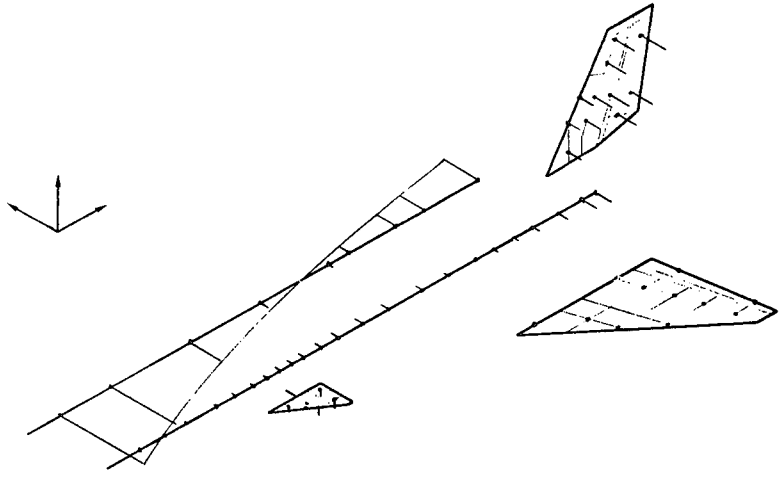

Mode 3, 1.77 Hz

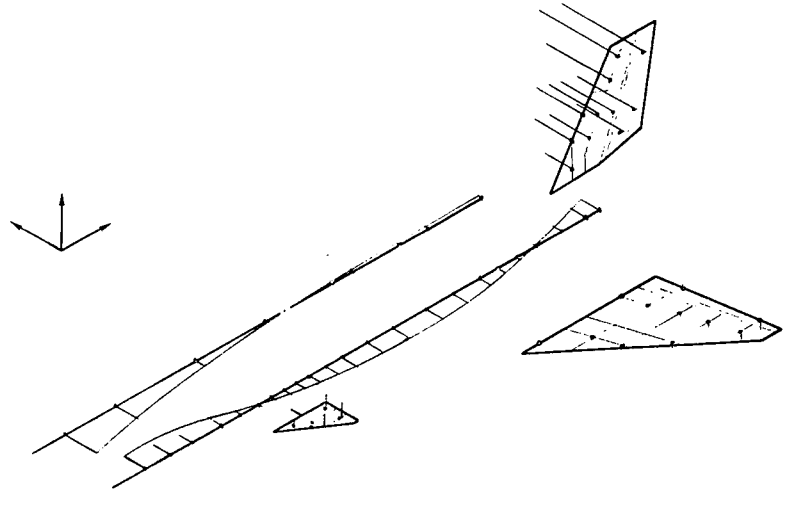

Mode 4, 2.52 Hz

Figure 2-3. Antisymmetric Mode Shapes (t = 75 sec) (Sheet 1 of 2)

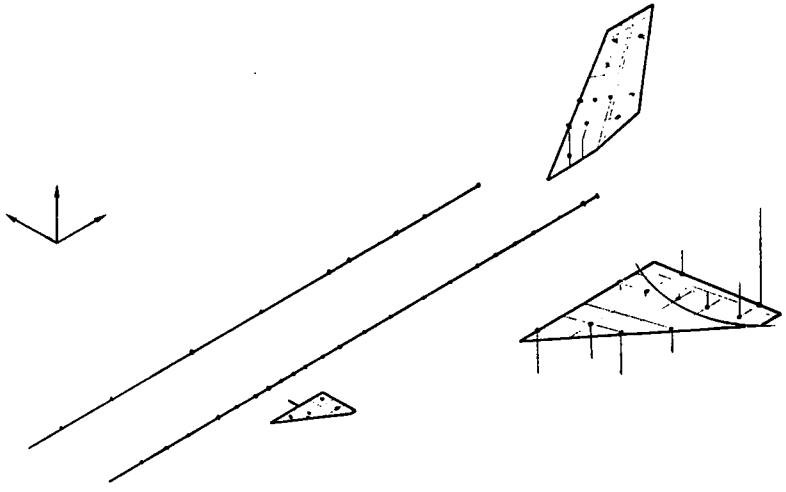

Mode 5, 3.19 Hz

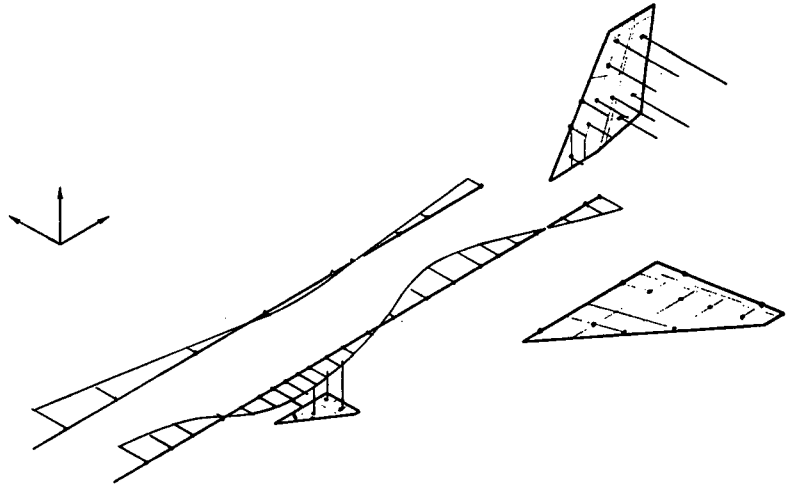

Mode 6, 3.82 Hz

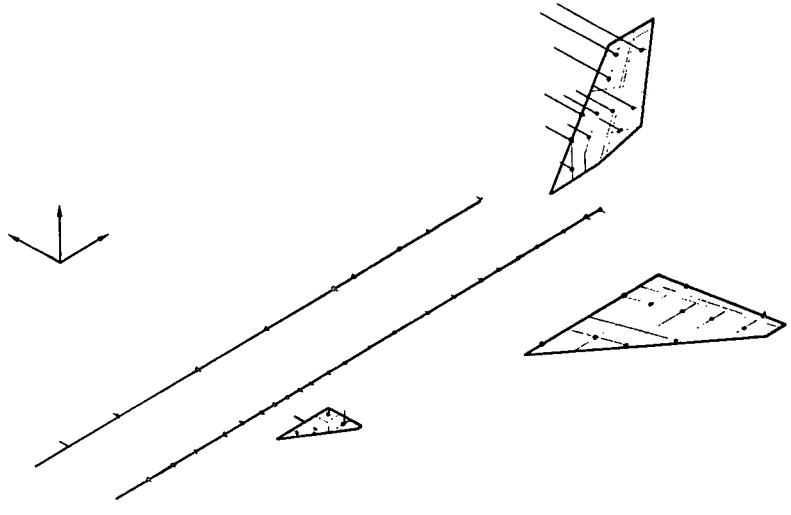

Mode 7, 4.32 Hz

Figure 2-3. Antisymmetric Mode Shapes (t = 75 sec) (Sheet 2 of 2)

The effect of removing the booster aerodynamic surfaces was accounted for in a similar fashion. The mode shapes and frequencies were assumed to remain constant, and the generalized masses were adjusted according to Equation 1. Modes consisting almost entirely of booster aerodynamic surface motion were eliminated (symmetric mode 6 and antisymmetric modes 1, 5 and 7).

2.2 GENERALIZED AERODYNAMIC FORCE DETERMINATION

The steady-state aerodynamic method of Woodward (Reference 3) was applied to the space shuttle configuration to generate aerodynamic forces. The justification for using steady-state aerodynamics instead of unsteady is given in Reference 1. To summarize briefly: the Woodward method accounts for wing-wing, wing-body and body-body interference, angle-of-attack, thickness and other flow effects not accounted for in most unsteady theories. The reduced frequency range of interest is low enough in the shuttle turbulence response problem that aerodynamic lag effects are relatively small. By using steady-state aerodynamics, the computation of aerodynamic forces is made once for each Mach number instead of for each value of reduced frequency as is required in the unsteady case.

Assuming harmonic motion, the quasi-steady complex downwash at point j due to a unit amount of the k^{th} generalized coordinate is

$$w_{jk} = V\alpha_{jk} - i\,\omega h_{jk} \tag{3}$$

where the first term is the downwash due to the flight velocity, V, and the modal angle of attack, α; and the second term is the downwash induced by the surface plunging motion of amplitude h and frequency ω.

The generalized aerodynamic force consists of two parts; that due to turbulence, and that due to vehicle motion. Specifically, the generalized aerodynamic force acting on mode r is given by

$$\bar{Q}_r = \underbrace{\sum_{s=1}^{n} q_s\, \bar{Q}_{rs}}_{\text{Response}} + \underbrace{q_f\, \bar{Q}_{rf}}_{\text{Gust}} \tag{4}$$

where $\bar{Q}_{rs}$ is the r^{th} generalized aerodynamic force due to a unit value of the vehicle displacement in mode s, q_f is the gust amplitude, and $\bar{Q}_{rf}$ is the r^{th} generalized aerodynamic force due to a unit gust. $\bar{Q}_{rs}$ is defined by the equation

$$\bar{Q}_{rs}(\omega) = \int_S h_r(x,y,z)\, \Delta p_s(x,y,z,\omega)\, dS \tag{5}$$

where Δp_s is the net pressure acting on the vehicle due to oscillation in mode s, and the integration is over the surface of the vehicle.

The generalized force due to the unit sinusoidal gust is given by:

$$\bar{Q}_{rf}(\omega) = \int_S h_r(x,y,z)\, \Delta p_f(x,y,z,\omega)\, dS \tag{6}$$

where Δp_f is the net pressure over the vehicle surface due to the downwash produced by a continuous sinusoidal gust wave traveling across the vehicle. This sinusoidal gust velocity may be expressed as:

$$W_f = q_f e^{i\omega t}$$

$$= q_f (\cos \omega t + i \sin \omega t) \tag{7}$$

The downwash on an oscillating airfoil in a flow of velocity (V) is given by:

$$w(t) = V\alpha(t) - \dot{h}(t) \tag{8}$$

where α is the angle of attack and $\dot{h}$ is the plunging velocity. For harmonic motion, the complex downwash may be written:

$$\bar{w} = V\bar{\alpha} - i\omega\bar{h} \tag{9}$$

Equating (7) and (9) yields:

$$W_f = \bar{w}$$

$$\bar{\alpha} = \frac{q_f}{V} \cos \omega t \tag{10}$$

$$\bar{h} = -\frac{q_f}{\omega} \sin \omega t \tag{11}$$

If x_i is the distance from a gust reference axis to the downwash at point i on the vehicle and k is the reduced frequency

$$\left(k = \frac{b\omega}{V}\right) \tag{12}$$

then Equations 9 and 10 become:

$$\bar{\alpha}_i = \frac{q_f}{V} \cos k\bar{x}_i \tag{13}$$

$$\bar{h}_i = - \frac{q_f b}{V k} \sin k \bar{x}_i \tag{14}$$

where

$$\bar{x}_i = \frac{x_i}{b}$$

Equations 13 and 14, when substituted for α and h in Equation 3, give the downwash distribution over the vehicle due to unit turbulence.

Having the unit downwash distributions, the Woodward method is used to derive the net pressure distributions required to solve Equations 5 and 6. Essentially, a matrix of influence coefficients, [F], is generated relating pressure to downwash in the form

$$\{p\} = [F] \{w\} \tag{15}$$

Woodward represents the vehicle as a system of source, doublet, and vortex singularities. The wings and bodies are divided into panels defining the boundaries of planar singularities. Line singularities distributed along the body centerline simulate body lift.

The aerodynamic panel representation employed here, shown in Figure 2-4, consists of 91 wing and 126 body panels. The body centerline points locating the line singularities

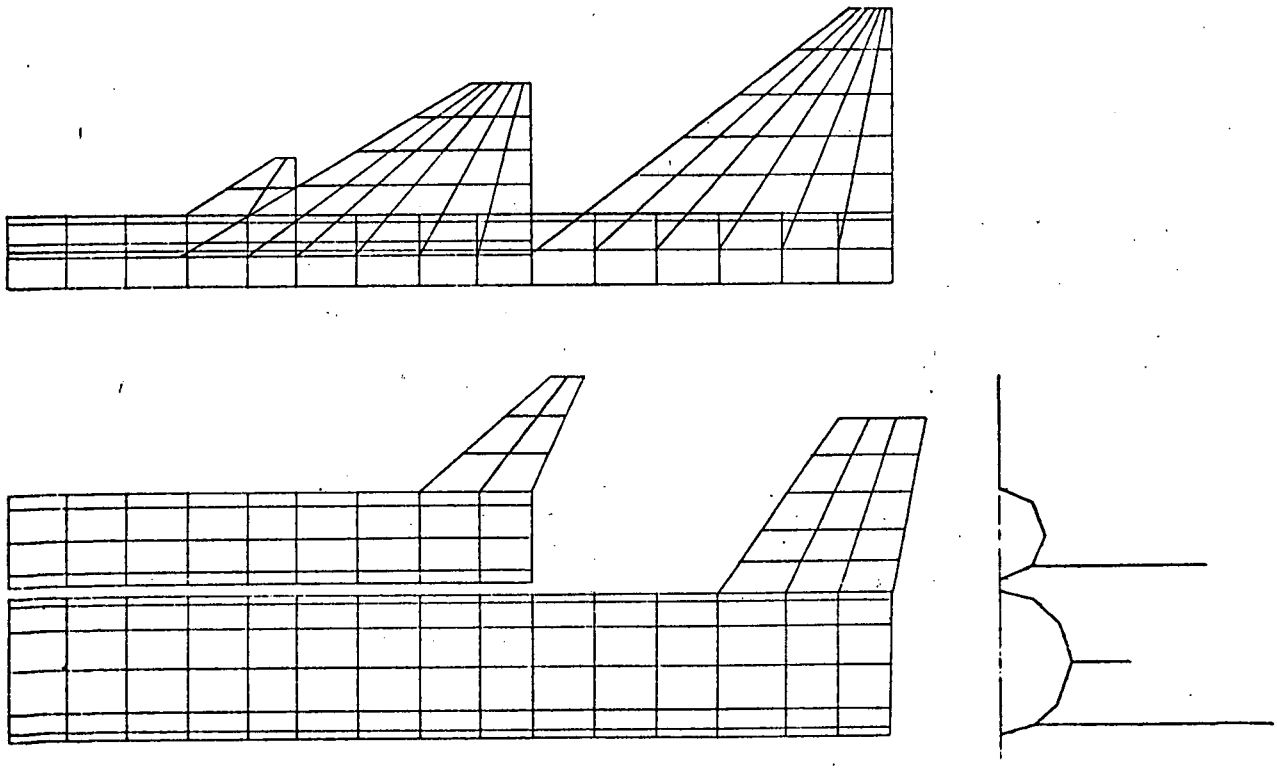

Figure 2-4. Aerodynamic Panel Representation

(not shown) were generally distributed per each ring of body panels and continued forward to the nose of each body at about the same spacing.

The booster wing, canard, and tail panels were removed to represent the configuration without booster aerodynamic surfaces.

There is no convenient way to display the aerodynamic influence coefficient data generated in this study. There were some interesting results, however, which will be discussed briefly.

Figure 2-5 shows the nondimensional aerodynamic center location and the total normal force coefficient derivative as a function of Mach number for the booster in the presence of the orbiter. The continuous curves are based on wind tunnel data as reported in Reference 7. The points represent the Woodward results at Mach number 0.8 and 1.2. Exact agreement is shown except for the aerodynamic center location at Mach 1.2 where the calculated value is 5% low. This is a remarkable agreement and increases the confidence in the pressure data for which there are no corresponding wind tunnel measurements.

The magnitude of the flow interference effects is suggested by Table 2-2, which compares the total normal force coefficient of the mated configuration with that of the

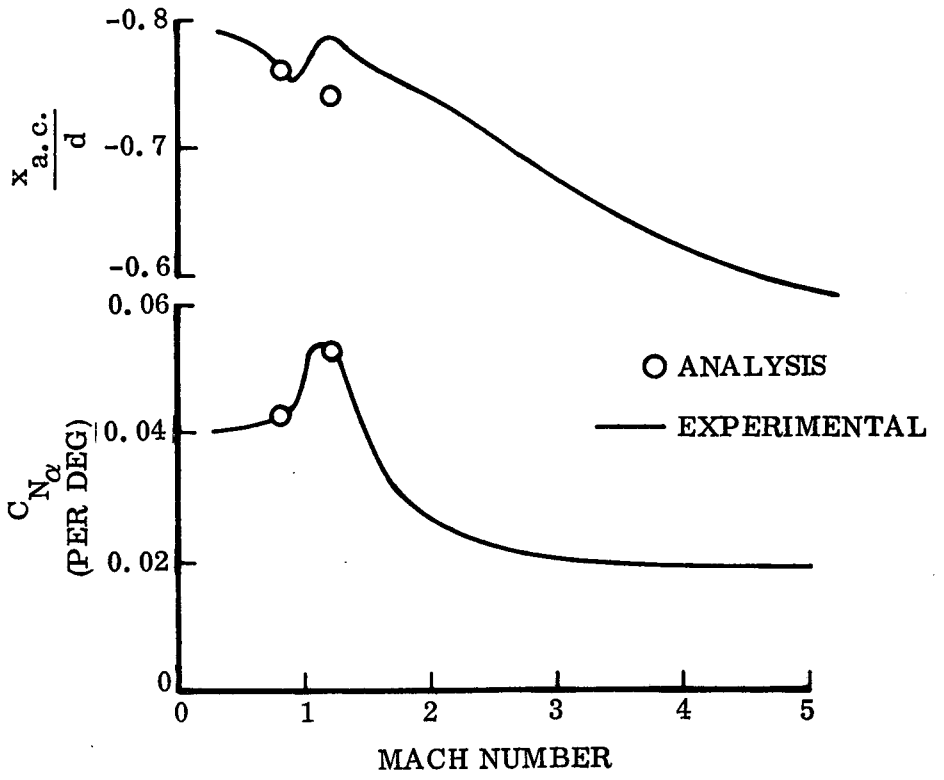

Figure 2-5. Booster Longitudinal Characteristics in Presence of Orbiter

Table 2-2. Inter-vehicle Flow Interference Effects

(M = 0.8, α = 0)

	Total Normal Force Coefficient
Booster Alone	0.0654
Orbiter Alone	0.0096
Total	0.0750
Booster in Presence of Orbiter	0.0925
Orbiter in Presence of Booster	0.0083
Total	0.1008

(Interference = 26% of total)

independent vehicles at 0.8 Mach number. Interference between the vehicles accounts for 26% of the total normal force coefficient of the mated configuration. These results were obtained from the Woodward analysis.

Table 2-3 summarizes the total normal force coefficients derived using the Woodward analysis at Mach numbers of 0.8 and 1.2 at 0 and 6 degrees angle-of-attack. The top figures correspond to the mated configuration and the numbers in parentheses pertain to the booster in presence of the orbiter. The effect of removing the booster aerodynamic surfaces can also be seen.

Table 2-3. Total Normal Force Coefficient Summary

	M = 0.8		M = 1.2	
	With Aero Surfaces	W/O Aero Surfaces	With Aero Surfaces	W/O Aero Surfaces
α = 0°	0.1008	-0.0085	0.0395	-0.0472
	(0.0925)	(0.0072)	(0.1014)	(0.0225)
α = 6°	0.4921	0.1342	0.5359	0.1753
	(0.3534)	(0.0073)	(0.4211)	(0.0557)

( ) = Booster in presence of orbiter.

Figure 2-6 shows typical pressure coefficient distributions for the booster body. The pressure coefficient is defined by the equation

$$\Delta C_p = \frac{p - p_\infty}{q_\infty} \tag{16}$$

where p is the local pressure and p_∞ and q_∞ are the free-stream pressure and dynamic pressure, respectively.

The top portion of the figure shows the effect of booster/orbiter interference. The dashed curve represents the pressure distribution for the isolated booster body. The corresponding pressure distribution in the presence of the orbiter is shown by the solid curve. These distributions are for a line running from nose to tail, 45 degrees from the top of the booster.

The bottom curves of Figure 2-6 show the effect of the booster aerodynamic surfaces on the booster body pressure distribution at 135 degrees from the top. All of the information shown in this figure is for 6 degrees angle-of-attack and Mach number 1.2.

Typical wing pressure distributions are shown in Figure 2-7. This figure shows the net (upper surface minus lower surface) pressure distributions in the chordwise

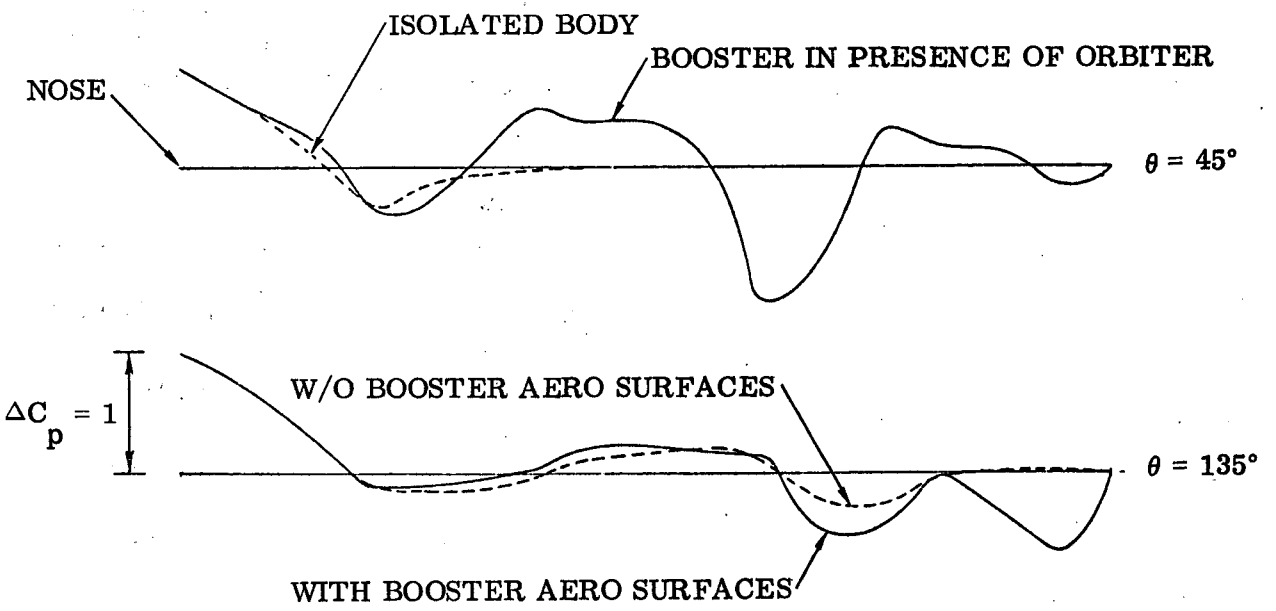

Figure 2-6. Booster Body Pressure Distributions (M = 1.2, α = 6 deg)

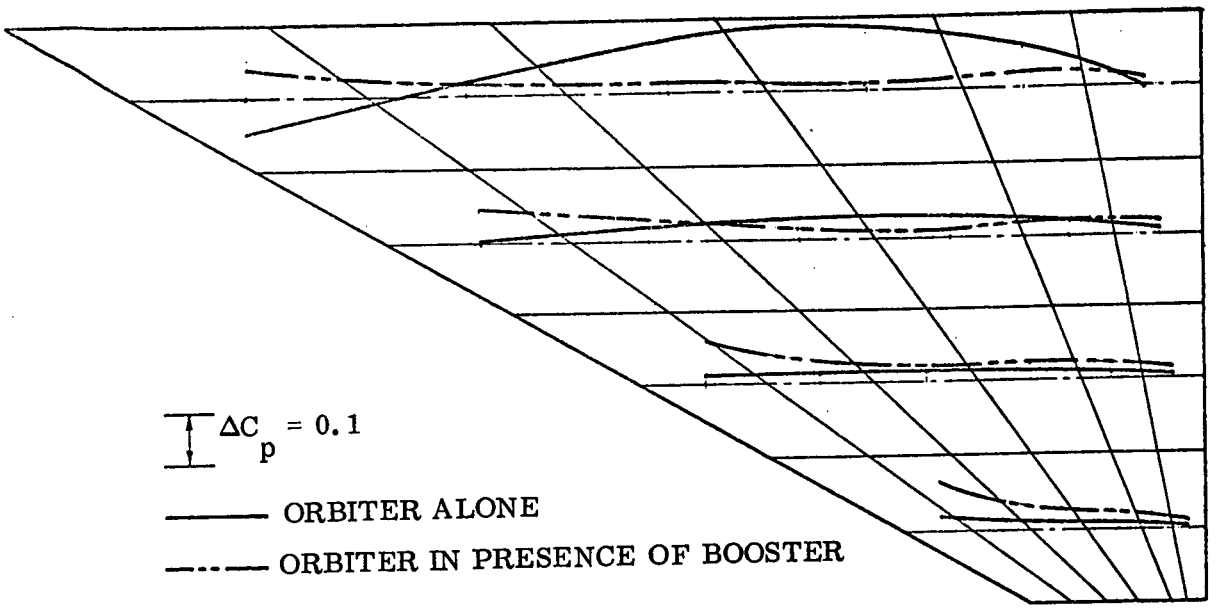

Figure 2-7. Orbiter Wing Pressure Distribution (M = 0.8, α = 0 deg)

direction for four span stations. The solid curves are for the orbiter alone and the pressures including the presence of the booster are shown by the dashed lines.

Good pressure data is essential when performing any type of elastic vehicle response or stability analysis in which aerodynamic forces are significant. The preceeding discussion has presented a brief insight into the complex flow fields associated with vehicles such as space shuttle. The Woodward method appears at this time to be the best analytical approach for determining steady-state pressure distributions for complex configurations at subsonic and supersonic speeds. Further correlations with experimental data are required to corroborate these findings.

2.3 TURBULENCE RESPONSE ANALYSIS

This section presents a brief review of the equations of motion, a discussion of the random and discrete turbulence models used, and details and results of the response calculations. A more detailed discussion of the theory is contained in Reference 1.

Lagrange's equation of motion

$$\frac{d}{dt}\left(\frac{\partial L}{\partial \dot{q}_r}\right) - \frac{\partial L}{\partial q_r} + \frac{\partial \mathcal{D}}{\partial q_r} = \bar{Q}_r \qquad r = 1,2, \ldots n \tag{17}$$

is used to formulate the response problem where

$L = T - P$

T = kinetic energy

P = potential energy

$\mathcal{D}$ = dissipation function

$\bar{Q}_r = r^{th}$ generalized force

$q_r = r^{th}$ generalized coordinate

The deflection (h) at any point on the vehicle is given by

$$h(x,y,z,t) = \sum_{r=1}^{n} h_r\,(x,y,z)\; q_r(t) \tag{18}$$

where h_r is the normalized deflection at the point in the r^{th} mode shape.

Using normal (with respect to the stiffness matrix) modes of vibration as generalized coordinates, the r^{th} equation of motion is of the form

$$M_{rr}\ddot{q}_r + D_{rr}\dot{q}_r + M_{rr}\,\omega_r^2\, q_r + \sum_{s=1}^{n} \delta^*_{rs} M_{rs}\,\ddot{q}_r = \bar{Q}_r \tag{19}$$

where

M_{rs} = generalized mass

D_{rr} = generalized damping

ω_r = frequency of mode r

$$\delta^*_{rs} = \begin{cases} 0, & r=s \\ 1, & r\neq s \end{cases}$$

and the generalized force, $\bar{Q}_r$, is defined by Equation 4.

Assuming harmonic motion, Equation 19 can be written in matrix form as

$$\left|q(\omega)\right| = -\left[A(\omega)\right]^{-1} \left|A_f(\omega)\right| \tag{20}$$

where

$$A_{rs} = \left[1 - \delta_{rs}\left(\frac{\omega_r}{\omega}\right)^2 (1 + ig_r)\right] \bar{M}_{rs} + Q_{rs} \tag{21}$$

$$\delta_{rs} = \begin{cases} 1, r=s \\ 0, r \neq s \end{cases}$$

$i = \sqrt{-1}$

g_r = structural damping coefficient for mode r

ω = gust frequency

$\bar{q}_r$ = amplitude of the r^{th} generalized coordinate

$$\bar{M}_{rs} = \frac{M_{rs}}{4\rho b^3} \tag{22}$$

$$A_{rf}(\omega) = \frac{q_f \bar{Q}_{rf}(\omega)}{4\rho b^3 \omega^2} \tag{23}$$

$$Q_{rs}(\omega) = \frac{\bar{Q}_{rs}(\omega)}{4\rho b^3 \omega^2} \tag{23}$$

where ρ is air density, b is reference length, and q_f is the turbulence amplitude.

Transfer functions are formed relating response to turbulence amplitude by the load summation method, which is written

$$H(x,y,z,\omega) = \frac{\omega^2}{q_f} \sum_{r=1}^{n} F'_r(x,y,z)\, \bar{q}_r(\omega)$$

$$+ \frac{1}{q_f} \sum_{r=1}^{n} \bar{F}_r(x,y,z,\omega)\, \bar{q}_r(\omega) + \frac{F_f(x,y,z,\omega)}{q_f} \tag{24}$$

where F'_r is the response (acceleration, shear, moment, or torque) due to the r^{th} degree of freedom oscillating at a unit frequency, $\bar{F}_r$ is the load due to the aerodynamic pressure distribution developed by a unit amount of the r^{th} generalized coordinate oscillating at frequency ω, and F_f is the load due to the aerodynamic pressure distribution produced by a gust wave of frequency ω.

For random turbulence, the response power spectral density (PSD), ϕ_x, is related to the gust PSD, ϕ, and the transfer function magnitude, $|H|$, by the equation:

$$\phi_x(\omega) = |H(\omega)|^2 \phi(\omega) \tag{25}$$

The ratio of rms response to rms gust velocity is given by

$$\bar{A} = \left[\int_0^{\omega_c} \phi_x(\omega) d\omega \right]^{1/2} \tag{26}$$

where ω_c is the integration cutoff frequency. The "characteristic frequency" of the response, or number of zero crossings with positive slope per second, is expressed by

$$N_o = \frac{1}{2\pi \bar{A}} \left[\int_0^{\omega_c} \omega^2 \phi_x(\omega) \, d\omega \right]^{1/2} \tag{27}$$

The turbulence PSD applied in this study is the 99th percentile curve (including the dashed portion) shown in Figure 2-8 reproduced from Reference 4. The equation of the curve is

$$E(\kappa) = \frac{683.4 \, (4000\kappa)^{1.62}}{1 + 0.0067 \, (4000\kappa)^{4.05}} \tag{28}$$

where $E(\kappa)$ is the turbulence PSD and κ is the wave number. As specified by Reference 4, design turbulence loads are obtained by multiplying the rms loads by a factor of 3.

In the present study, the spectrum was normalized to produce a unity rms value by dividing Equation 28 by its rms value, 1.94 m/s. Design loads and accelerations are obtained, therefore, by multiplying their $\bar{A}$ values by 5.82 m/s.

Discrete turbulence is simulated by a Fourier series.

$$f(t) = a_o + \sum_{m=1}^{M} (a_m \cos \omega_m t + b_m \sin \omega_m t) \tag{29}$$

where

f(t) is the forcing function

M is the number of terms in the series

t = time

$\omega_m = m \pi / T$

$a_o = \frac{1}{2T} \int_{-T}^{T} f(t) dt$

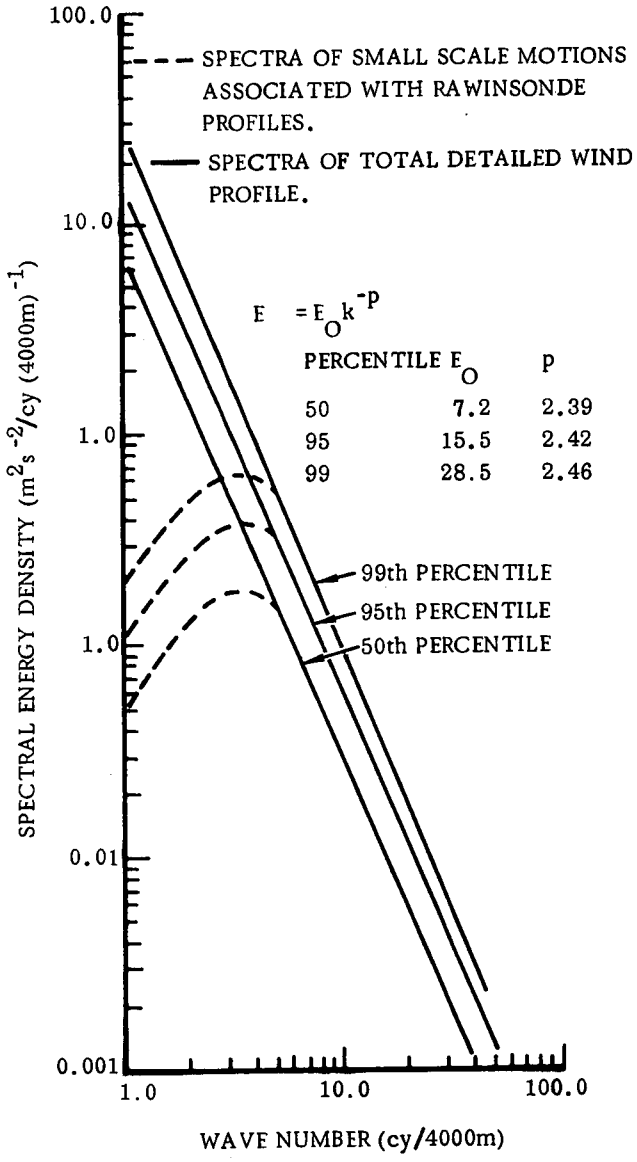

Figure 2-8. Spectra of Detailed Wind Profiles (Reference 4)

$$a_m = \frac{1}{T}\int_{-T}^{T} f(t) \cos \bar{\omega}_m t \, dt$$

$$b_m = \frac{1}{T}\int_{-T}^{T} f(t) \sin \bar{\omega}_m t \, dt$$

The resulting force time-history f(t) is periodic with period 2T.

As prescribed by Equation 29, the force is stationary. It is often more convenient to think of the vehicle as being fixed, with the disturbance moving over it. This is described by substituting (x/V-t) for t in Equation 29, which yields

$$f(t) = a_o + \sum_{m=1}^{M} a_m \cos (k_m \bar{x} - \omega_m t) + b_m \sin (k_m \bar{x} - \omega_m t) \tag{30}$$

where

$k_m = \omega_m b/V$

$\bar{x} = x/b$

b is the reference length

V is the vehicle velocity

x is the distance from a point on the vehicle to the gust reference axis

By considering that the cosine terms are symmetric and the sine terms are antisymmetric, Equation 30 can be written in complex form as

$$f(t) = a_o + \mathrm{Re}\left[\sum_{m=1}^{M} a_m e^{i(\omega_m t - k \bar{x})}\right] - \mathrm{Im}\left[\sum_{m=1}^{M} b_m e^{i(\omega_m t - k \bar{x})}\right] \tag{31}$$

The vehicle response to this disturbance is given by

$$Z(t) = \sum_{m=1}^{M} \left[\left(a_m H_{R_m} + b_m H_{I_m}\right) \cos \bar{\omega}_m t + \left(b_m H_{R_m} - a_m H_{I_m}\right) \sin \bar{\omega}_m t\right] \tag{32}$$

where H_{R_m} and H_{I_m} are the real and imaginary components of the m^{th} transfer function evaluated at frequency $\bar{\omega}_m$, i.e.,

$$H_m = H_{R_m} + iH_{I_m} \tag{33}$$

The discrete gust used in the present study was the "quasi-square-wave" shape described in Reference 4. The gust amplitude was normalized to 1-m/s. The results must therefore be multiplied by a factor of 9 to correspond to the design value specified in Reference 4. The gust length was 170 meters, producing a gust period equal to one-half the period of the first elastic mode at t = 75 seconds. The Fourier series contained 40 terms, resulting in the gust shape shown in Figure 2-9.

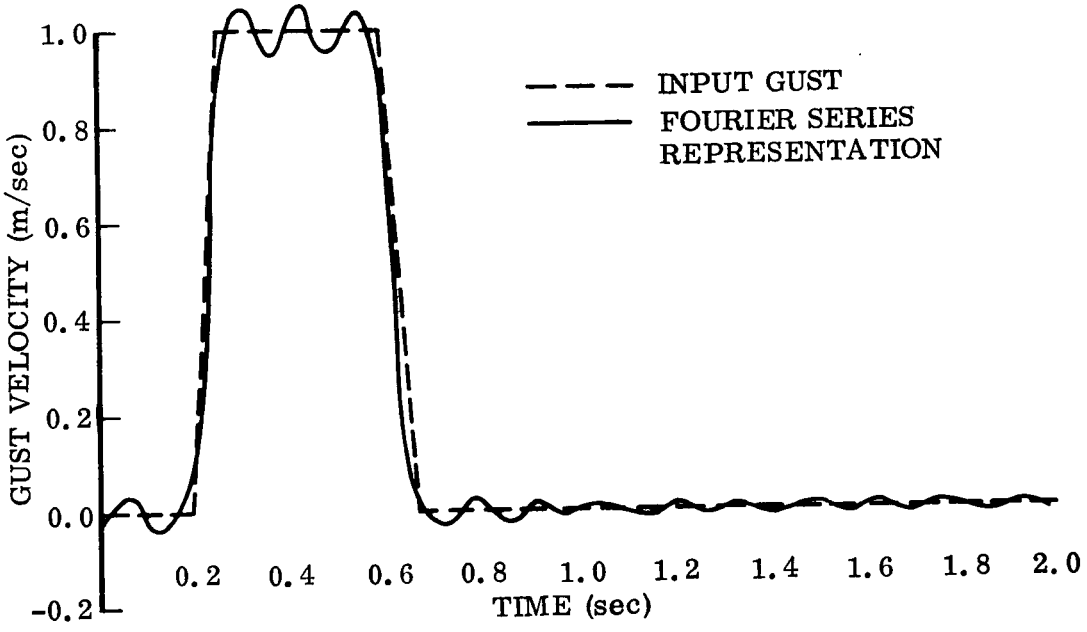

Figure 2-9. Discrete Gust Time History

A pitch plane stability augmentation system (SAS) was incorporated into the symmetric analysis for comparison with the unaugmented vehicle response. The SAS block diagram is shown in Figure 2-10. The SAS effects are included by modifying the A-matrix in Equation 20. The procedure for doing this is given in detail in Reference 1.

Propellant sloshing parameters for the booster at t = 60 and 75 seconds are shown in Table 2-4. These values were determined by the method of Reference 8. These modes were mass coupled to the vehicle modes as described in Reference 1.

Table 2-4. Sloshing Parameters

Time (sec)	Tank	Slosh Mass (kg)	Slosh Spring (N/m)	Slosh cg (m)
60	LO_2	205,100	1,162,000	44.0
	LH_2	12,720	72,000	71.3
75	LO_2	205,100	1,211,000	44.8
	LH_2	12,720	75,100	74.4

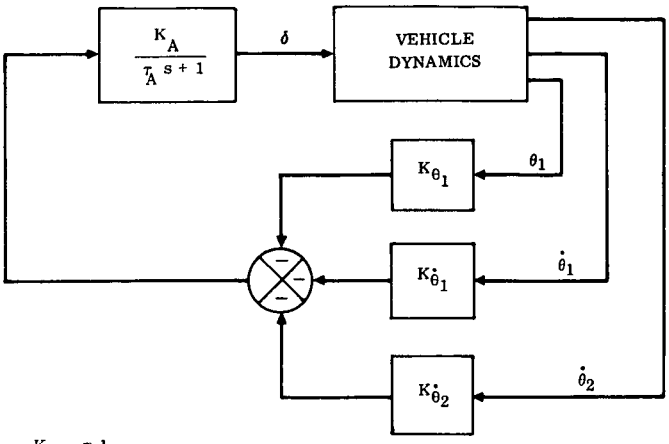

$K_A = 1$

$\tau_A = 0.04$ sec

$K_{\theta_1} = 1$

$K_{\dot{\theta}_1} = 0.35$ sec

$K_{\dot{\theta}_2} = 0.35$ sec

SENSOR NO. 1 LOCATED AT BOOSTER NOSE (STATION 25.4m)

SENSOR NO. 2 LOCATED AT BOOSTER ENGINE GIMBAL (STATION 154.0m)

Figure 2-10. Pitch Plane SAS

Responses were computed for the analysis conditions of Table 1-1 for the following items:

1. Booster wing root shear
2. Booster wing root bending moment
3. Booster wing root torque (about booster station 84.0m)
4. Booster wing tip acceleration
5. Booster body acceleration at booster station 29.2m
6. Booster body acceleration at booster station 44.6m
7. Booster body acceleration at booster station 59.1m
8. Booster body acceleration at booster station 76.9m
9. Booster body acceleration at booster station 99.2m
10. Orbiter body acceleration at orbiter station 5.08m
11. Orbiter body acceleration at orbiter station 24.6m
12. Orbiter body acceleration at orbiter station 45.2m
13. Orbiter body acceleration at orbiter station 68.5m

Representative transfer functions are shown in Figures 2-11 through 2-32. All transfer functions shown herein pertain to flight at Mach 1.2. (Each figure contains three sets of symbols, corresponding to one degree of freedom, total rigid body response, and total response including sloshing and elastic modes.) The one degree of freedom cases represent vertical translation and side translation for the symmetric and antisymmetric conditions, respectively.

Figure 2-11 through 2-16 apply to the symmetric flight condition with the SAS off and booster aerodynamic surfaces intact (Conditions 1 and 2 in Table 1-1). Corresponding plots with the SAS on (Condition 3) are given in Figures 2-17 through 2-22. Antisymmetric transfer functions for Conditions 5 and 6 (SAS off, booster aerodynamic surfaces on) are contained in Figures 2-23 through 2-28. Transfer functions for the conditions having booster aerodynamic surfaces removed are shown in Figures 2-29 and 2-30 for the symmetric case and 2-31 and 2-32 for the antisymmetric condition.

The transfer function peaks can generally be seen to coincide with vehicle resonant frequencies. In some instances, however, a peak occurs at a frequency well above the highest modal value. This can be seen for example in Figure 2-15. These high-frequency peaks, probably due to aerodynamic coupling, do not appreciably affect the results, however. In the random case, this is due to the fact that the turbulence spectrum drops off rapidly with frequency. Figure 2-33 shows the response power spectral density for the transfer function of Figure 2-15. Note that the high-frequency peak is now two orders of magnitude below the peak at 2.2 Hz. In fact, the random response parameter, $\bar{A}$, in all cases had leveled off at 5 Hz. Therefore, 5 Hz was used as the cutoff frequency in evaluating $\bar{A}$ and N_0 by Equations 26 and 27.

In the discrete analyses, since the gust wavelength was established so as to excite the vehicle fundamental structural mode, the high-frequency peak in the transfer functions had no appreciable effect on the response time histories.

Results of the random analysis are summarized in Tables 2-5 through 2-10. Tables 2-5 and 2-6 give the $\bar{A}$ and N_0 values respectively for one degree of freedom. Corresponding rigid body results are listed in Tables 2-7 and 2-8. The total $\bar{A}$ and N_0 values are listed in Tables 2-9 and 2-10, respectively.

The total $\bar{A}$ values of booster body and orbiter body acceleration are shown graphically in Figures 2-34 and 2-35 respectively for the conditions with booster aerodynamic surfaces intact. Figure 2-34 shows that symmetrically the maximum acceleration on the booster occurs at 0.8 Mach number. It also shows the effectiveness of the SAS in reducing the accelerations at 1.2 Mach number. The SAS reduces the booster rms nose acceleration by 38% and the rms tail acceleration by 7%. In the antisymmetric case, the booster body rms side acceleration at the nose is the same at Mach 0.8 and Mach 1.2. At the aft end, however, the rms acceleration is higher at Mach 1.2 by

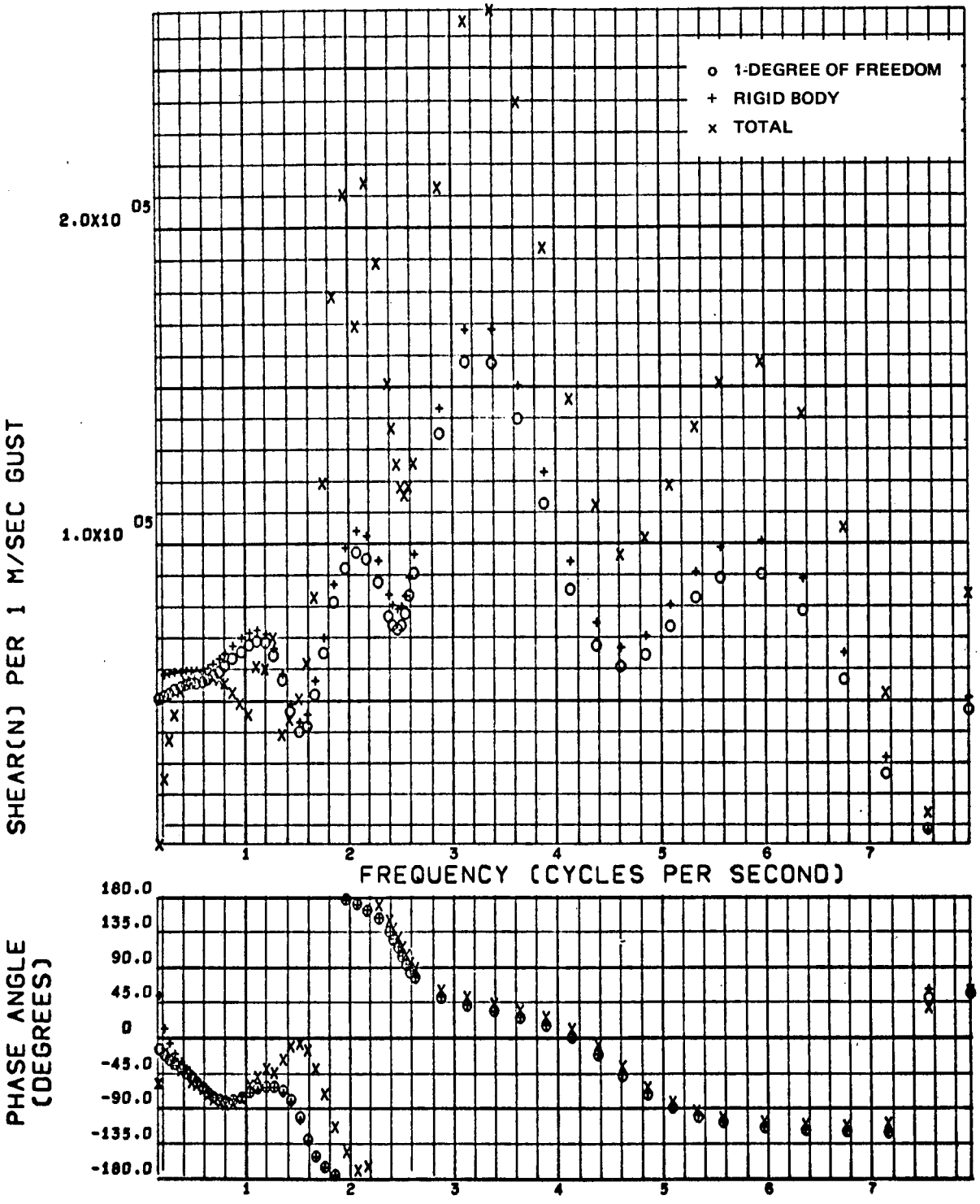

Figure 2-11. Booster Wing Root Shear Symmetric Transfer Function, M = 1.2

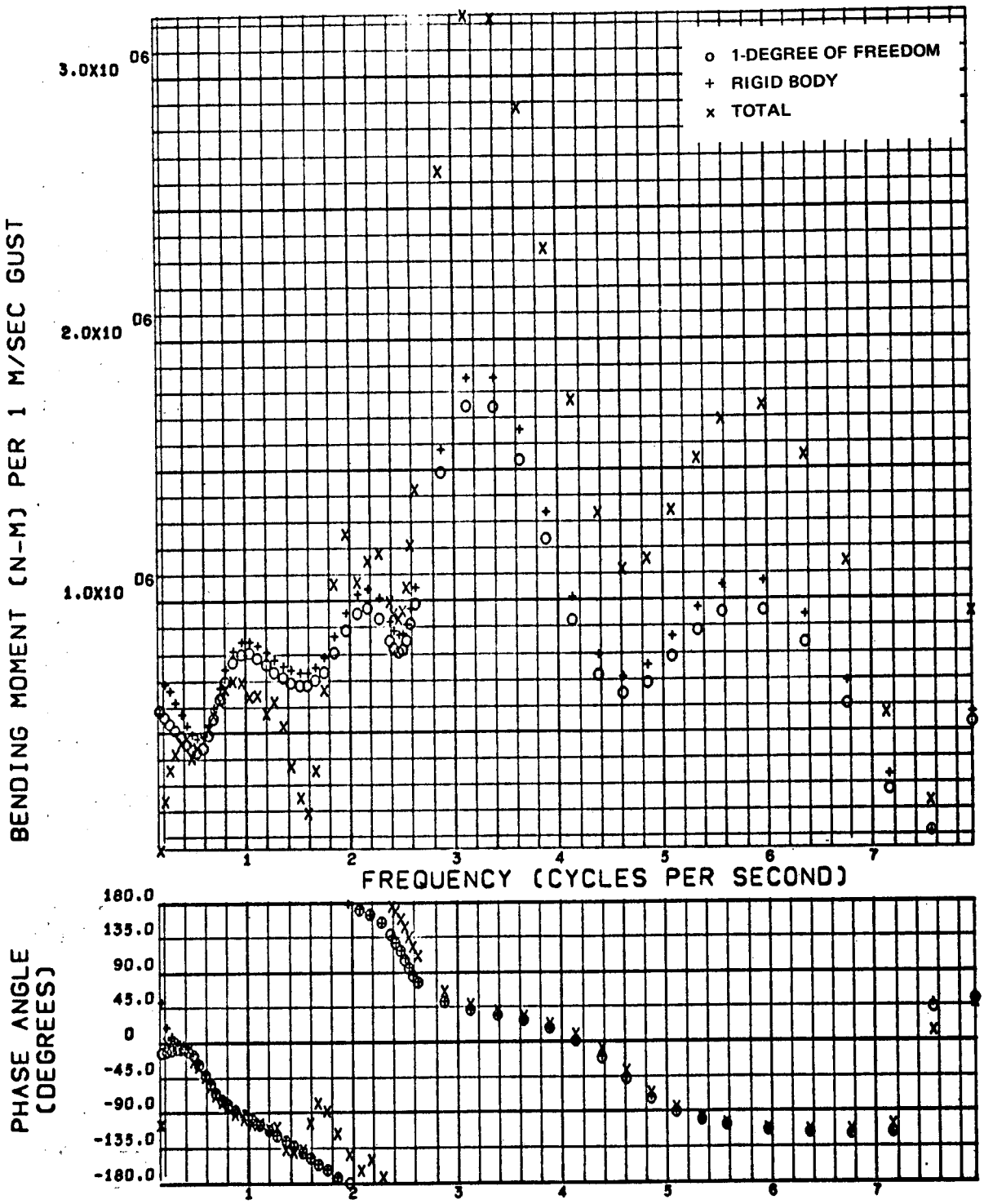

Figure 2-12. Booster Wing Root Bending Moment Symmetric Transfer Function, M = 1.2

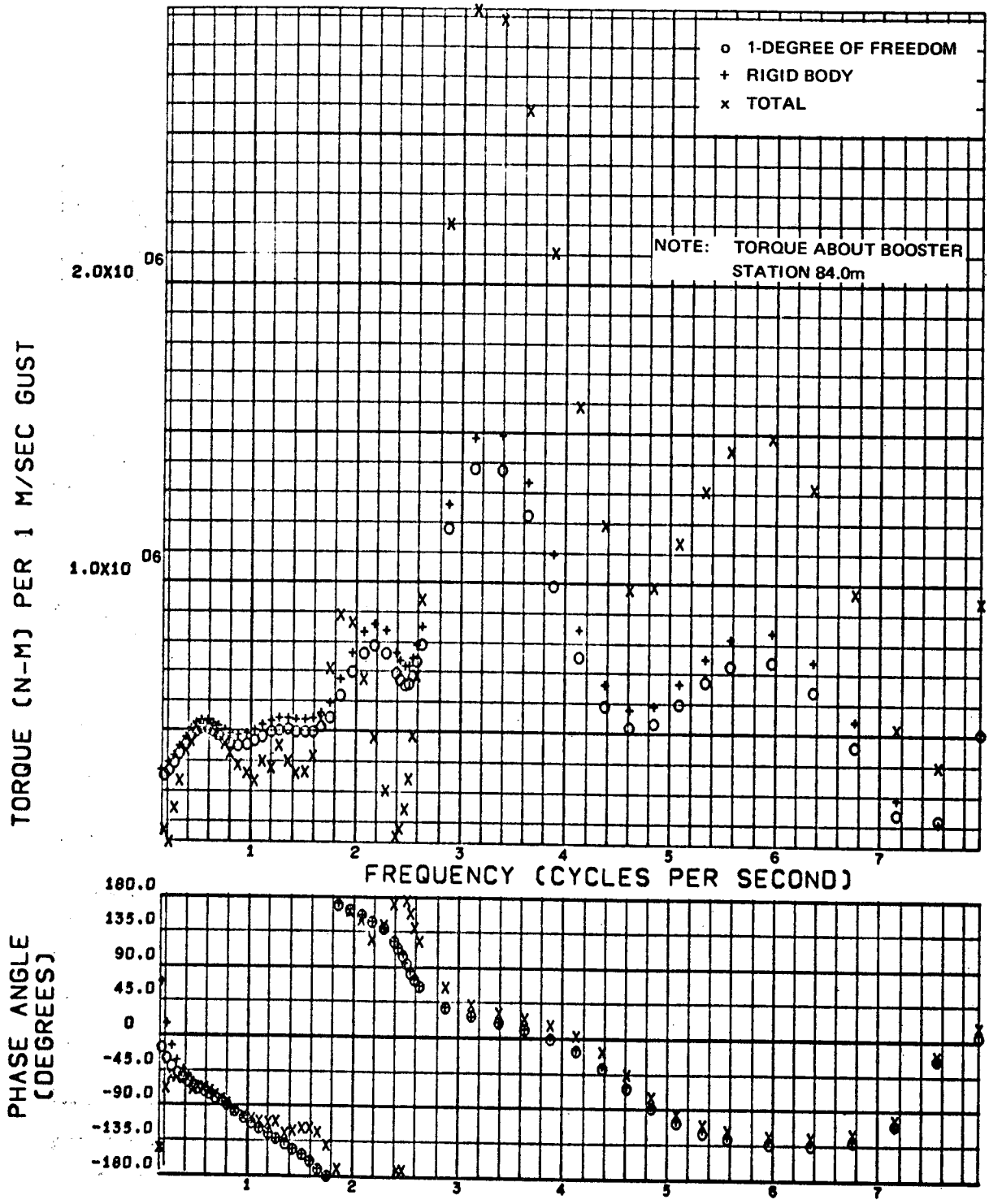

Figure 2-13. Booster Wing Root Torque Symmetric Transfer Function, M = 1.2

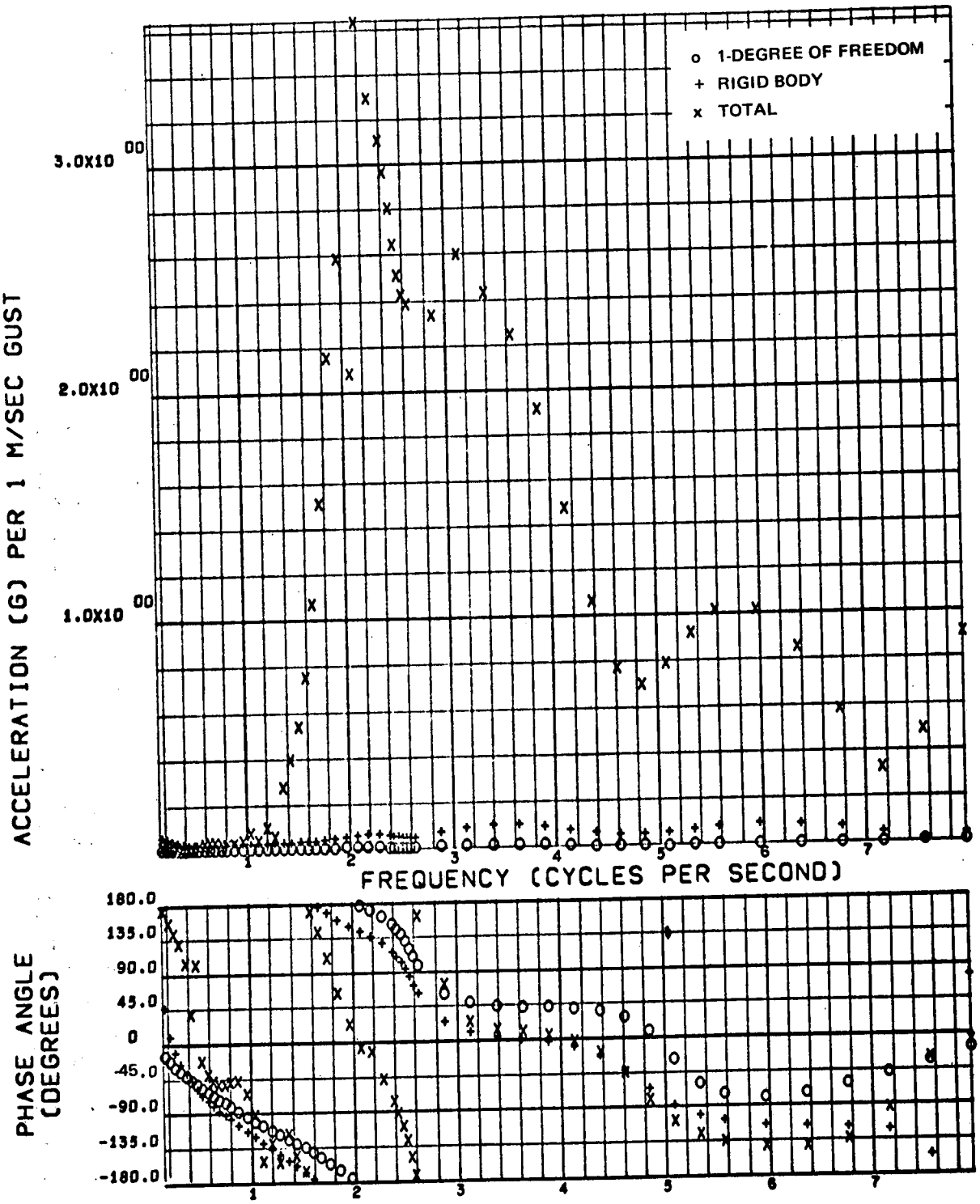

Figure 2-14. Booster Wing Tip Acceleration Symmetric Transfer Function, M = 1.2

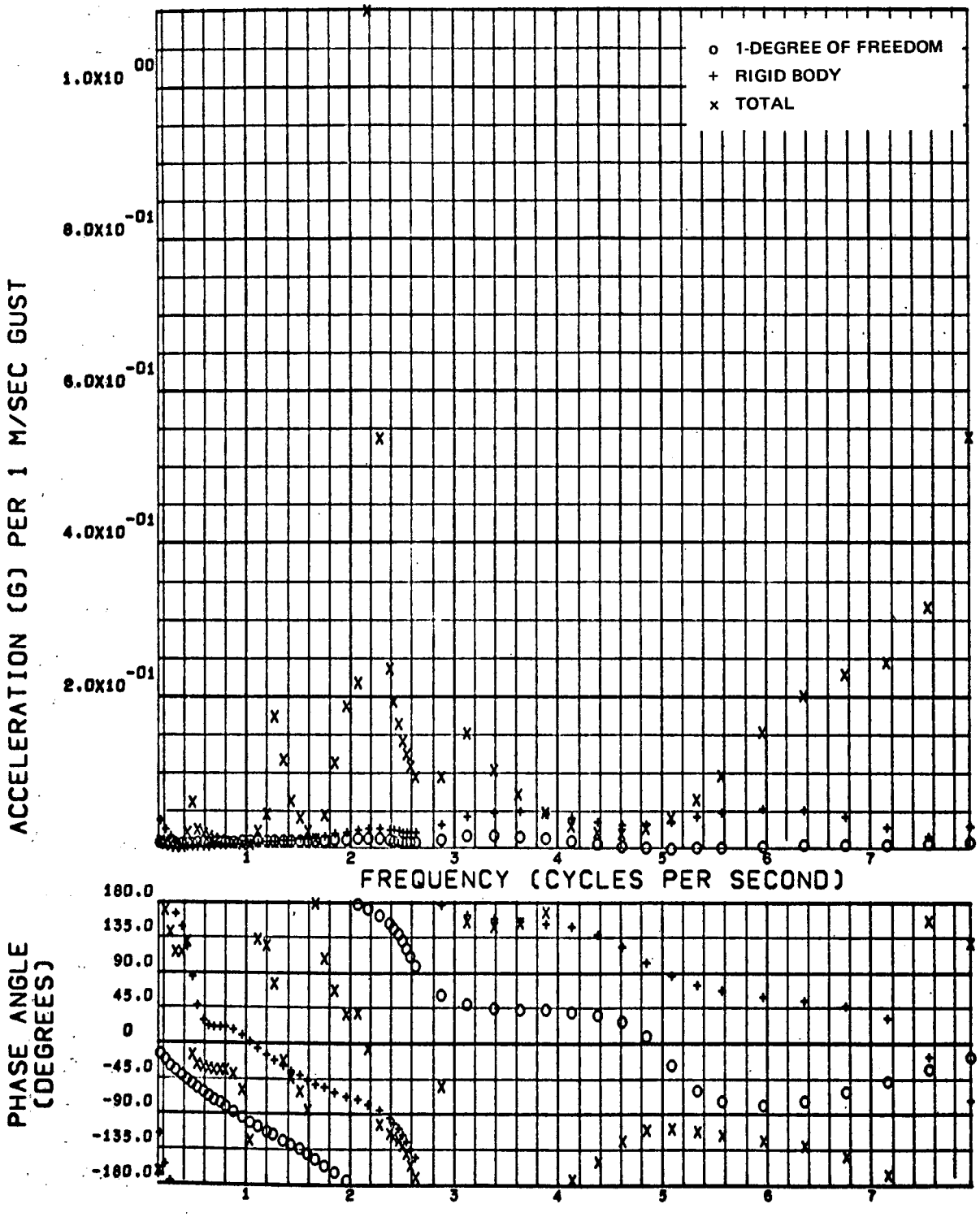

Figure 2-15. Booster Body Acceleration Symmetric Transfer Function, Booster Station 29.2 m, M = 1.2

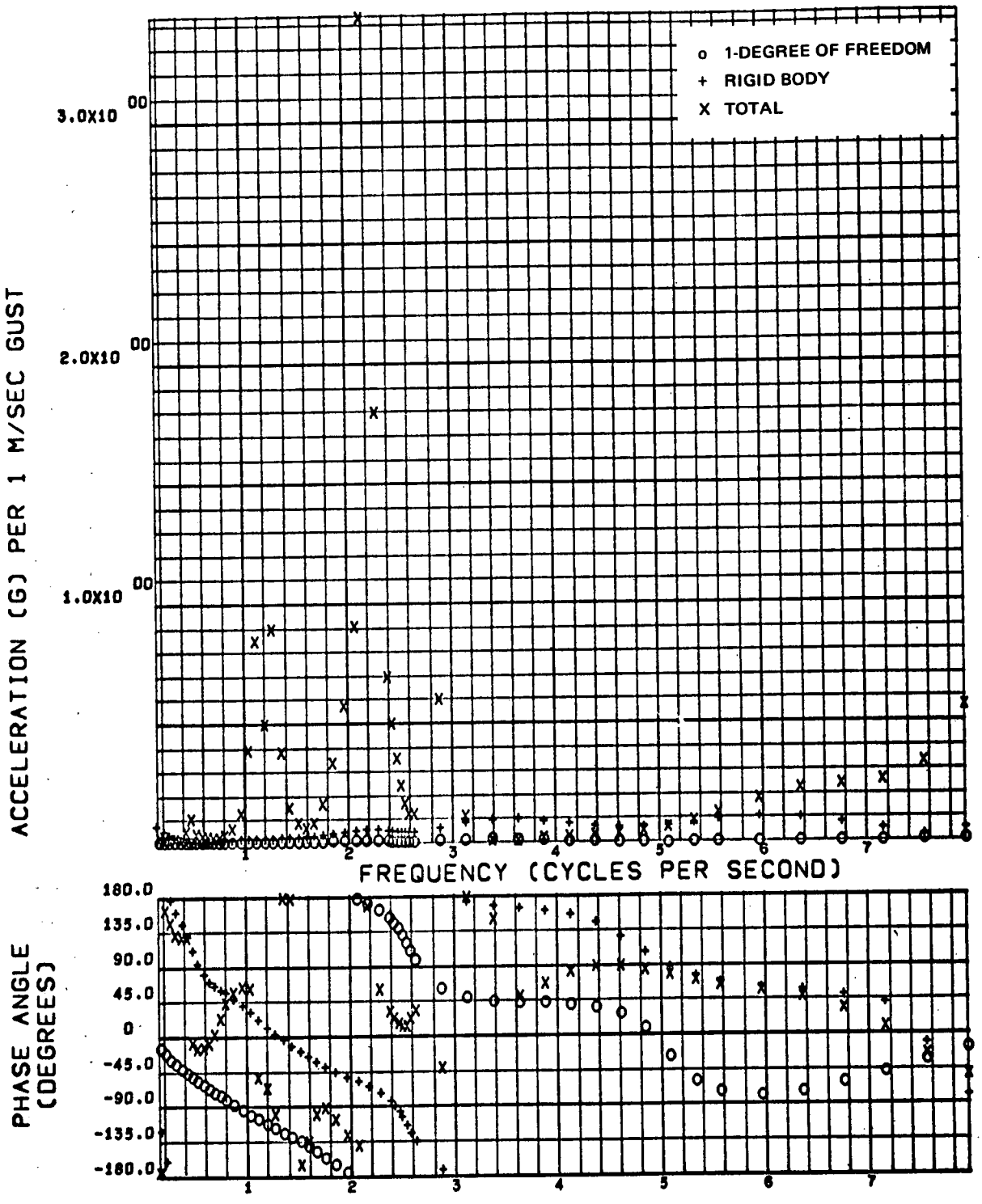

Figure 2-16. Orbiter Body Acceleration Symmetric Transfer Function, Orbiter Station 5.08 m, M = 1.2

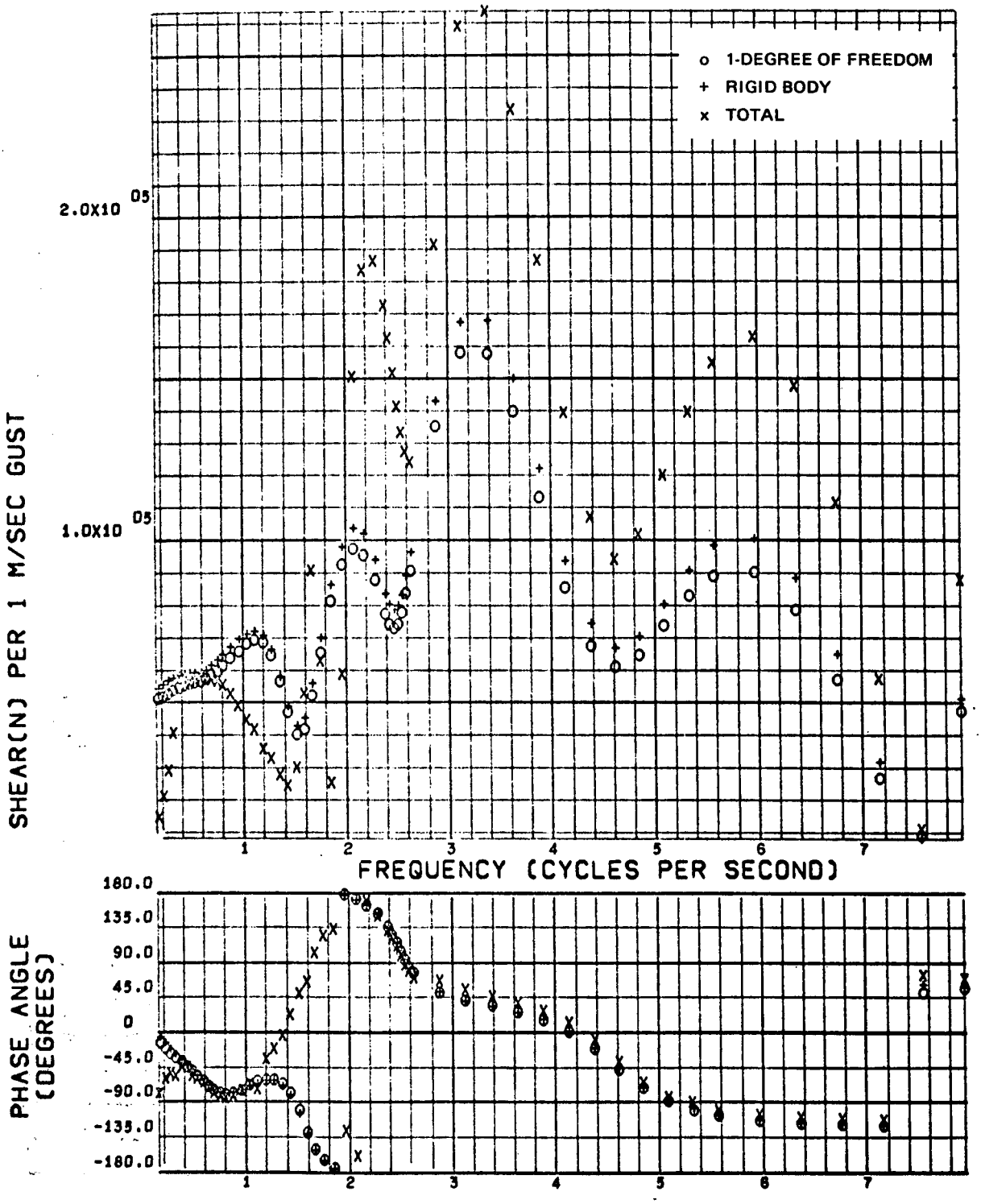

Figure 2-17. Booster Wing Root Shear Symmetric Transfer Function, M = 1.2, SAS on

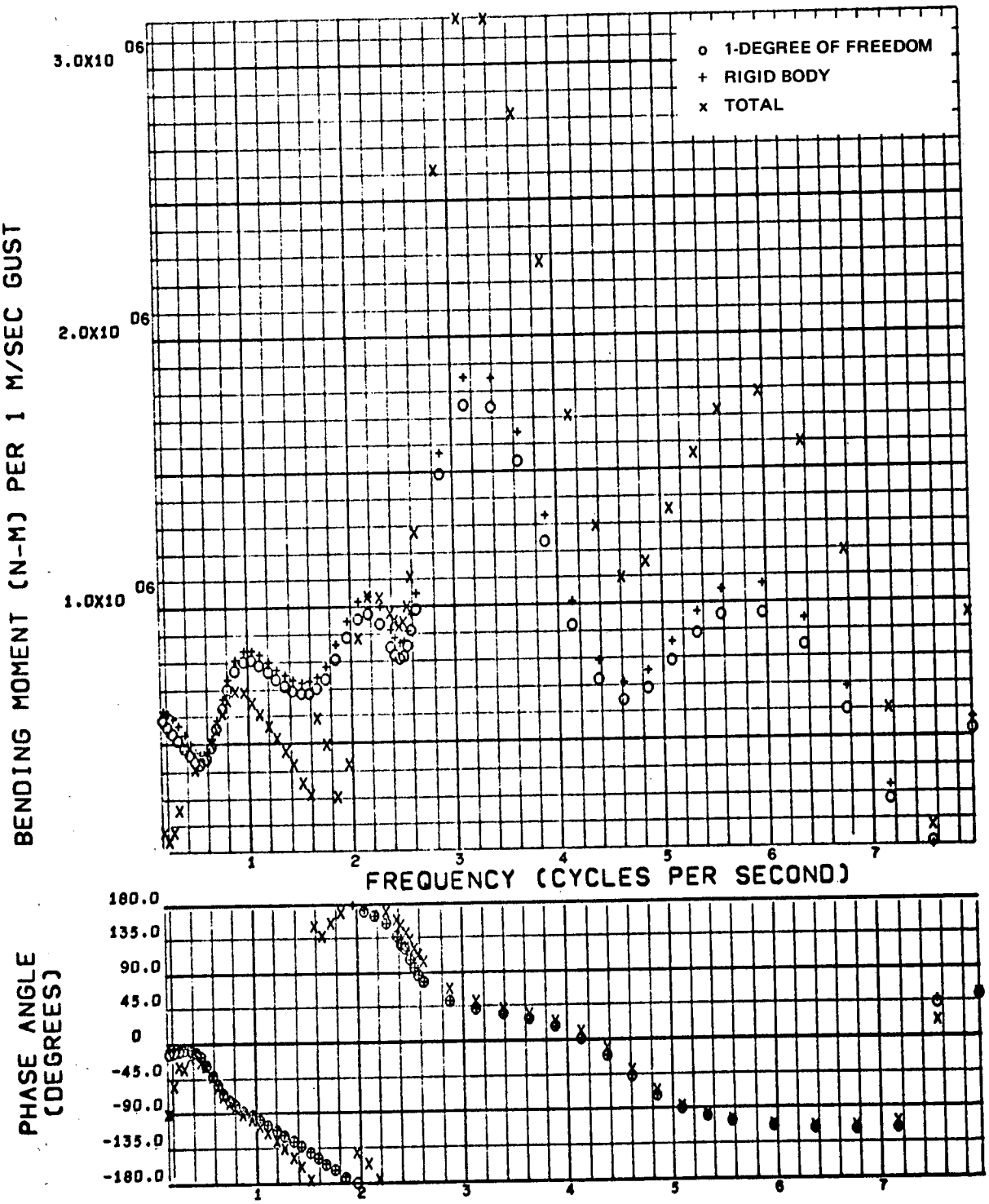

Figure 2-18. Booster Wing Root Bending Moment Symmetric Transfer Function, M = 1.2, SAS on

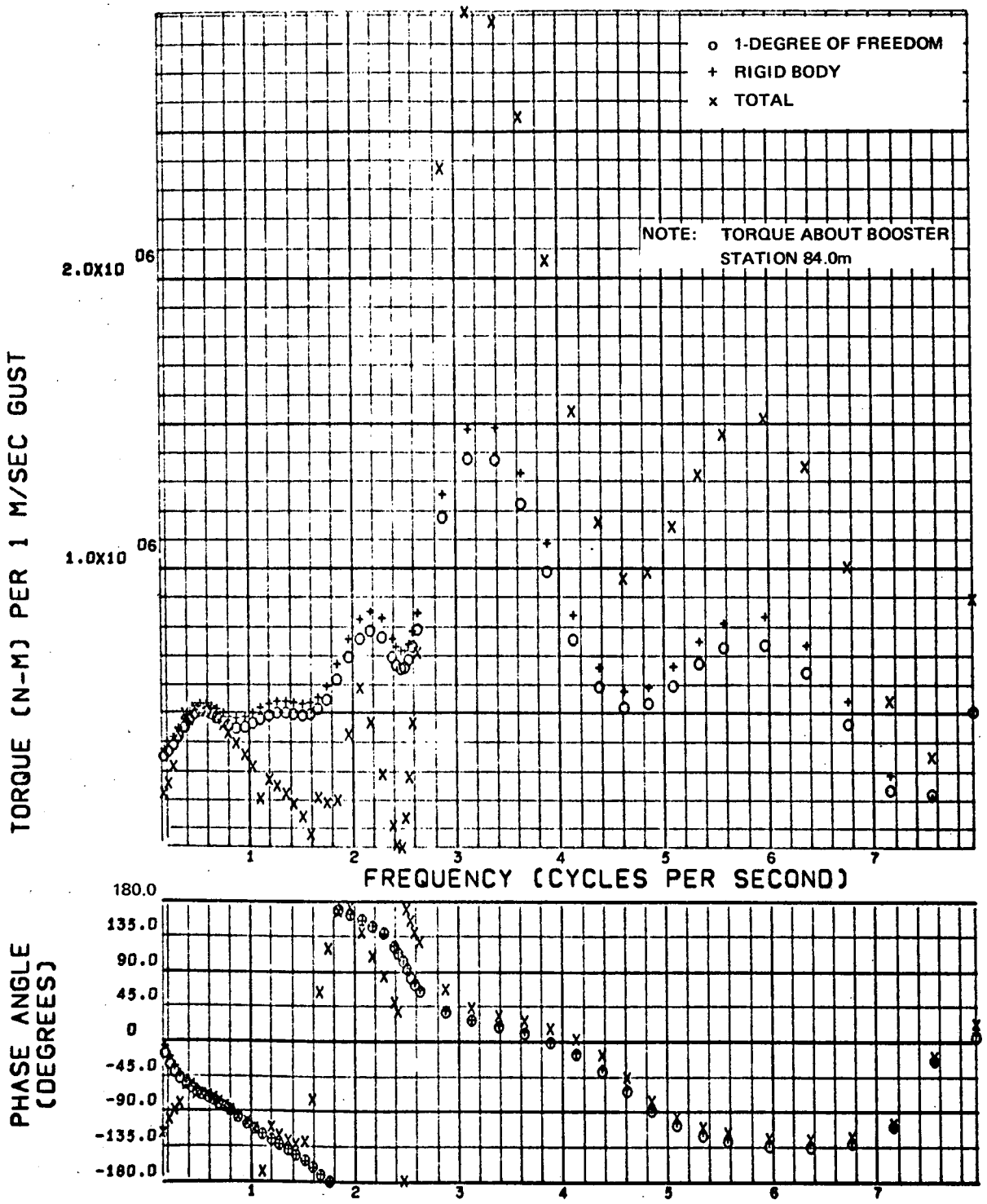

Figure 2-19. Booster Wing Root Torque Symmetric Transfer Function, M = 1.2, SAS on

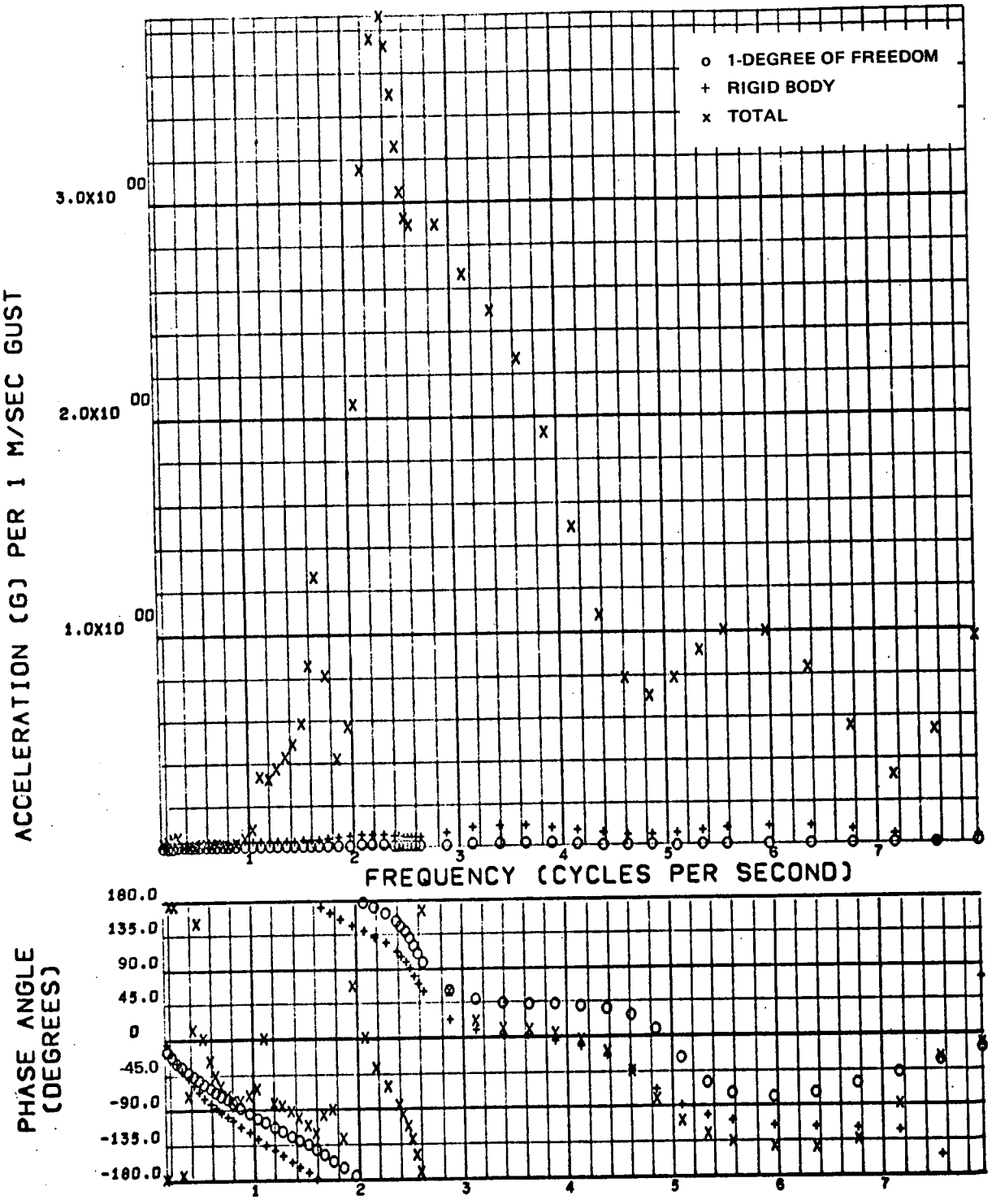

Figure 2-20. Booster Wing Tip Acceleration Symmetric Transfer Function, M = 1.2, SAS on

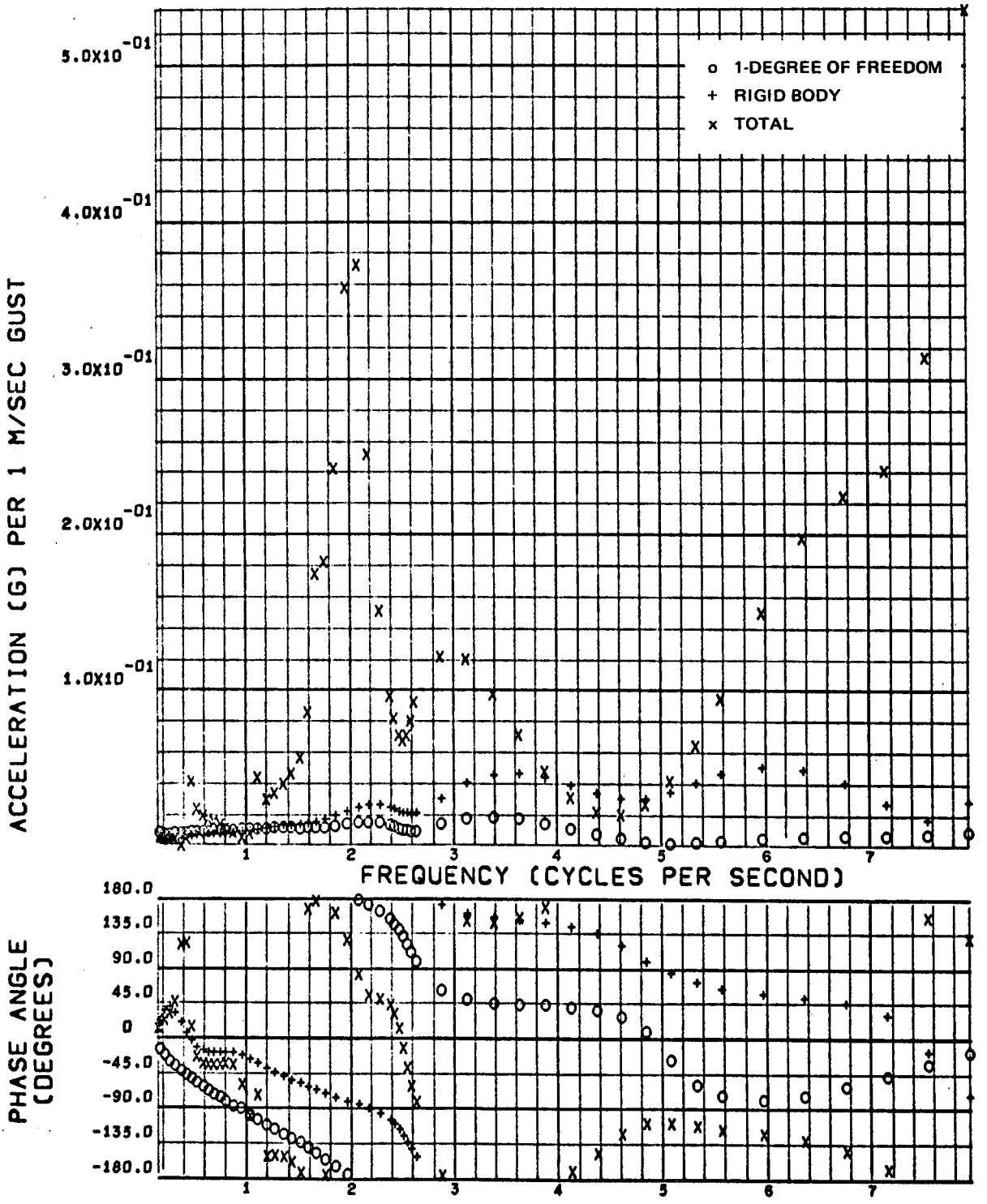

Figure 2-21. Booster Body Acceleration Symmetric Transfer Function, Booster Station 29.2 m, M = 1.2, SAS on

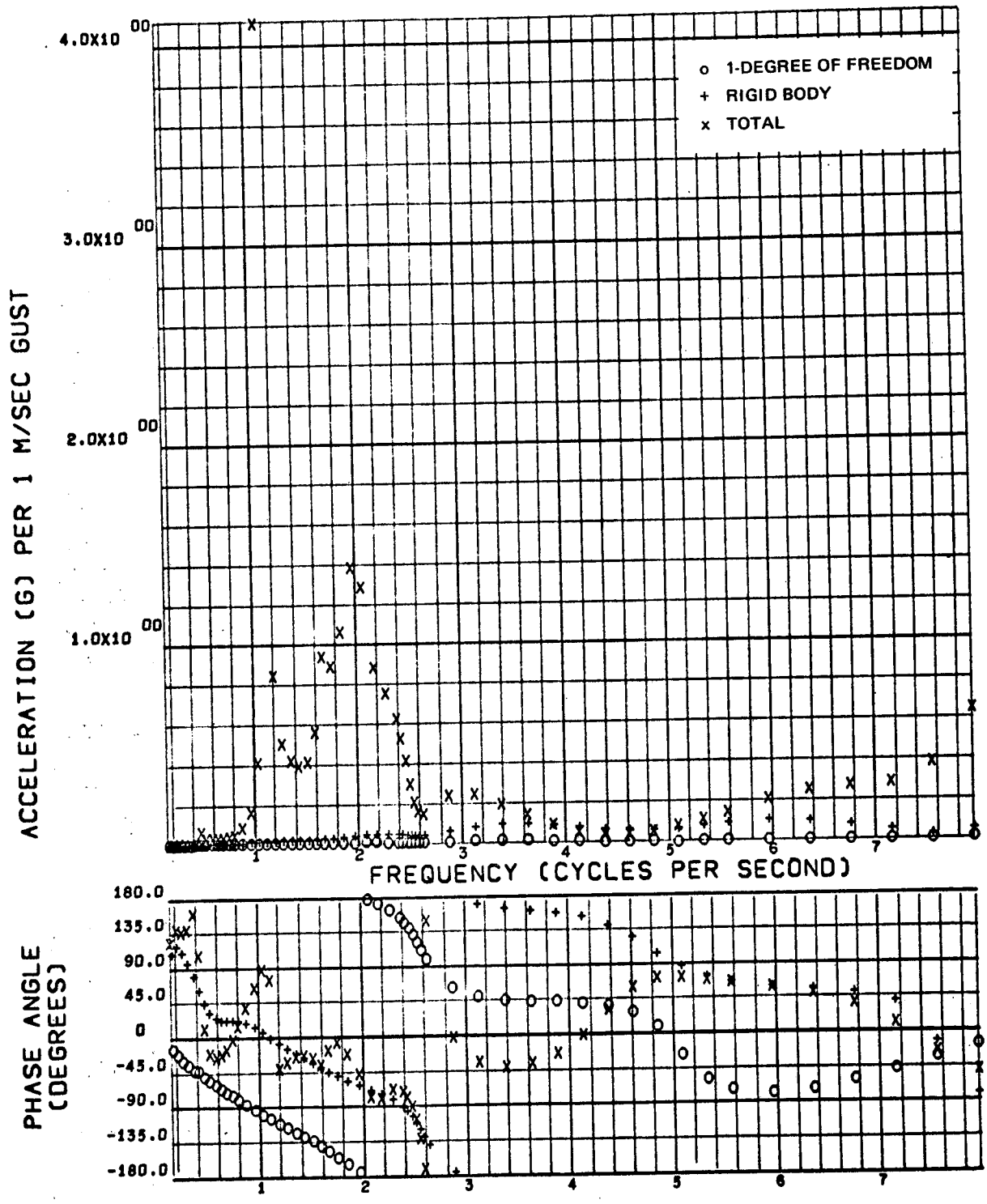

Figure 2-22. Orbiter Body Acceleration Symmetric Transfer Function, Orbiter Station 5.08 m, M = 1.2, SAS on

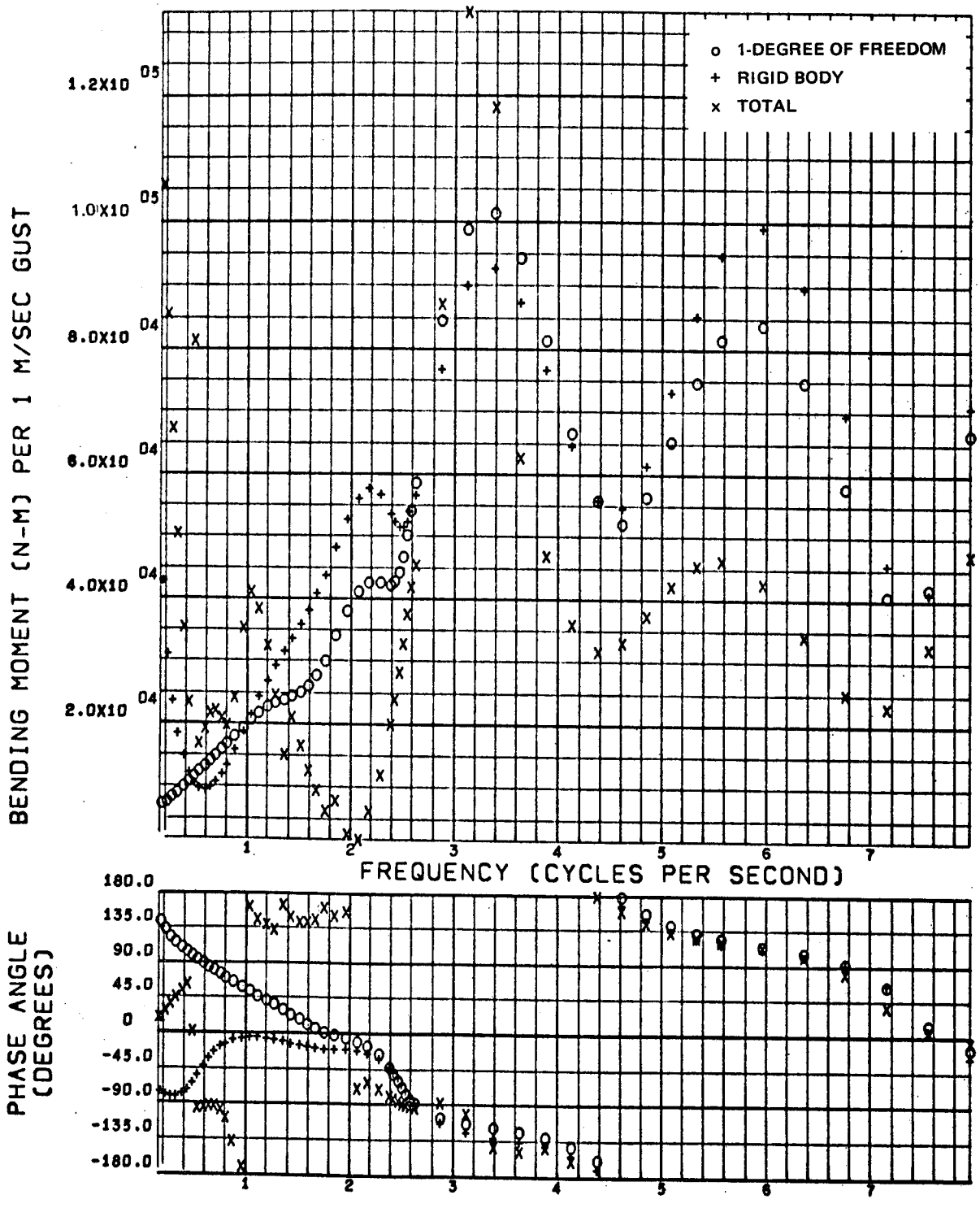

Figure 2-23. Booster Wing Root Bending Moment Antisymmetric Transfer Function, M = 1.2

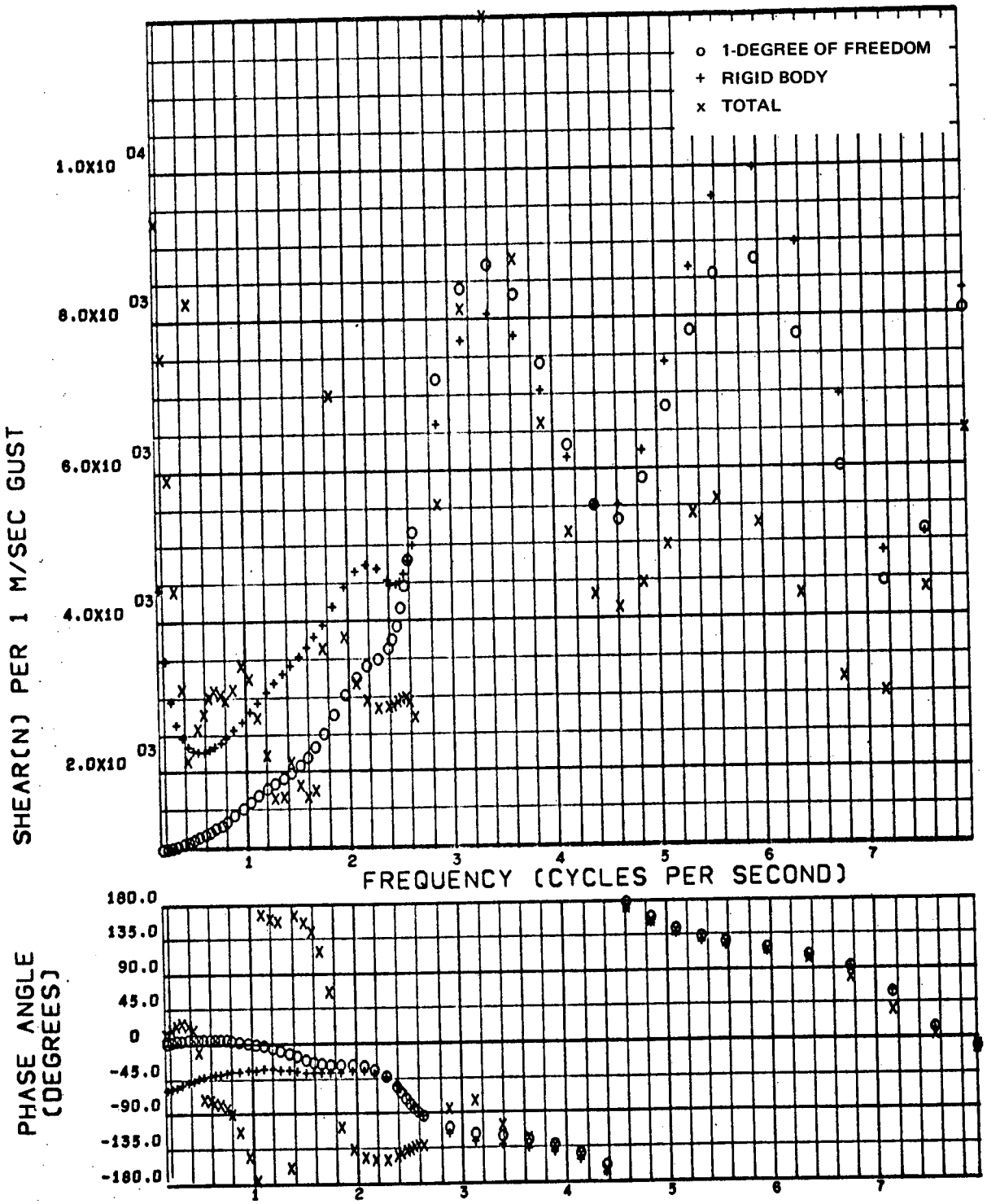

Figure 2-24. Booster Wing Root Shear Antisymmetric Transfer Function, M = 1.2

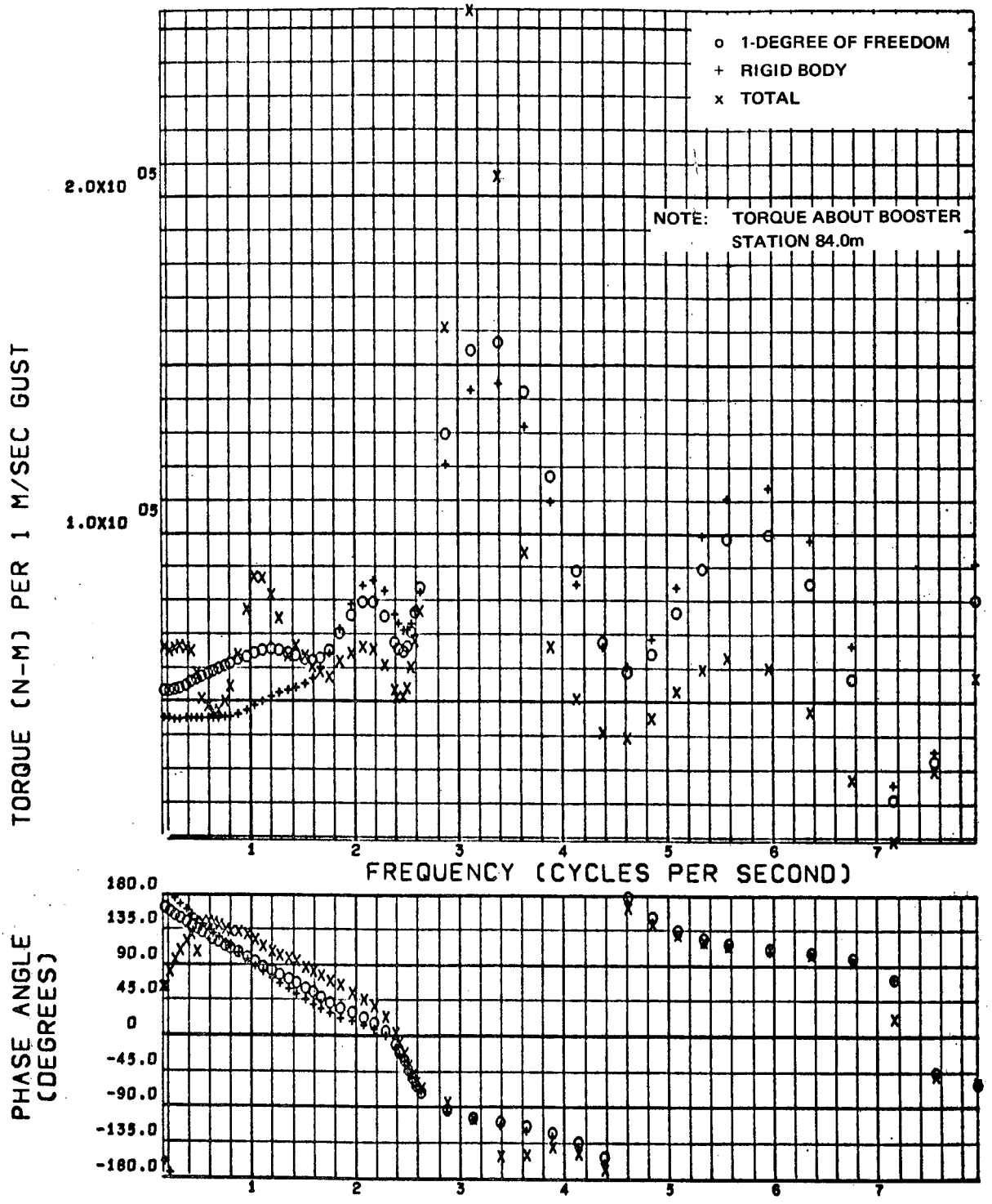

Figure 2-25. Booster Wing Root Torque Antisymmetric Transfer Function, M = 1.2

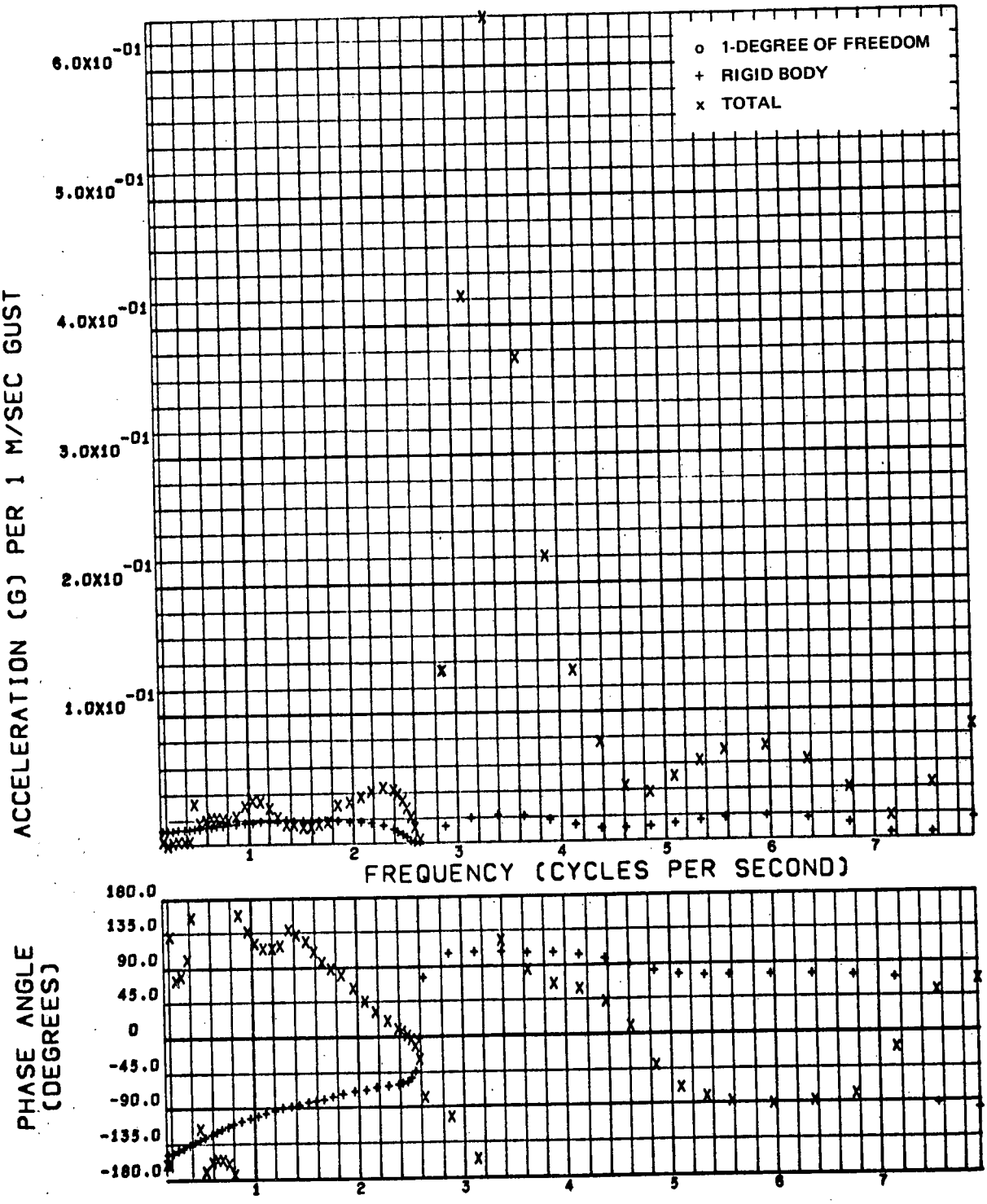

Figure 2-26. Booster Wing Tip Acceleration Antisymmetric Transfer Function, M = 1.2

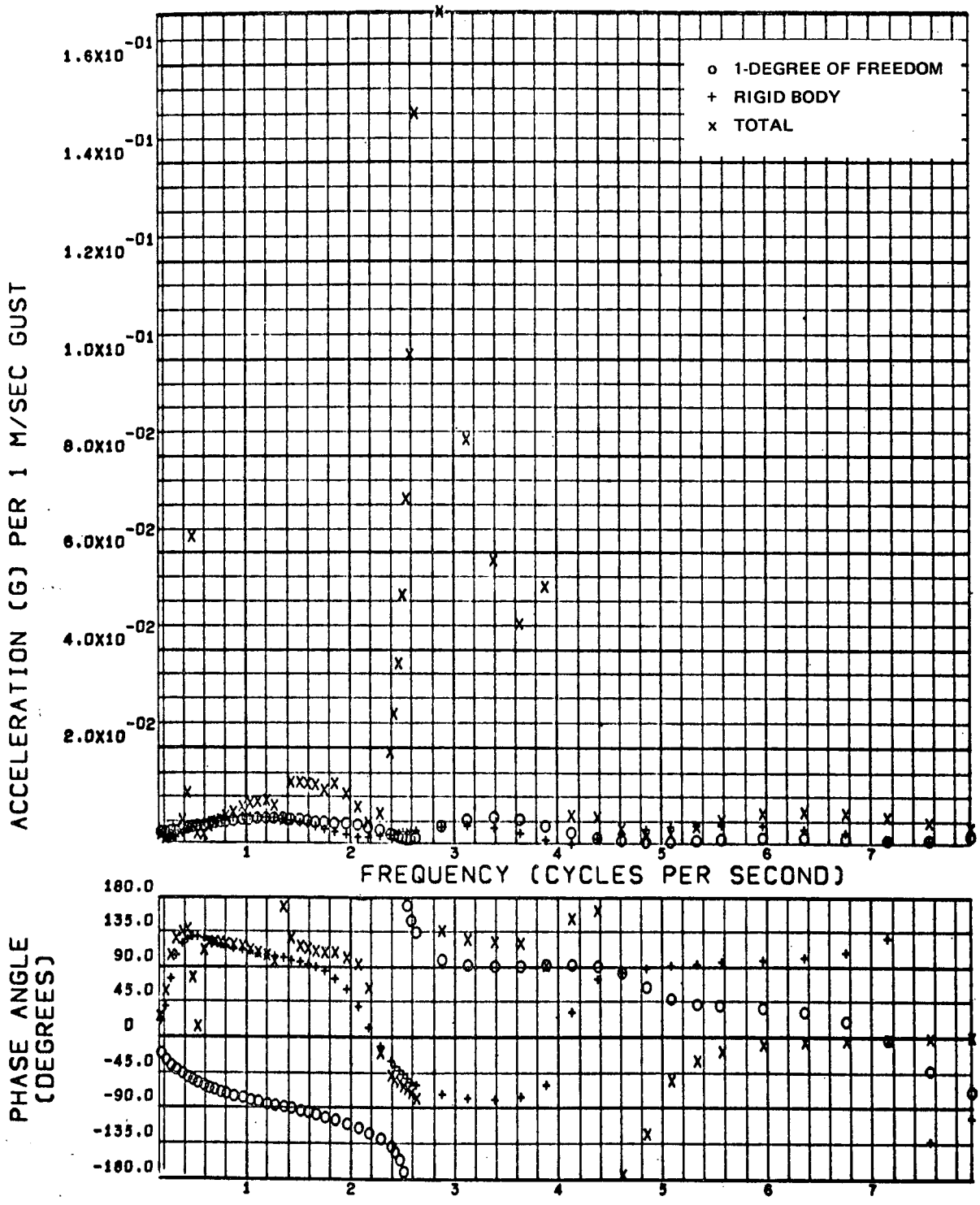

Figure 2-27. Booster Body Acceleration Antisymmetric Transfer Function, Booster Station 29.2 m, M = 1.2

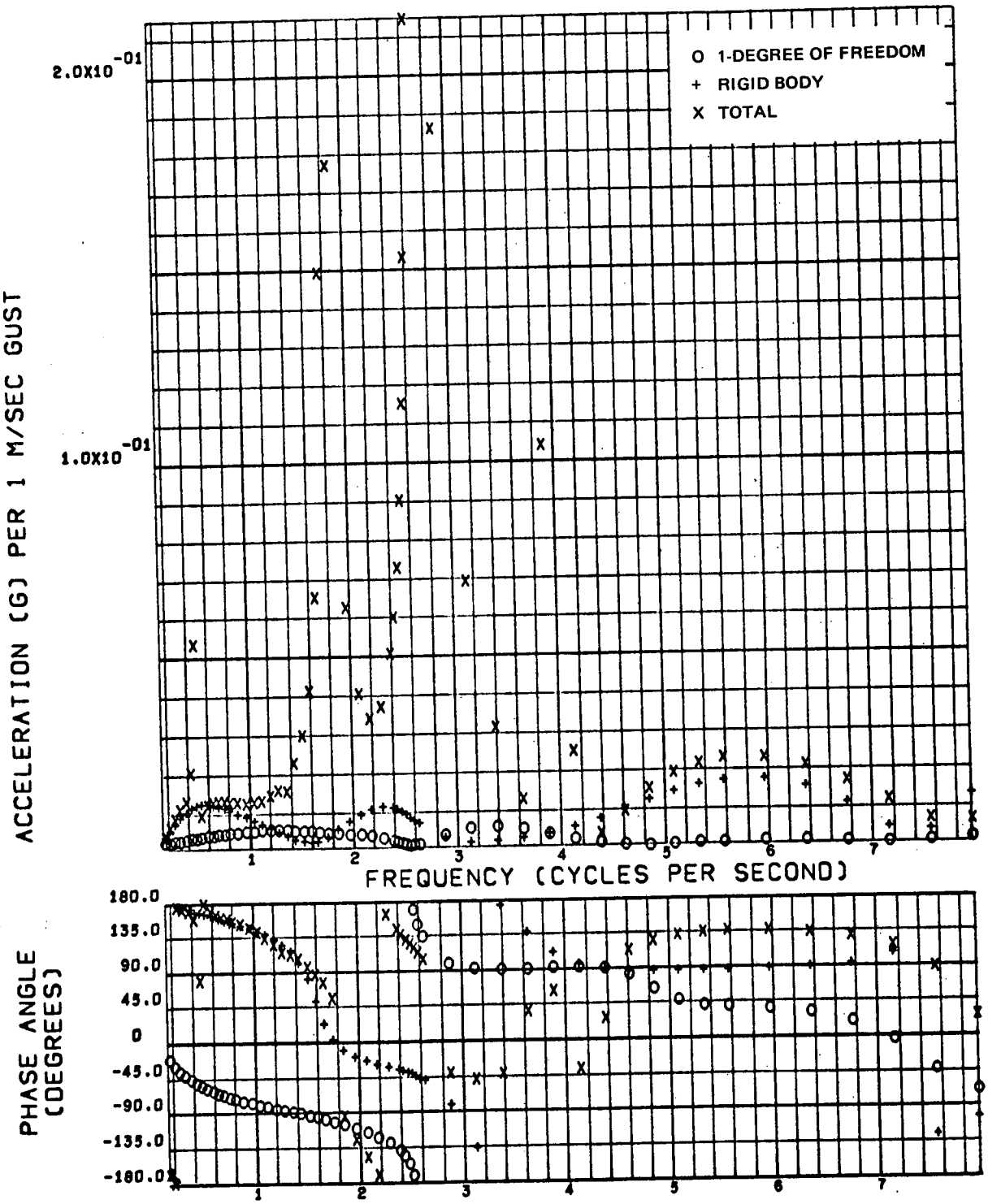

Figure 2-28. Orbiter Body Acceleration Antisymmetric Transfer Function, Orbiter Station 5.08 m, M = 1.2

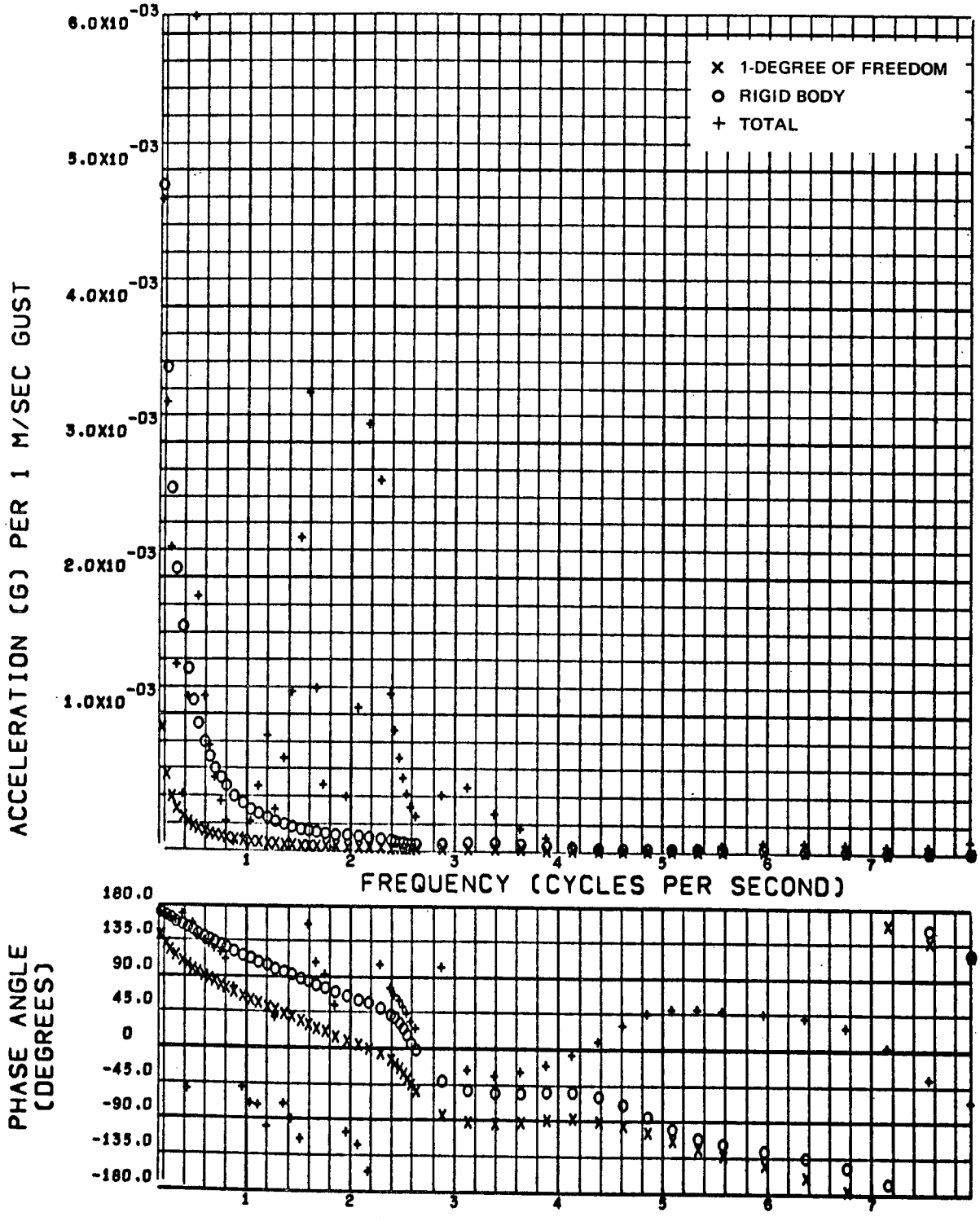

Figure 2-29. Booster Body Acceleration Symmetric Transfer Function, Booster Station 29.2m, M = 1.2, Booster Aerodynamic Surfaces Removed

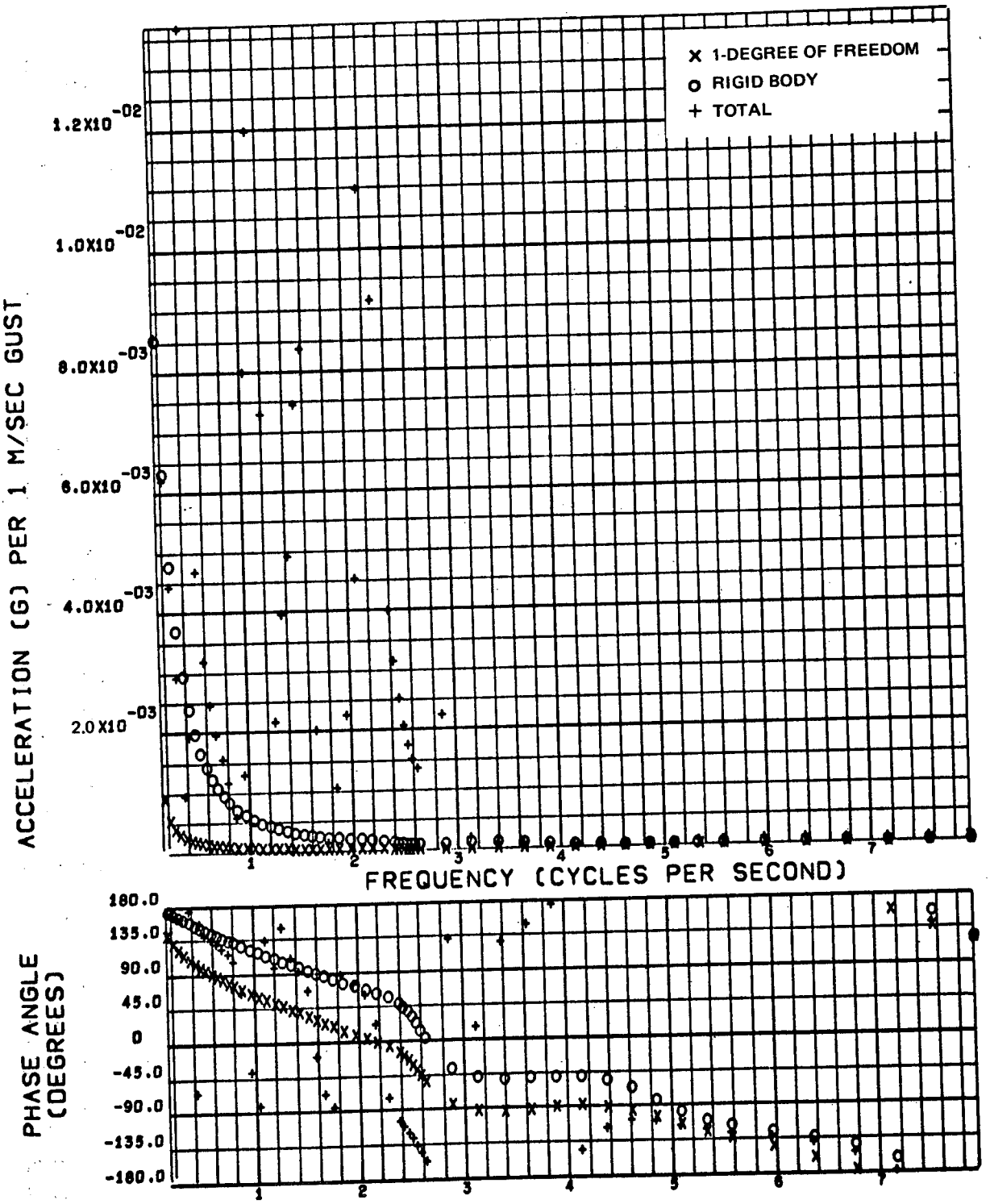

Figure 2-30. Orbiter Body Acceleration Symmetric Transfer Function, Orbiter Station 5.08m, M = 1.2, Booster Aerodynamic Surfaces Removed

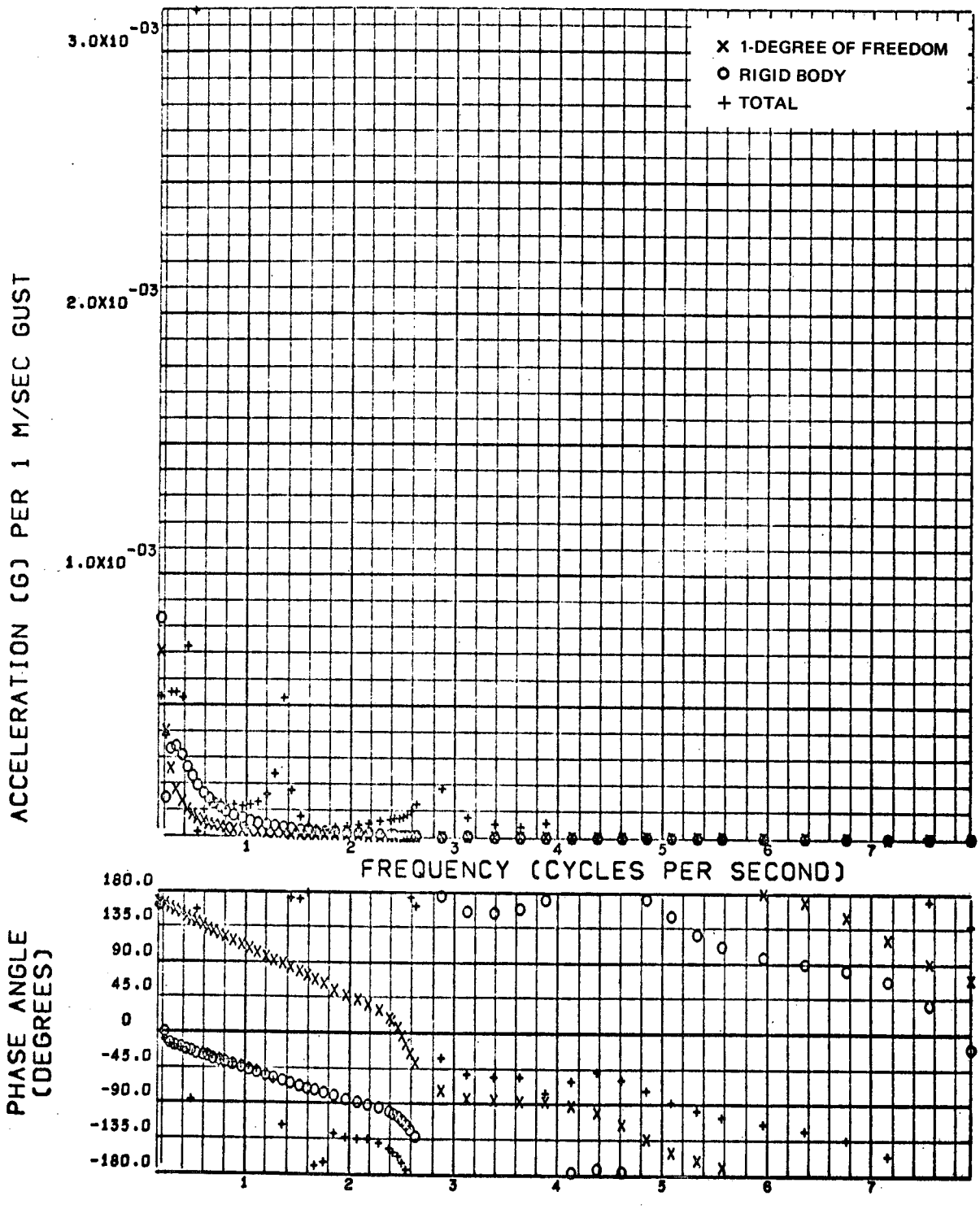

Figure 2-31. Booster Body Acceleration Antisymmetric Transfer Function, Booster Station 29.2m, M = 1.2, Booster Aerodynamic Surfaces Removed

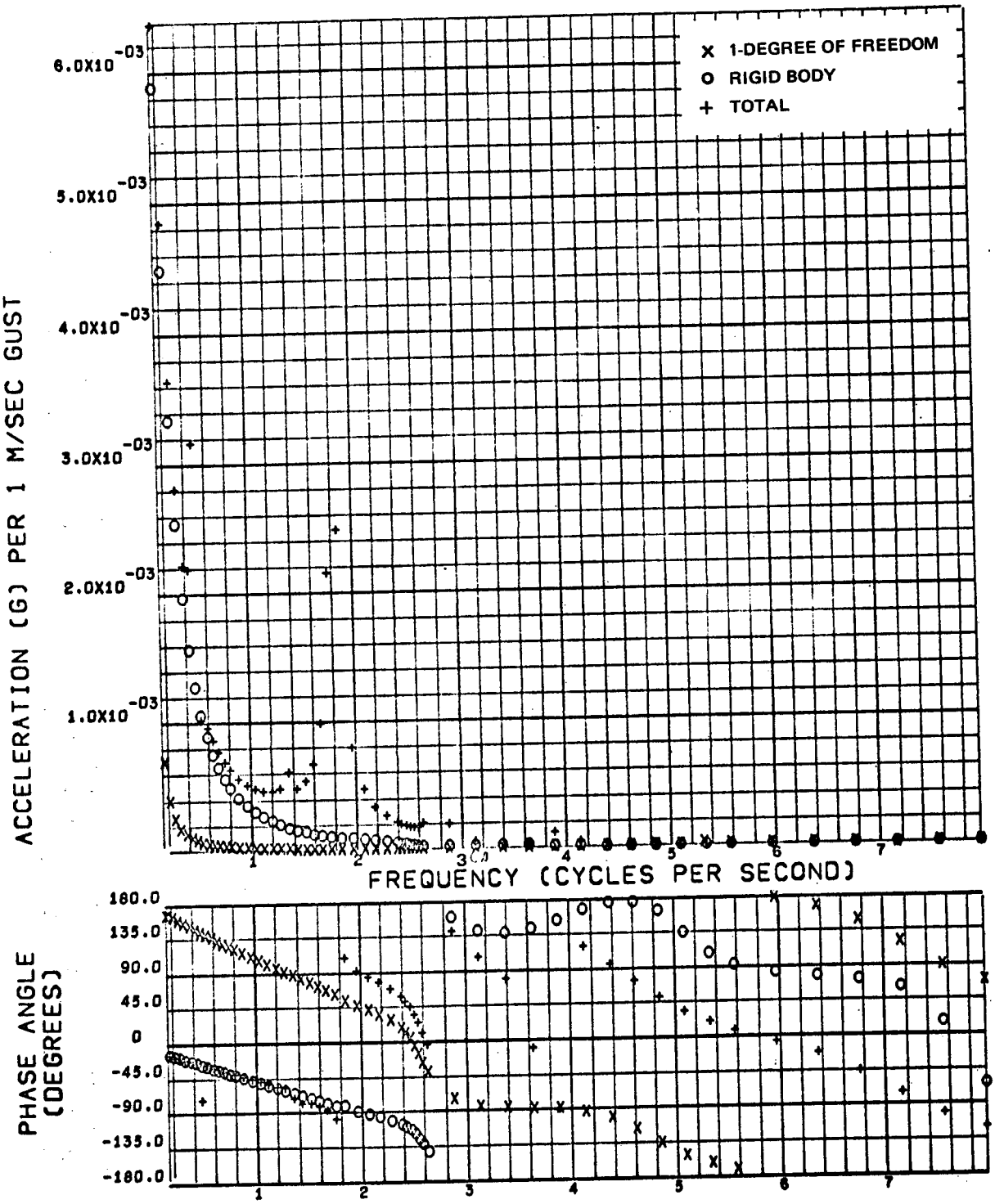

Figure 2-32. Orbiter Body Acceleration Antisymmetric Transfer Function, Orbiter Station 5.08m, M = 1.2, Booster Aerodynamic Surfaces Removed

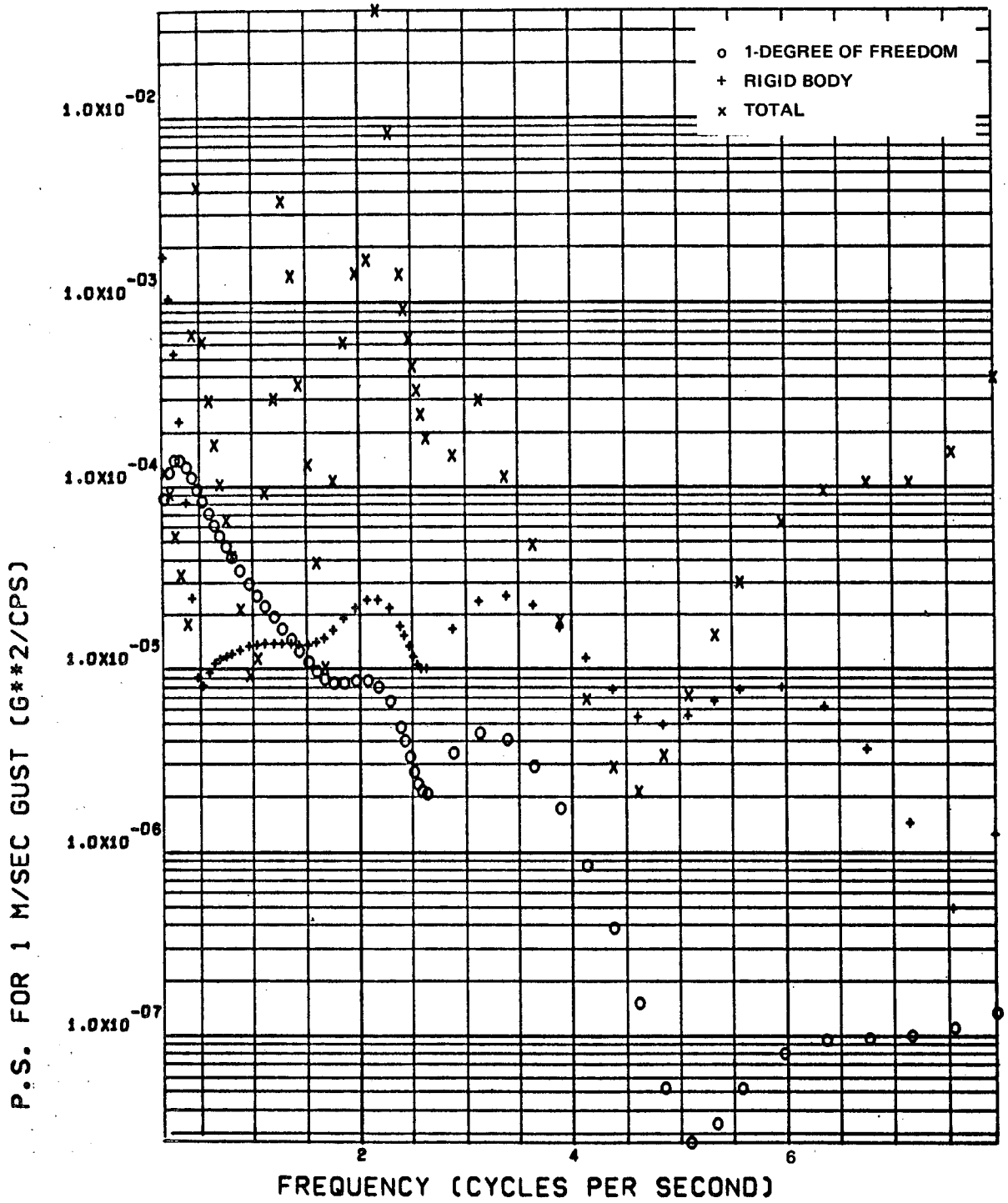

Figure 2-33. Booster Body Acceleration Symmetric Power Spectral Density, Booster Station 29.2m, M = 1.2

Table 2-5. 1 Degree of Freedom $\bar{A}$ Values

Response Item	Condition No.								
	2	3	4	5	7	8	9	10	11
Booster Wing									
Root Shear (10^3N)	56.84	56.84	—	1.659	—	55.66	—	2.522	—
Root Bending Moment (10^4N-m)	57.45	57.45	—	1.861	—	61.15	—	2.872	—
Root Torque* (10^4N-m)	46.33	46.33	—	5.725	—	34.86	—	4.325	—
Tip Acceleration (10^{-2}g)	0.937	0.937	—	0.0	—	0.483	—	0.0	—
Booster Body Acceleration (10^{-2}g)									
Booster Station 29.2m			0.031	0.385	0.021		0.047	0.301	0.054
Booster Station 44.6m									
Booster Station 59.1m									
Booster Station 76.9m									
Booster Station 99.2m									
Orbiter Body Acceleration (10^{-2}g)									
Orbiter Station 5.08m									
Orbiter Station 24.6m									
Orbiter Station 45.2m									
Orbiter Station 68.5m	0.937	0.937	0.031	0.385	0.021	0.483	0.047	0.301	0.054

*About booster station 84.0m

Table 2-6. 1 Degree of Freedom N_o Values

Response Item	Condition No.								
	2	3	4	5	7	8	9	10	11
Booster Wing									
Root Shear	1.358	1.358	—	2.496	—	1.348	—	1.763	—
Root Bending Moment	1.467	1.467	—	2.499	—	1.390	—	1.769	—
Root Torque*	1.428	1.428	—	1.326	—	1.437	—	1.119	—
Tip Acceleration	1.153	1.153	—	0.0	—	1.326	—	0.0	—
Booster Body Acceleration									
Booster Station 29.2m			0.285	0.995	0.239		0.231	0.766	0.222
Booster Station 44.6m									
Booster Station 59.1m									
Booster Station 76.9m									
Booster Station 99.2m									
Orbiter Body Acceleration									
Orbiter Station 5.08m									
Orbiter Station 24.6m									
Orbiter Station 45.2m									
Orbiter Station 68.5m	1.153	1.153	0.285	0.995	0.239	1.326	0.231	0.766	0.222

*About booster station 84.0m

Table 2-7. Rigid Body $\bar{A}$ Values

Response Item	Condition No.								
	2	3	4	5	7	8	9	10	11
Booster Wing									
Root Shear (10^3N)	61.60	60.09	—	2.881	—	55.92	—	2.431	—
Root Bending Moment (10^4N-m)	64.21	61.56	—	2.431	—	61.15	—	2.954	—
Root Torque* (10^4N-m)	49.30	49.12	—	4.751	—	35.80	—	4.527	—
Tip Acceleration (10^{-2}g)	3.823	2.480	—	1.338	—	2.903	—	0.363	—
Booster Body Acceleration (10^{-2}g)									
Booster Station 29.2m	1.480	0.929	0.190	0.361	0.026	1.788	0.098	0.418	0.105
Booster Station 44.6m	0.698	0.771	0.108	0.136	0.026	0.937	0.047	0.367	0.084
Booster Station 59.1m	0.930	0.994	0.027	0.367	0.049	0.465	0.047	0.326	0.063
Booster Station 76.9m	2.058	1.546	0.083	0.795	0.086	1.323	0.113	0.299	0.036
Booster Station 99.2m	3.615	2.367	0.213	1.293	0.129	2.715	0.206	0.311	0.012
Orbiter Body Acceleration (10^{-2}g)									
Orbiter Station 5.08m	3.216	1.719	0.337	0.910	0.234	3.385	0.204	0.378	0.096
Orbiter Station 24.6m	1.867	1.078	0.224	0.627	0.195	2.152	0.122	0.290	0.067
Orbiter Station 45.2m	0.682	0.773	0.105	0.578	0.174	0.909	0.045	0.251	0.052
Orbiter Station 68.5m	1.499	1.266	0.037	0.979	0.111	0.839	0.079	0.201	0.019

*About booster station 84.0m

Table 2-8. Rigid Body N_o Values

Response Item	Condition No.								
	2	3	4	5	7	8	9	10	11
Booster Wing									
Root Shear	1.351	1.366	—	1.506	—	1.435	—	1.888	—
Root Bending Moment	1.406	1.457	—	1.924	—	1.390	—	1.898	—
Root Torque*	1.453	1.451	—	1.486	—	1.535	—	1.123	—
Tip Acceleration	1.330	1.895	—	1.029	—	1.550	—	0.901	—
Booster Body Acceleration									
Booster Station 29.2m	1.623	2.476	0.281	0.945	0.336	2.007	0.362	0.496	0.211
Booster Station 44.6m	1.690	1.585	0.280	0.630	0.178	2.172	0.375	0.610	0.215
Booster Station 59.1m	1.163	1.120	0.291	0.812	0.238	1.375	0.232	0.766	0.221
Booster Station 76.9m	1.261	1.571	0.296	0.875	0.272	1.301	0.278	0.983	0.243
Booster Station 99.2m	1.325	1.871	0.289	0.892	0.286	1.536	0.298	1.132	0.331
Orbiter Body Acceleration									
Orbiter Station 5.08m	1.518	2.653	0.283	0.779	0.274	1.892	0.344	0.616	0.210
Orbiter Station 24.6m	1.585	2.603	0.282	0.920	0.266	1.968	0.356	0.661	0.215
Orbiter Station 45.2m	1.681	1.545	0.280	1.075	0.260	2.180	0.374	0.707	0.220
Orbiter Station 68.5m	1.214	1.372	0.317	1.137	0.225	1.052	0.259	0.901	0.243

*About booster station 84.0m

Table 2-9. Total $\bar{A}$ Values

Response Item	Condition No.								
	2	3	4	5	7	8	9	10	11
Booster Wing									
Root Shear (10^3N)	62.45	56.77	—	4.751	—	62.06	—	3.802	—
Root Bending Moment (10^4N-m)	59.13	55.28	—	5.100	—	66.15	—	3.666	—
Root Torque* (10^4N-m)	50.12	50.61	—	6.334	—	46.77	—	4.097	—
Tip Acceleration (10^{-2}g)	56.88	56.77	—	4.997	—	96.34	—	2.080	—
Booster Body Acceleration (10^{-2}g)									
Booster Station 29.2m	8.102	5.001	0.227	2.249	0.086	9.609	0.370	2.285	0.303
Booster Station 44.6m	3.377	2.511	0.145	1.545	0.078	4.626	0.258	1.661	0.229
Booster Station 59.1m	5.831	3.978	0.080	1.666	0.087	9.080	0.167	1.004	0.158
Booster Station 76.9m	4.947	4.514	0.101	1.726	0.105	5.813	0.123	0.572	0.054
Booster Station 99.2m	6.779	6.284	0.217	1.950	0.133	7.551	0.262	1.095	0.096
Orbiter Body Acceleration (10^{-2}g)									
Orbiter Station 5.08m	28.77	52.13	0.521	3.148	0.268	41.86	0.900	3.002	0.399
Orbiter Station 24.6m	4.409	13.70	0.275	1.421	0.210	5.388	0.455	1.735	0.275
Orbiter Station 45.2m	4.702	3.011	0.146	1.046	0.183	7.587	0.256	1.671	0.214
Orbiter Station 68.5m	13.10	8.877	0.093	1.586	0.110	19.05	0.154	3.233	0.037

*About booster station 84.0m

Table 2-10. Total N_o Values

Response Item	Condition No.								
	2	3	4	5	7	8	9	10	11
Booster Wing									
Root Shear	2.006	2.032	—	0.929	—	2.086	—	1.329	—
Root Bending Moment	2.279	2.350	—	0.885	—	1.981	—	1.422	—
Root Torque*	2.303	2.235	—	1.311	—	2.260	—	1.151	—
Tip Acceleration	2.550	2.646	—	3.221	—	2.279	—	1.455	—
Booster Body Acceleration									
Booster Station 29.2m	2.117	1.998	0.511	2.041	0.465	2.184	0.518	1.071	0.461
Booster Station 44.6m	1.786	1.633	0.490	1.061	0.465	1.702	0.525	1.014	0.459
Booster Station 59.1m	2.409	2.248	0.793	1.420	0.430	2.621	0.777	0.994	0.455
Booster Station 76.9m	2.263	1.897	0.586	1.493	0.376	2.762	0.722	1.597	0.412
Booster Station 99.2m	1.905	1.645	0.413	1.863	0.336	1.745	0.522	1.274	0.476
Orbiter Body Acceleration									
Orbiter Station 5.08m	1.950	1.267	0.728	2.050	0.347	1.939	0.720	1.052	0.472
Orbiter Station 24.6m	1.631	1.160	0.431	1.351	0.298	1.859	0.495	0.664	0.470
Orbiter Station 45.2m	2.000	2.132	0.608	0.895	0.284	1.983	0.630	0.948	0.471
Orbiter Station 68.5m	2.445	2.235	1.350	1.573	0.362	2.717	1.309	1.360	0.729

*About booster station 84.0m

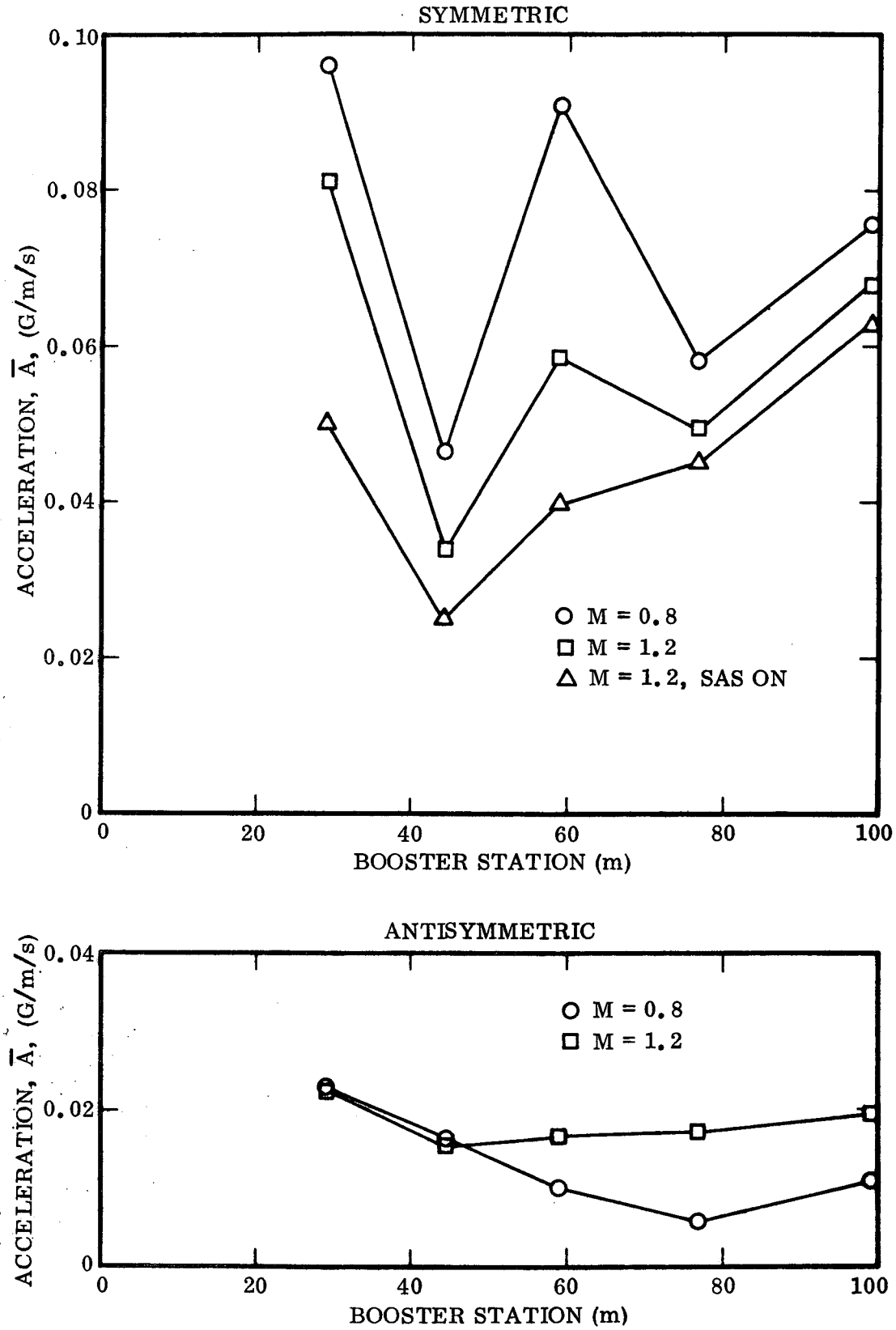

Figure 2-34. Booster $\bar{A}$ Accelerations

nearly a factor of 2. Figure 2-35 shows that the orbiter symmetric rms nose acceleration is about five times as large as the booster rms nose acceleration. It is also interesting to note that while the SAS lowers the booster accelerations, it increases the orbiter nose acceleration by 82%.

The booster and orbiter $\bar{A}$ accelerations are shown in Figures 2-36 and 2-37, respectively for the conditions with booster aerodynamic surfaces removed. It can be seen that removing the booster aerodynamic surfaces lowers the $\bar{A}$ accelerations by an order of magnitude. The booster and orbiter nose accelerations are consistently higher at Mach 0.8 than at Mach 1.2.

Responses due to 1-m/s amplitude quasi-square wave discrete turbulence are shown in Figures 2-38 through 2-46. Figure 2-38 shows envelopes of booster body peak acceleration for symmetric and antisymmetric turbulence. As in the random case, symmetric turbulence produces higher accelerations. Corresponding plots for the orbiter are shown in Figure 2-39. Again, the orbiter nose symmetric acceleration is considerably higher than for the booster.

Actual response time histories due to the 1-m/s quasi-square-wave gust are given in Figures 2-40 through 2-46. Booster wing root shear, bending moment, and torque due to symmetric gust are given in Figures 2-40, 2-41, and 2-42, respectively. Booster wing tip acceleration is shown in Figure 2-43. All of these figures show the total, one degree of freedom, and rigid body responses separately. Figures 2-44 and 2-45 show the corresponding booster and orbiter nose acceleration time histories, respectively. Total antisymmetric responses are shown in Figure 2-46 for booster wing root shear, bending moment, and torque, and booster wing tip acceleration.

It is interesting to compare the random and discrete turbulence results. Table 2-11 summarizes the booster wing root shear and bending moment at Mach 1.2 due to symmetric random and discrete turbulence. As specified in Reference 4, the rms loads from the random analysis based on the 99^{th} percentile PSD were multiplied by three to yield design values. The discrete quasi-square-wave gust results were multiplied by nine to yield design values corresponding to a 9 m/s amplitude gust. It can be seen that the discrete turbulence loads are higher approximately by the ratio of the discrete turbulence level to the 3σ random value $\left(\frac{9}{3 \times 1.94}\right)$, indicating that the discrete turbulence design criteria may be overly conservative (corresponding to about 5σ random turbulence).

The elastic contribution to the total load is also greater for discrete turbulence. This is probably because the gust length was set so as to excite the fundamental mode, which had a large wing motion. In fact in the random case, the elastic effect was to reduce the total wing root bending moment.

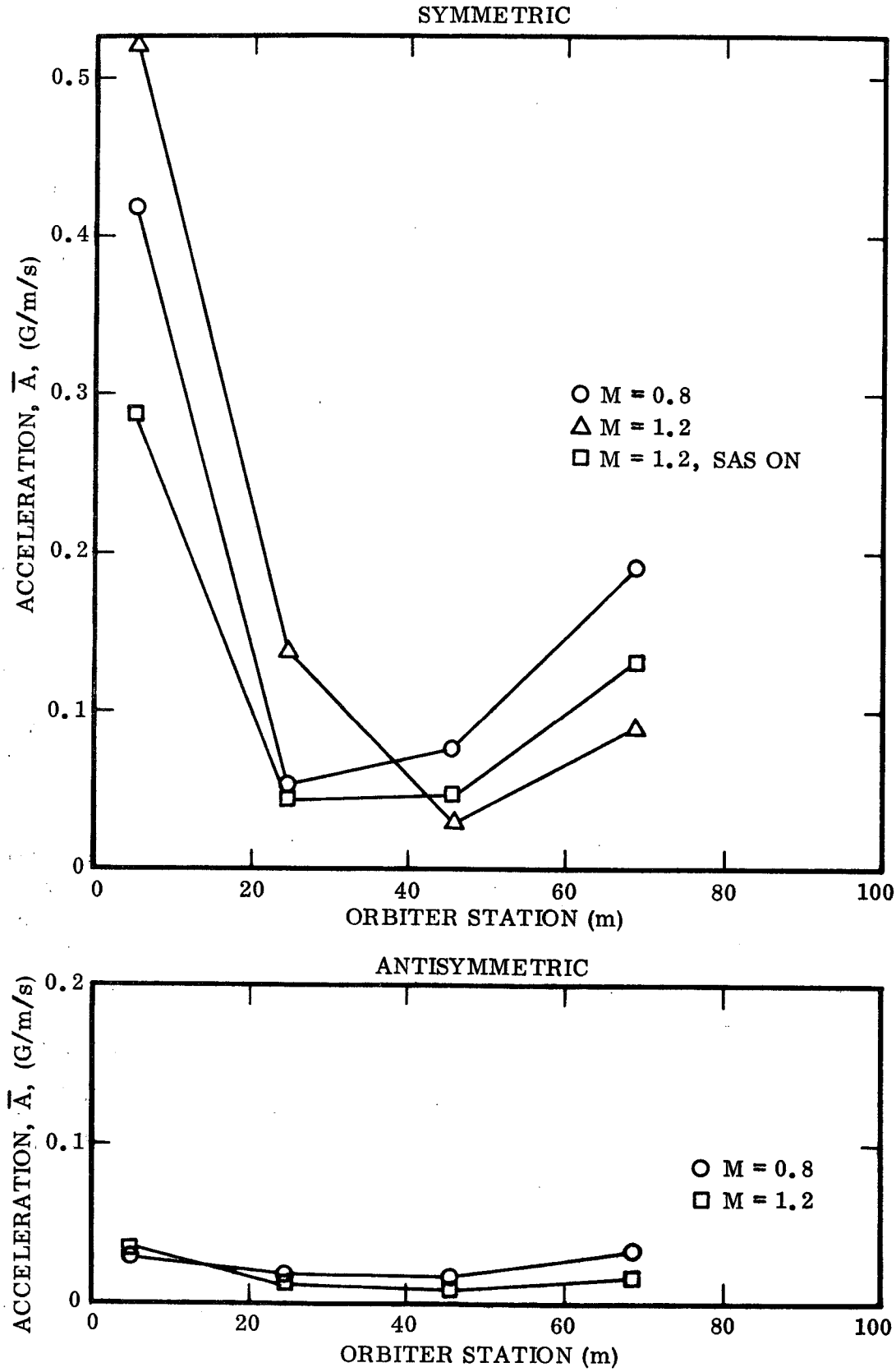

Figure 2-35. Orbiter $\bar{A}$ Accelerations

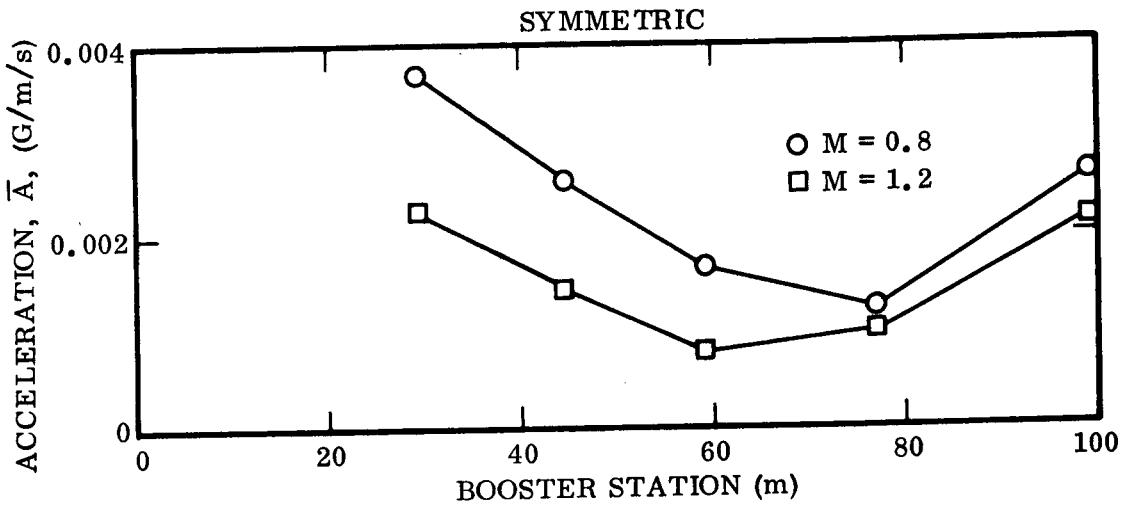

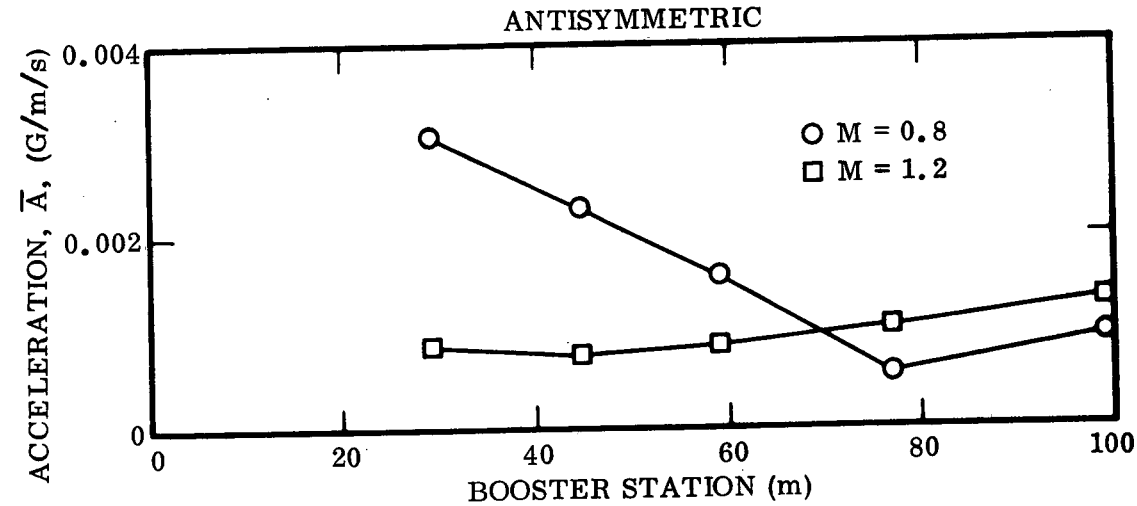

Figure 2-36. Booster $\bar{A}$ Accelerations (Booster Aerodynamic Surfaces Removed)

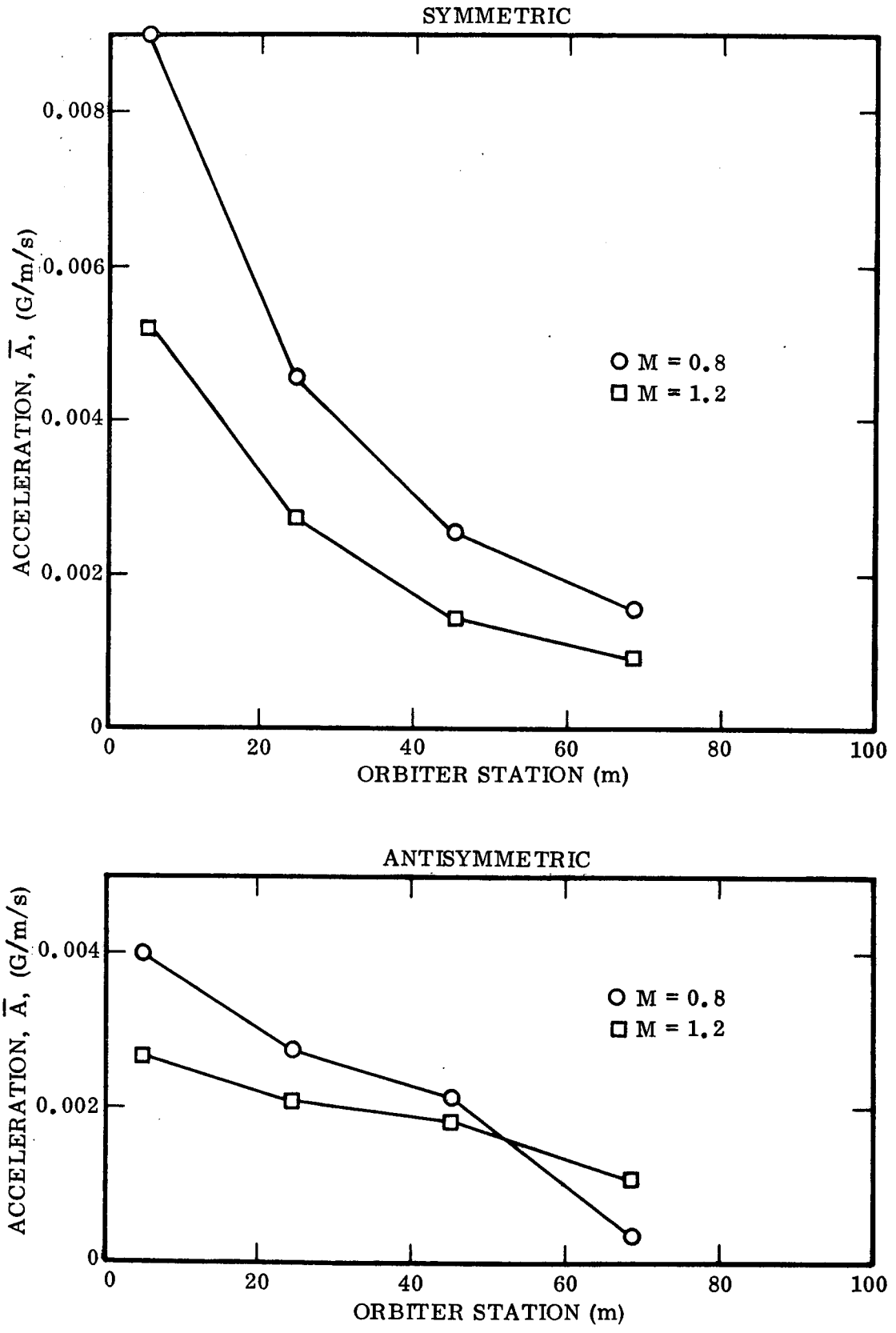

Figure 2-37. Orbiter $\bar{A}$ Accelerations (Booster Aerodynamic Surfaces Removed)

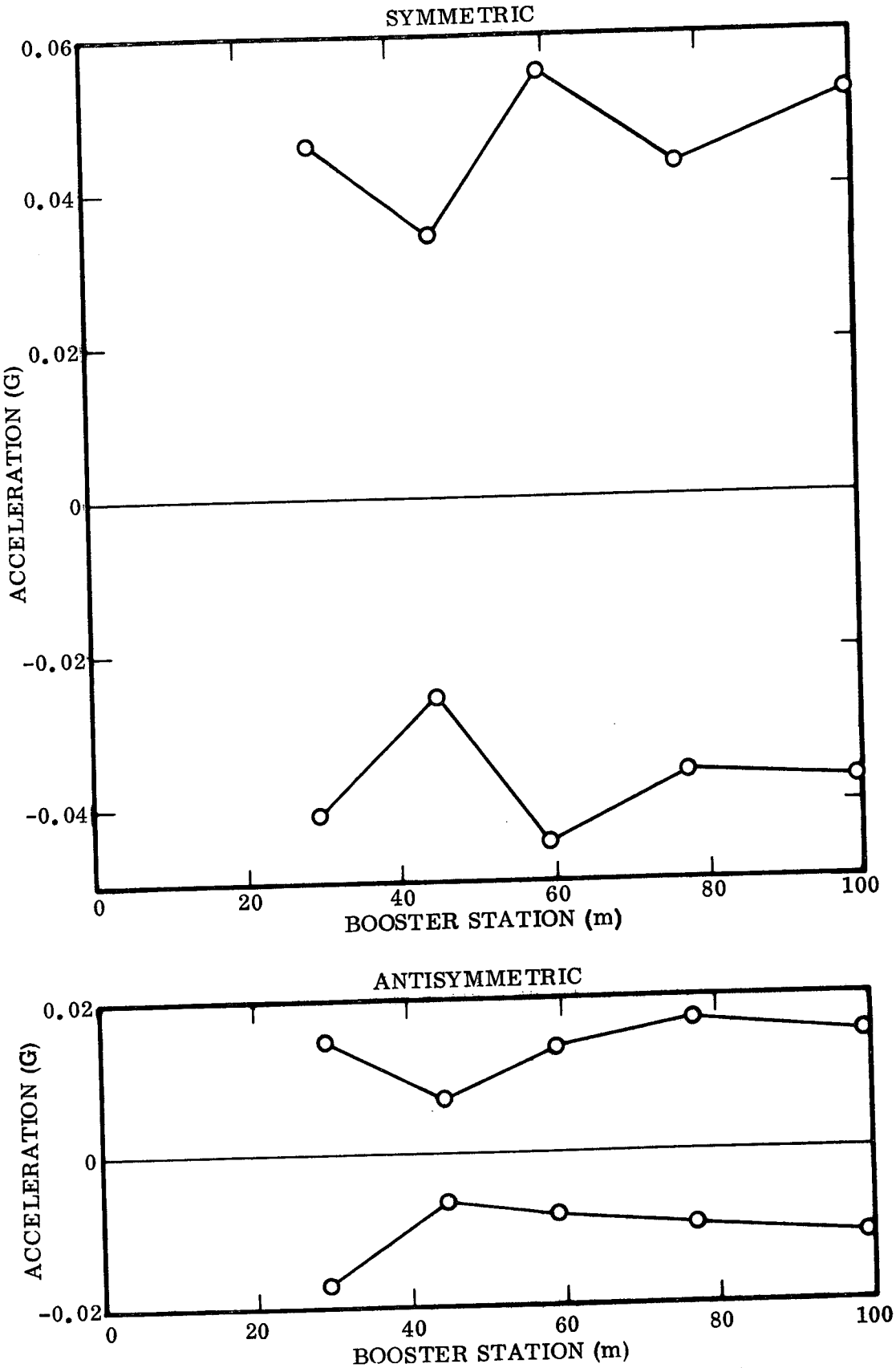

Figure 2-38. Booster Peak Acceleration Envelopes at M = 1.2 Due to 1-m/s Quasi-square Gust

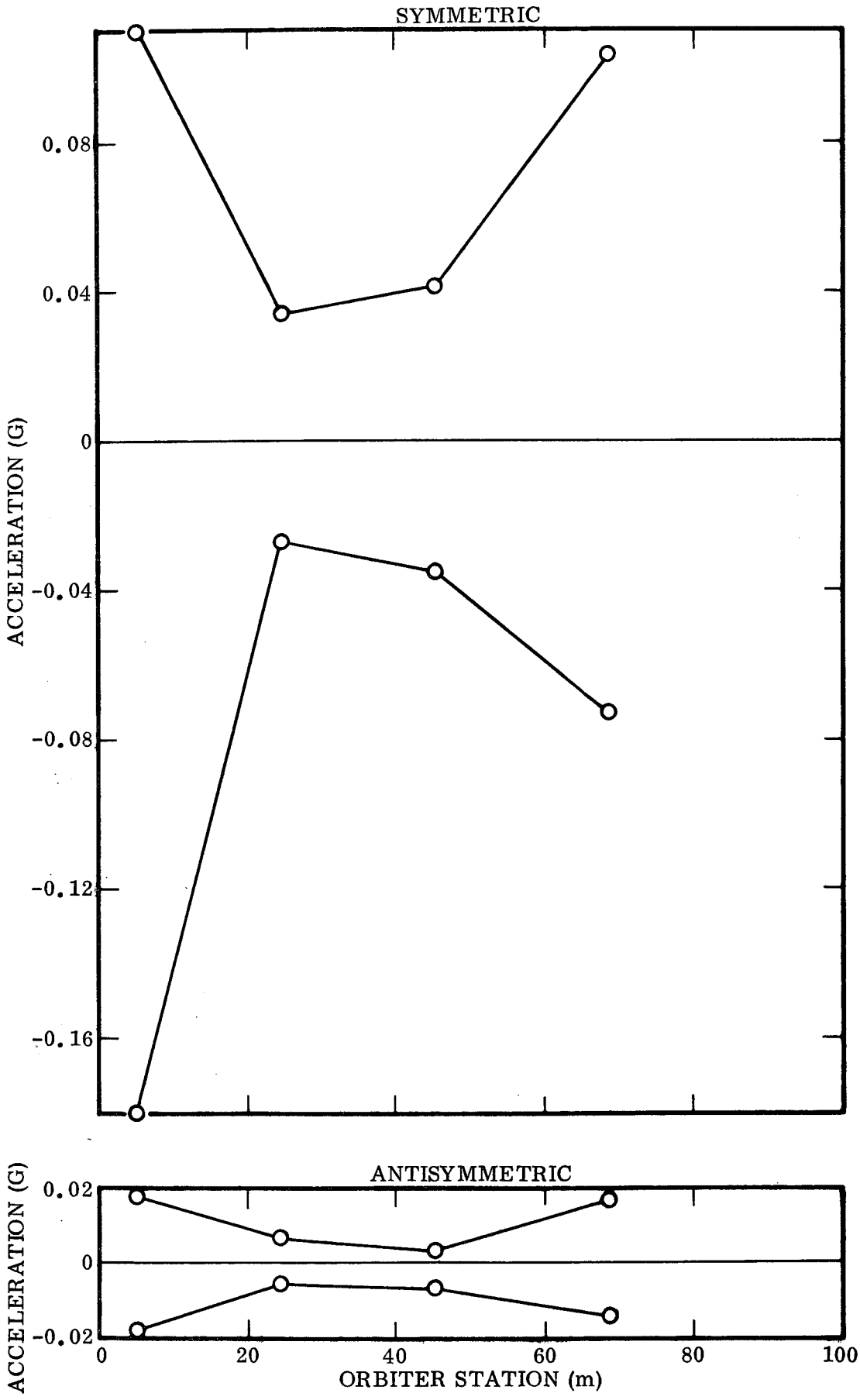

Figure 2-39. Orbiter Peak Acceleration Envelopes at M = 1.2 Due to 1-m/s Quasi-square Gust

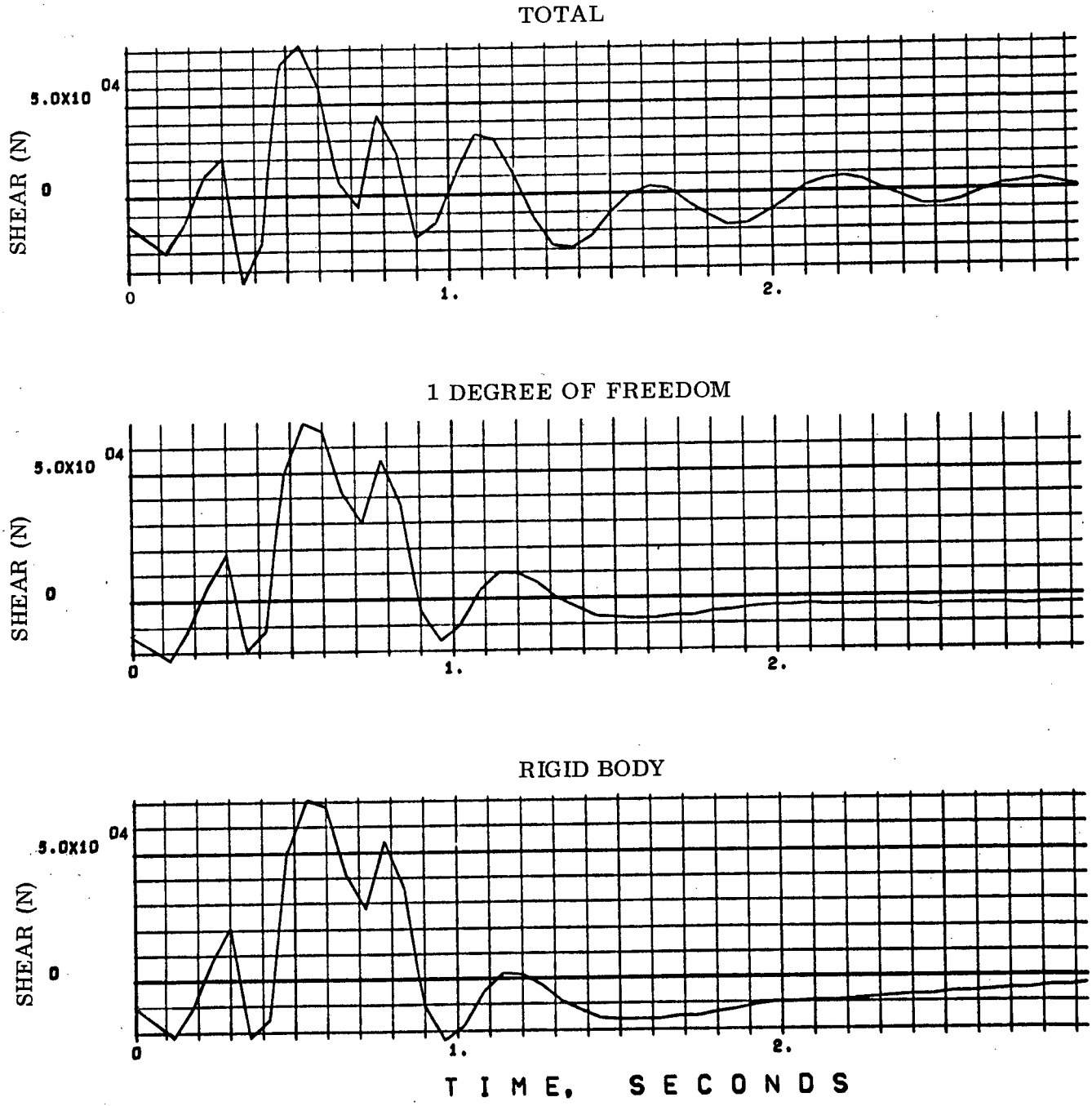

Figure 2-40. Booster Wing Root Shear at M=1.2 Due to 1-m/s Symmetric Quasi-square Gust

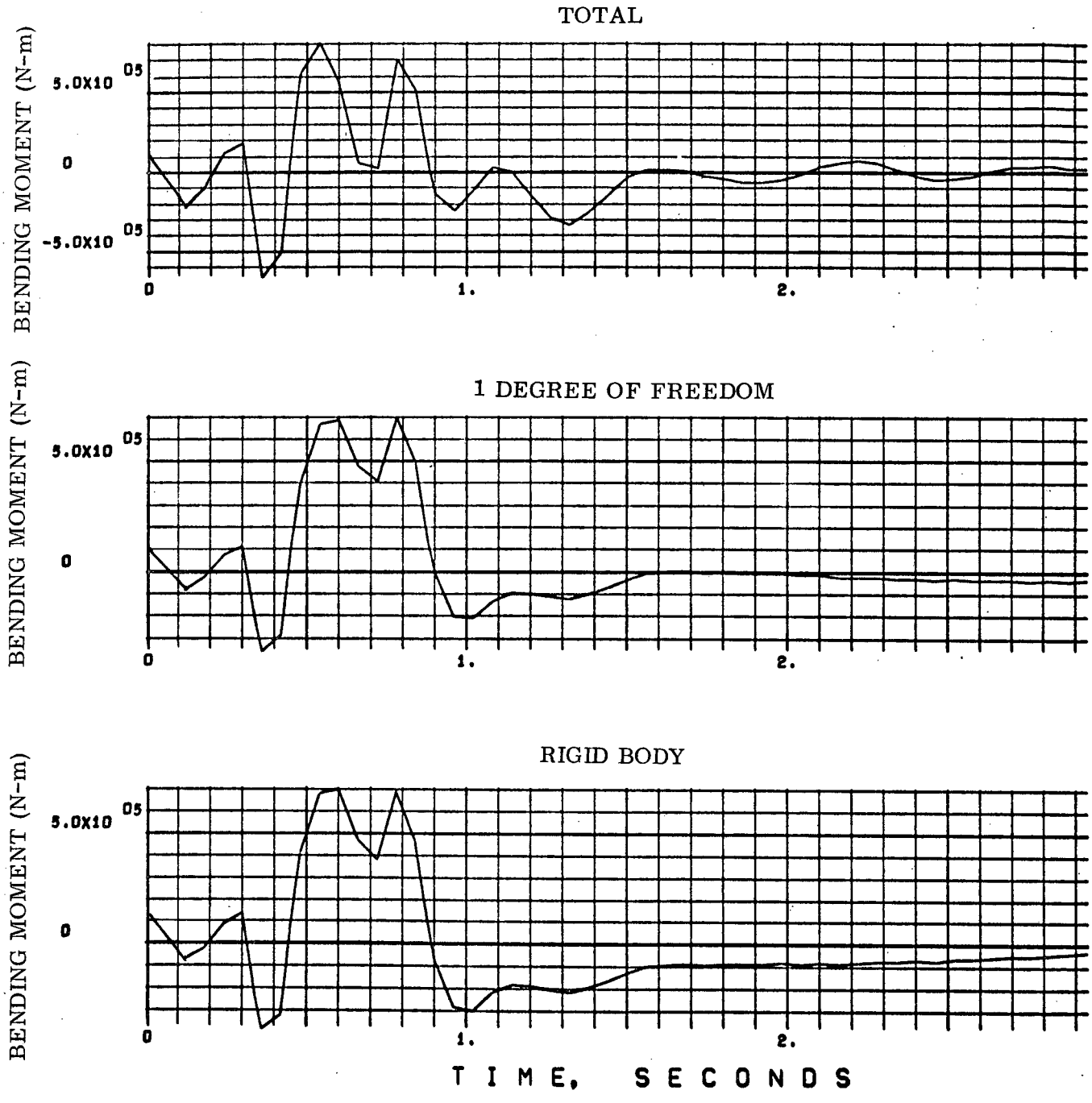

Figure 2-41. Booster Wing Root Bending Moment at M=1.2 Due to 1-m/s Symmetric Quasi-square Gust

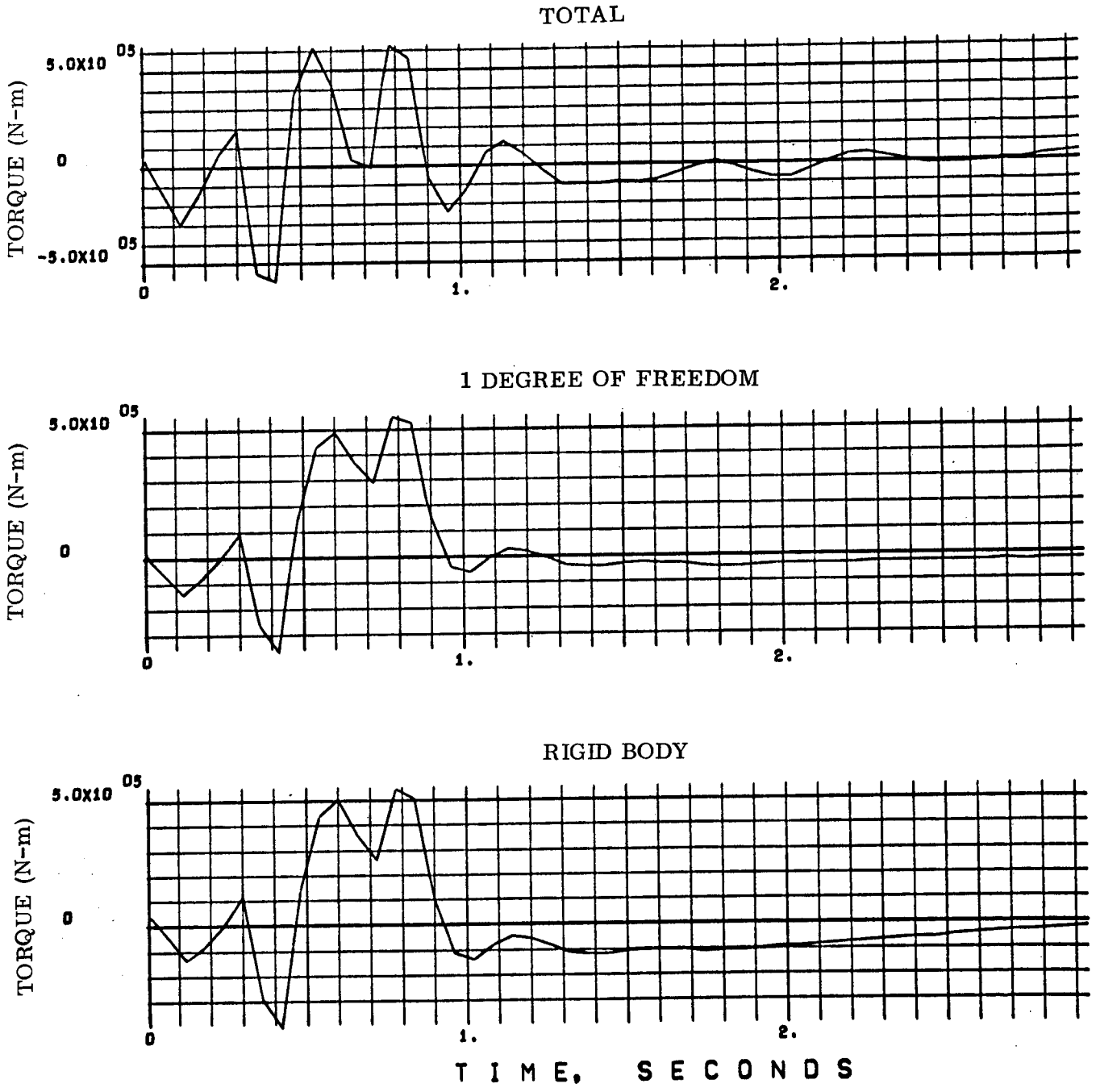

NOTE: TORQUE ABOUT BOOSTER STATION 84.0m

Figure 2-42. Booster Wing Root Torque at M=1.2 Due to 1-m/s Symmetric Quasi-square Gust

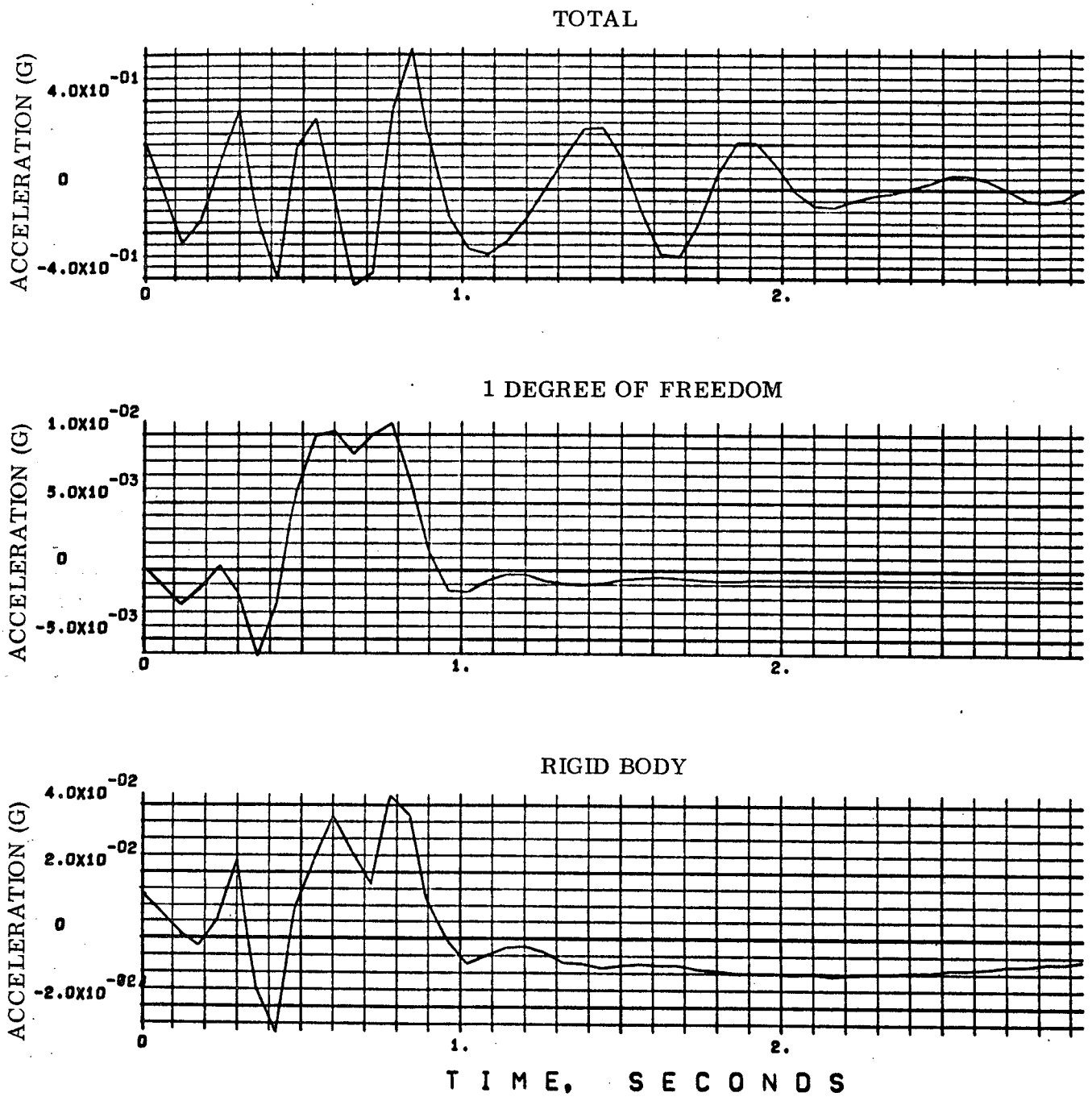

Figure 2-43. Booster Wing Tip Acceleration at M=1.2
Due to 1-m/s Symmetric Quasi-square Gust

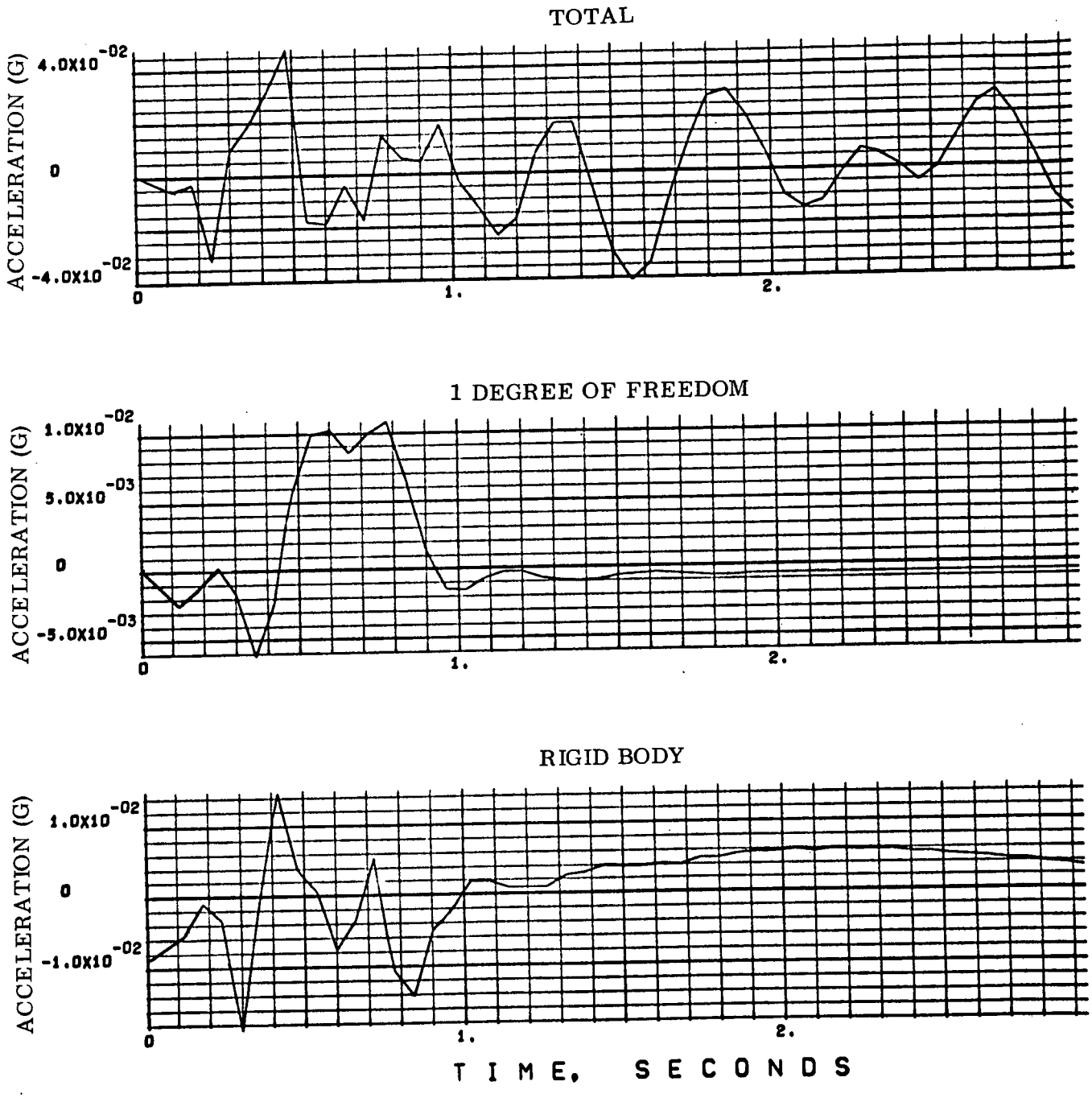

Figure 2-44. Booster Body Acceleration at Booster Station 29.2m at M=1.2 Due to 1-m/s Symmetric Quasi-square Gust

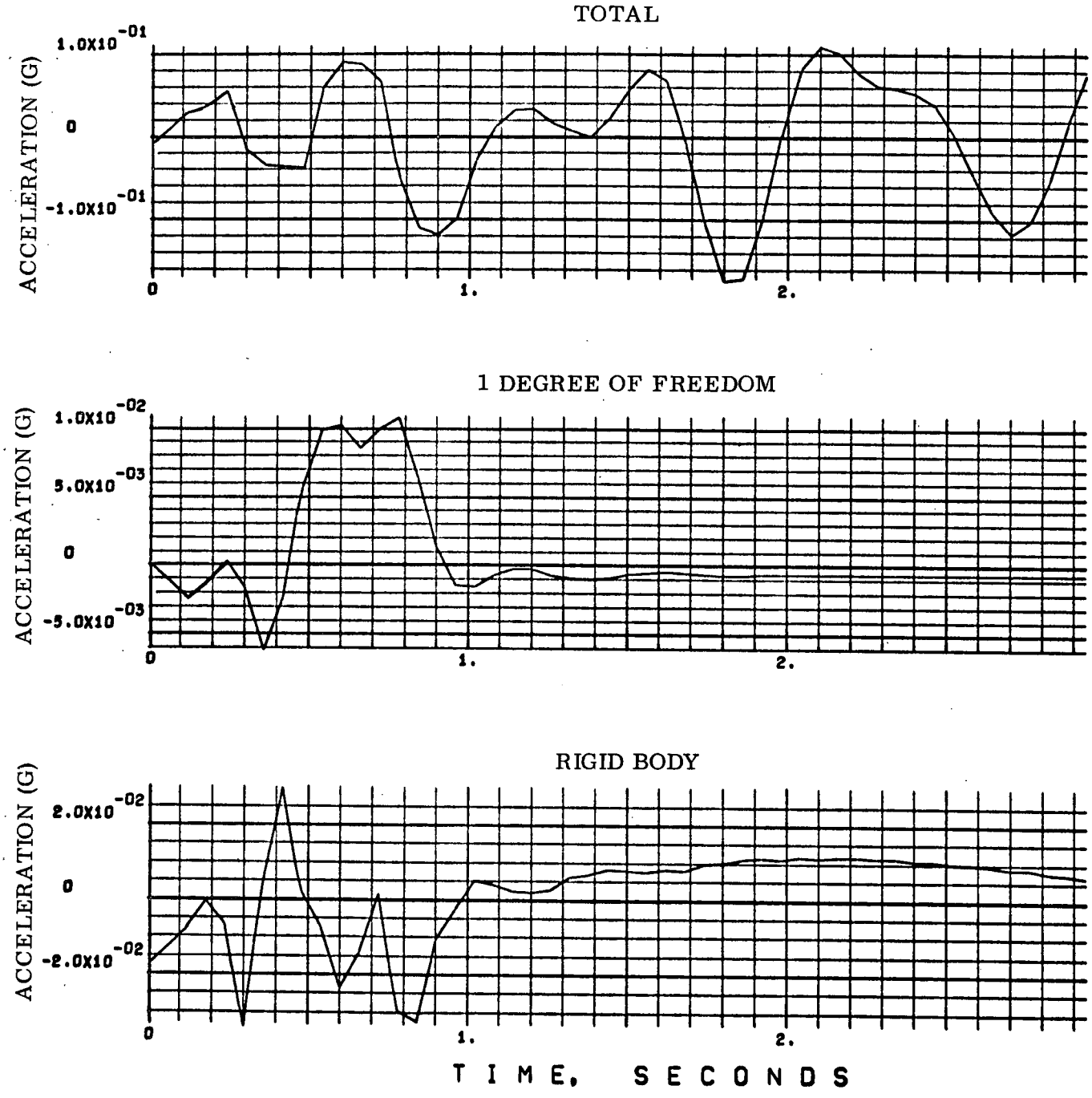

Figure 2-45. Orbiter Body Acceleration at Orbiter Station 5.08m at M=1.2 Due to 1-m/s Symmetric Quasi-square Gust

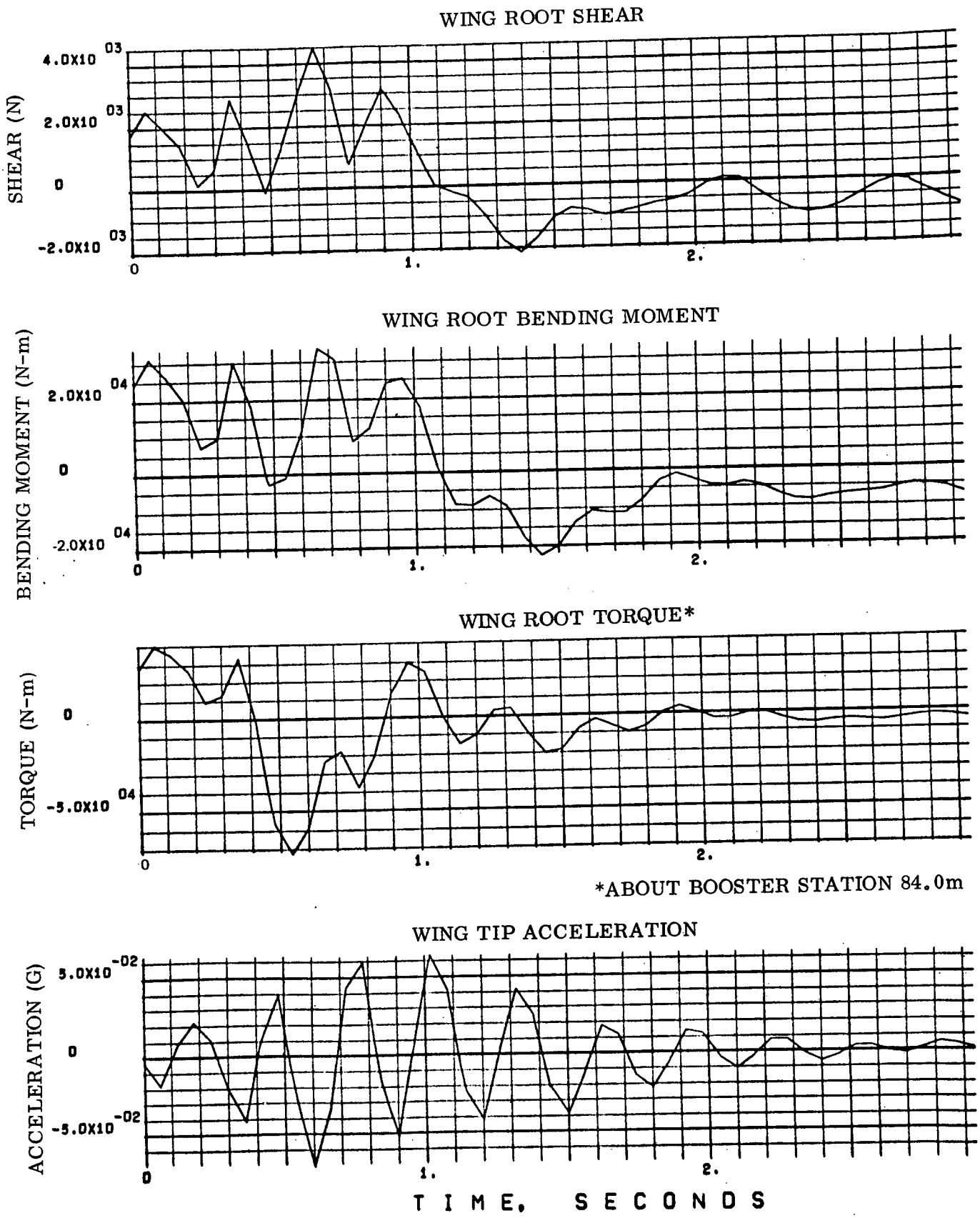

Figure 2-46. Booster Total Response to 1-m/s Antisymmetric Quasi-square Gust at M=1.2

Table 2-11. Booster Wing Root Shear and Bending Moment Due to Symmetric Turbulence at Mach 1.2

Gust Type	Shear (10^5N)				Bending Moment (10^6N-m)			
	Total	Rigid	Elastic	Total / Rigid	Total	Rigid	Elastic	Total / Rigid
Random	3.634	3.560	0.074	1.02	3.442	3.737	-0.295	0.92
Discrete	7.465	6.416	1.049	1.16	7.316	6.350	0.966	1.15

To determine the criticality of these loads, booster design wing loads were obtained from Reference 9 and are shown in Table 2-12. The maximum αQ loads include a 20% allowance for static aeroelastic effects and elastic portion of turbulence response. From these comparisons, it appears that including the rigid portion of the gust response in the ascent trajectory analysis and multiplying the results by a factor of 1.2 is conservative for space shuttle, although this should be verified by a static aeroelastic analysis.

Table 2-12. Booster Design Wing Root Shear and Bending Moment (Reference 9)

Design Condition	Total (Rigid + Elastic)		Elastic	
	Shear (10^5N)	Bending Moment (10^6N-m)	Shear (10^5N)	Bending Moment (10^6N-m)
Maximum αQ (Mach 1.2)	28.77	19.65	4.77	3.30
Reentry	28.94	18.43		
2.5g Maneuver	23.08	16.98		
Design Gust	22.62	16.53		

SECTION 3

CONCLUSIONS AND RECOMMENDATIONS

A fully reusable space shuttle configuration has been analyzed at Mach numbers 0.8 and 1.2 during ascent flight to determine its responses to random and discrete atmospheric turbulence. To simulate an expendable booster, the booster aerodynamic surfaces were removed for portions of the analysis.

Aerodynamic interference effects have been shown to be significant for space shuttle. The Woodward method appears to be the best analytical approach for determining steady-state pressure distributions for complex configurations at subsonic and supersonic speeds. The Woodward method has correlated well with wind tunnel total force and moment data for the configuration analyzed. Further testing is desirable to provide pressure data for complex configurations such as space shuttle to verify the Woodward approach.

The symmetric random turbulence analysis showed higher accelerations on the booster and orbiter at Mach 0.8 than at Mach 1.2. Antisymmetrically, booster accelerations are higher at 1.2 Mach number. The booster and orbiter accelerations are lower, however, by an order of magnitude in the antisymmetric condition than in the symmetric case.

Inclusion of the booster stability augmentation system lowered the symmetric accelerations for the booster, but agravated the orbiter front-end response. Loads due to a 9 m/s quasi-square-wave gust were found to be higher than 3σ random turbulence loads, indicating that the discrete gust design criterion may be conservative. It was found that elastic response accounted for about 15% of the total wing gust load in the discrete analysis, while in the random case, the elastic effect was small.

Comparison with booster wing design loads indicates that the wing elastic gust loads fall well within the 20% increase in total rigid body loads allocated for elastic effects. Static aeroelastic loads, not computed in the present study, are required to determine the actual design margin.

The turbulence response analysis method employed herein is costly and requires extensive input data. Simpler methods would be more attractive for preliminary design and configuration trade studies. The approximate methods would have to be evaluated against the present approach, however, to determine whether the results are sufficiently accurate.

SECTION 4

REFERENCES

1. R. G. Huntington, A Method for Determining the Response of Space Shuttle to Atmospheric Turbulence, "Volume I, Space Shuttle Turbulence Response," GDC-DDE71-002, General Dynamics Convair Aerospace Division, 1 November 1971.

2. R. G. Huntington and R. L. Haller, A Method for Determining the Response of Space Shuttle to Atmospheric Turbulence, "Volume II, Computer Program Description and Usage Instructions," GDC-DDE71-006, Convair Aerospace Division of General Dynamics, December 1971.

3. F. A. Woodward, "Analysis and Design of Wing-Body Combinations at Subsonic and Supersonic Speeds," Journal of Aircraft, Vol. V, No. 6, 1968.

4. Terrestrial Environment (Climatic) Criteria Guidelines for Use in Space Vehicle Development, 1971 Revision, TM X-64589, NASA, 10 May 1971.

5. R. H. MacNeal, (Editor), The NASTRAN Theoretical Manual, SP-221, NASA, September 1970.

6. R. J. Guyan, "Reduction of Stiffness and Mass Matrices," AIAA Journal, Vol. 3, No. 2, February 1965.

7. W. E. Rister, et al, Aerodynamic Design Data Book for B-9U Booster, 16-549-4-176, General Dynamics Convair Aerospace Division, July 1971.

8. D. O. Lomen, Analysis of Fluid Sloshing, GDC-DDE66-018, Convair Aerospace Division of General Dynamics, June 1966.

9. Anon., Space Shuttle Booster B-9U Loads (Phase B Study Design Load Data), 76-549-30-008, General Dynamics Convair Aerospace Division, 1 June 1971 Revision.